Measurement of ^{23}Na(α,p)^{26}Mg at Energies Relevant to ^{26}Al Production in Massive Stars and Nucleosynthesis in Type 1a Supernovae

Jessica Rachael Tomlinson

PhD

University of York

Physics

September 2015

Abstract

^{26}Al is an important radionuclide in astrophysics. Its decay to ^{26}Mg results in the emission of a 1.8 MeV gamma-ray which is detected and mapped across the galaxy, providing evidence of ongoing nucleosynthesis in the universe. Its origin is still not understood, however observations suggest massive stars as a possible main production site. A post processing network calculation study modelled nucleosynthesis in the C/Ne convective-shell before the core collapse of a massive star and found that the ^{23}Na(α,p)^{26}Mg reaction is important for the synthesis of ^{26}Al in this environment.

Due to large uncertainties in previous experimental measurements of this reaction, theoretically calculated Hauser-Feshbach cross sections were used to calculate the ^{23}Na(α,p)^{26}Mg reaction rate for the post processing calculations. This theoretical rate has large uncertainties as the statistical model used to calculate the cross sections is not thought to be applicable for the level density of the compound nucleus ^{27}Al.

The ^{23}Na(α,p)^{26}Mg reaction is also found to play an important role in the nucleosynthesis of several nuclei in type Ia supernovae explosions by several sensitivity studies. Again these studies used the reaction rate from Hauser-Feshbach statistical model cross-section calculations.

A measurement has been made of the ^{23}Na(α,p)^{26}Mg reaction cross section in inverse kinematics using the TUDA scattering chamber at TRIUMF laboratory in Canada. The cross sections were calculated in the energy range $E_{\mathrm{c.m.}} = 1.28$ - 3.15 MeV and found to be in reasonable agreement with the Hauser Feshbach model calculations. A new reaction rate has been calculated providing tight constraints on the uncertainty in the production of ^{26}Al in the C/Ne convective shell of massive stars due to the ^{23}Na(α,p)^{26}Mg reaction.

Contents

List of Figures

List of Tables

Acknowledgements

Firstly I would like to thank my supervisor Alison Laird, without whom none of this would be possible. She has encouraged and guided me through every part of my PhD and I am very grateful to her. I would also like to thank Simon Fox for all his help and guidance both during the experiment and setup, and with the data analysis, especially all the help with MIDAS when it had a mind of its own. He made experiments a lot more fun! As well as this, I am grateful to Thomas Davinson for his patient guidance and help, especially for the experimental setup. I would also like to thank him for the sort codes used in the data analysis of this work and for all his advice with analysis and detectors. I would like to thank Alex Murphy for his amazing Monte Carlo simulations, and for his advice throughout my PhD.

I am also grateful for all the help from the Dragon group at TRIUMF, especially Jennifer Fallis who was co-PI on this experiment. To everyone who worked on the experimental runs: Chris Ruiz, Peter Machule, Max Chen, Martine Alcorta, Barry Davids, Alan Shotter, Nicolas de Séréville, Charlie Akers, Greg Christian, Naomi Galinski, Matt Pearson and Alex Rojas, thank-you for taking shifts, noise chasing, leak testing, aligning and all the other fun things that go with TUDA experiments!

A big thank-you goes to all the PhD students and academics in the nuclear group at York, especially Philip Adsley who has answered so, so many of my questions and Edward Martin who helped me so much with coding, especially ROOT. Thanks must also go to Christian Diget, Brian Fulton and Mike Bentley for all their assistance and encouragement. Also everyone in my office, James, Jos, Stephen, Nuray, Nic, Mark and Adam and my best friends Keri, Ruchi and Adelle who enjoyed thesis submission week so much.

Finally, I would like to thank my entire family, especially my Mum, Dad, Ben, Adam, Becky and Saffey for their constant encouragement and for reminding me there is world outside my PhD bubble.

Declaration

I hereby declare that except where a specific reference is made to the work of others, the contents of this thesis are original and have not been submitted in whole or in part for consideration for any other degree or qualification in this, or any other university. This dissertation is my own work and contains nothing which is the outcome of work done by others, except as specified in the text and Acknowledgements. All sources are acknowledged as references.

Jessica Rachael Tomlinson

September 2015

Chapter 1

Introduction and Motivation

The nuclear processes which occur in stars are responsible for creating the building blocks for life on earth. Nuclear astrophysics is a field of study concerned with finding the origin of the chemical elements and understanding the processes which lead to their creation in the various stellar environments. In order to understand the origin of the chemical elements we must understand the nuclear processes involved in their creation. Experimental nuclear astrophysics aims to measure important nuclear information such as nuclear lifetimes and reaction rates in astrophysical environments, in order to explain the processes happening inside stellar environments. This leads to a better understanding of the origin of the nuclei of which we are made.

These measurements, coupled with observational evidence from gamma-ray astronomy and measurements of the isotopic abundances of pre-solar grains and meteorites, allow theoreticians to constrain astrophysical models. This leads to a better understanding of how the chemical elements, which make up life on earth, came to be. Although much progress has been made in measuring reaction cross sections in the laboratory, there are still many which remain unmeasured, necessitating the use of theoretical predictions of the cross sections as input for astrophysical models. This can lead to large uncertainties. The relatively low energy of astrophysical environments can make cross section measurements in the laboratory difficult. Further, the nuclei involved in these reactions are often unstable and can be difficult to study in the laboratory.

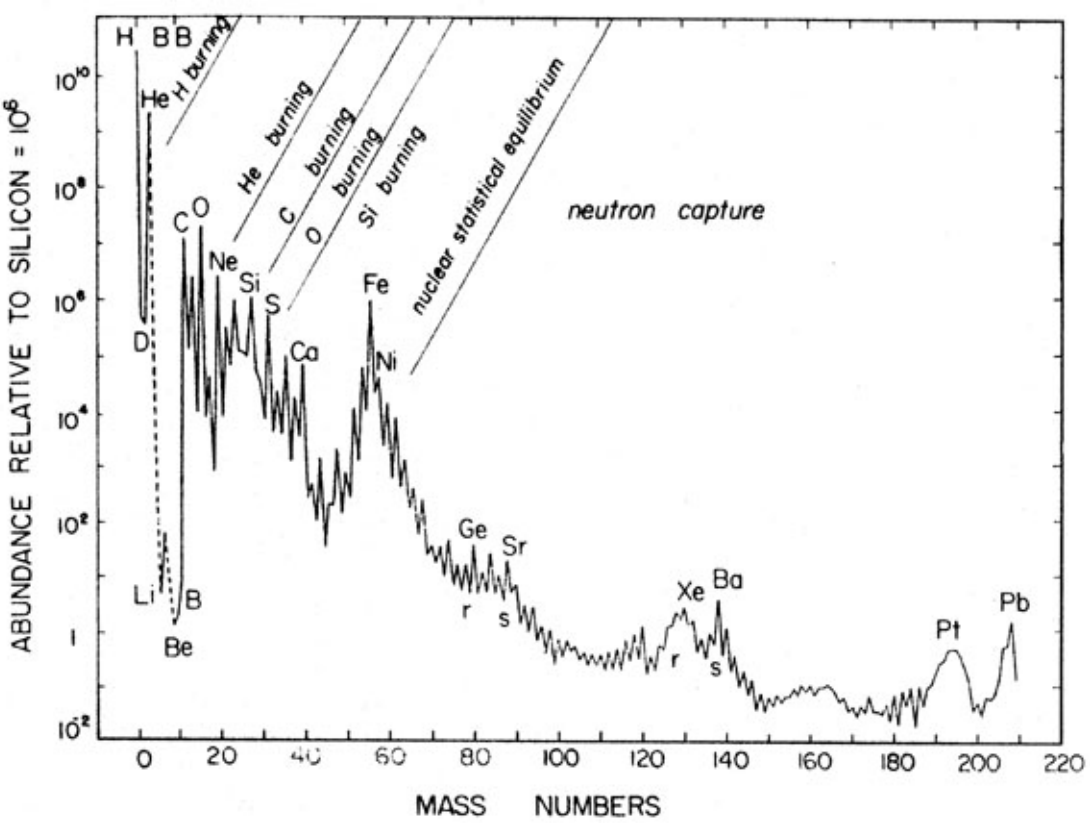

Fig. 1.1 The local Galactic abundance distribution of nuclei and the processes by which they are created, see text for additional details. Figure taken from reference [1].

Figure 1.1 shows the relative abundance of nuclei in the local Galaxy. Hydrogen and helium are the most abundant elements and were mainly formed during Big Bang nucleosynthesis along with deuterium. Some helium is also produced by hydrogen burning in stellar environments. The abundance of lithium, beryllium and boron is from cosmic-ray spallation reactions with CNO nuclei, with some of the lithium being produced in the Big Bang. These nuclei are easily destroyed in fusion reactions with protons and so an abundance minimum is observed here [2]. Nuclei from carbon to calcium are from successive stages of stellar burning. The iron peak nuclei are produced in explosive burning environments in supernovae explosions. These nuclei are energetically the most stable and so we observe an abundance peak [2].

Beyond the iron peak, nucleosynthesis via charged-particle reactions becomes unlikely due to the large Coulomb repulsion and so the majority of nuclei after this are produced by neutron capture reactions. There are two neutron capture processes, the slow neutron capture process (s-process) and the rapid neutron capture

process (r-process). The s-process occurs when neutrons are captured by nuclei which subsequently undergo beta decay producing nuclei along the valley of stability up to ^{209}Bi when alpha decay halts the process. Where the neutron-capture reactions are much faster the r-process occurs. In this case neutron-capture reactions happen faster than the competing beta-decay processes producing unstable nuclei along the neutron drip line up to the point where neutron capture reactions are balanced by photodisintegrations. When the neutron abundance begins to be exhausted the unstable neutron-rich nuclei produced decay to the valley of stability. The stable nuclei which are neutron deficient between ^{74}Se and ^{196}Hg cannot be produced by the s- and r- processes. Instead they are produced by the p-process via (p,γ) and (γ,n) reactions [2].

1.1 ^{26}Al Production in the Universe

^{26}Al is an important radionuclide in nuclear astrophysics. It beta decays to an excited state in ^{26}Mg with a half-life of $\sim$7.2$\times$10^5 years which subsequently decays to its ground state emitting a 1.8 MeV gamma-ray which was first observed in 1984 [3]. This emission line is one of the most intense gamma-rays observed in the interstellar medium [4]. The fact that it is currently observed is evidence of continuing nucleosynthesis in the Galaxy due to its relatively short lifetime compared to the timescale of Galactic evolution of $\sim$10^{10} years [5].

It has also been observed in meteorites via an excess of its decay product ^{26}Mg [6]. The discovery was made in calcium-aluminium rich inclusions (CAIs) which were some of the first solids to condense in the early Solar System material [7]. This observation has led to the conclusion that ^{26}Al was present and reasonably widespread in the early solar system with an abundance ratio of ^{26}Al/^{27}Al $\sim$ 5$\times$10^{-5} [8]. The favoured scenario for its presence is contamination of the proto-solar system by massive stars [7]. Understanding the origin of the radionuclide ^{26}Al would therefore give information on the formation of the Solar System.

^{26}Al has also been observed in pre-solar grains, again via an excess of its decay product ^{26}Mg. These grains are thought to have been produced in stellar environments before the formation of the solar system and preserved in meteorites [9]. The isotopic composition of these grains can therefore provide information about the nuclear processes occurring in the stellar environment in which they are formed providing constraints for astrophysical models and complementing astrophysical observations. Again, this makes information on the astrophysical origin of this radionuclide highly important in nuclear astrophysics.

The origin of the main production site of ^{26}Al is still under debate. There are two main characteristics needed by the environment in which it is produced. Firstly, the stellar environment must be hot enough with T$\geq$10^8 K and, secondly, there must be sufficient seed nuclei for its production. As well as this the ^{26}Al must be ejected into the interstellar medium before it is destroyed in the hot environment in which it is created [10]. Several sites have been proposed for the production of ^{26}Al. These sites include Wolf-Rayet stars, which are massive stars with M$\geq$30M$_\odot$ with strong stellar winds, thought to eject the ^{26}Al into the interstellar medium. Core collapse supernovae have also been identified as a possible production site [11].

The Compton Gamma-Ray Observatory (CGRO), launched in 1991, used the COMPTEL instrument to create the first 1.8 MeV mapping of the Galaxy [5]. The map showed that the emission was clustered asymmetrically along the Galactic plane, which favoured a massive star hypothesis for the main production site of ^{26}Al since massive stars are known to form in clusters [10]. In conjunction with this Knödlseder [5] investigated the correlation between the 1.8 MeV gamma-ray line from the COMPTEL data and the 53 MHz microwave free-free emission. Free-free emission is produced by the acceleration of electrons in the electrostatic field of ionised gas and it can be used to map out the distribution of ionised gas in the Galaxy. Massive stars with M$\geq$20M$_\odot$ are found to substantially contribute to the ionisation of the interstellar medium. Knödlseder concluded that the close correlation

between the 1.8 MeV gamma-ray line and the microwave free-free emission suggests that the origin of ^{26}Al is massive stars with M $\geq$ 20M$_{\odot}$ [5].

More recently galactic ^{26}Al maps, which show the distribution of the radioisotipe in the Galaxy, have been created by the SPI (SPectrometer on Integral) spectrometer. The SPI spectrometer is on board the INTErnational Gamma-Ray Astrophysics Laboratory (INTEGRAL) mission [4]. Data from the INTEGRAL SPI showed that ^{26}Al is co-rotating with the Galaxy, supporting a Galaxy-wide origin [12]. Figure 1.2 shows the most recent map produced by the INTEGRAL space mission.

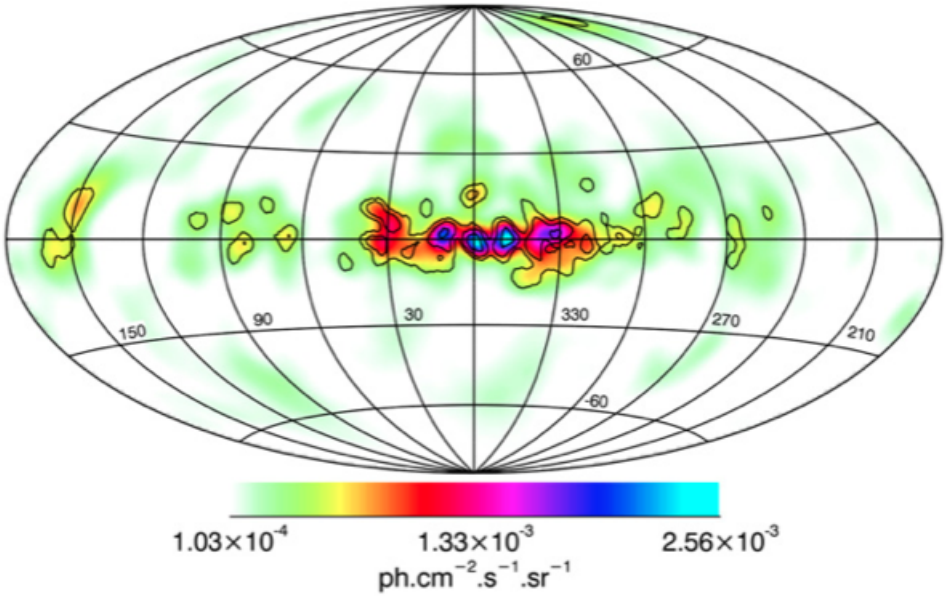

Fig. 1.2 Map of ^{26}Al in the Galactic plane produced by INTEGRAL [4].

^{26}Al is thought to be produced at the same site as ^{60}Fe which is produced in the final stages of massive star evolution. ^{60}Fe decays to ^{60}Co and ^{60}Ni, emitting gamma-ray lines of 1.173 and 1.333 MeV. These gamma-rays can also be detected, however, the radiation is too weak to derive a constraint on the spatial distribution of ^{60}Fe [4]. Satellites such as the Reuven Ramaty High Energy Solar Spectroscopic Imager (RHESSI) and SPI have measured the abundance ratio of ^{60}Fe/^{26}Al and the most recent calculation give the ratio to be 0.14, which agrees with supernova model predictions [4].

There are several stages in a massive stars lifetime when it may produce ^{26}Al, firstly in the hydrogen convective core of Wolf-Rayet stars, secondly with explosive

Ne/C burning during core collapse and, thirdly, in the pre-supernova star during C/Ne convective shell burning [13]. The focus of this work is the C/Ne convective shell of the pre-supernova star where T∼1.25 GK and Gamow window E_G=1.2-2.2 MeV. In order to understand the nucleosynthesis leading to its production it is first necessary to understand the nuclear burning over the lifetime of the star.

1.1.1 Massive Star Evolution

Massive stars are classified as stars with an initial mass M≥11$M_\odot$. They have much shorter lifetimes than lower mass stars and spend approximately 90% of their time on the main sequence converting hydrogen to helium via the CNO cycles. At lower temperatures it is the proton-proton (pp) chains which burn hydrogen into helium. The reactions involved in the pp chains are shown in Fig. 1.3. Each chain produces 26.73 MeV by converting four protons into one ^{4}He nucleus [2, 14].

pp1 chain	pp2 chain	pp3 chain
p(p,e$^+\nu$)d	p(p,e$^+\nu$)d	p(p,e$^+\nu$)d
d(p,γ)^{3}He	d(p,γ)^{3}He	d(p,γ)^{3}He
^{3}He(^{3}He,2p)α	^{3}He(α,γ)^{7}Be	^{3}He(α,γ)^{7}Be
	^{7}Be(e$^-$,ν)^{7}Li	^{7}Be(p,γ)^{8}B
	^{7}Li(p,α)α	^{8}B($\beta^+\nu$)^{8}Be
		^{8}Be(α)α

Fig. 1.3 The pp chains which burn hydrogen to helium [2].

Figure 1.4 shows how the energy generation rates of the pp1 chain and CNO cycle vary with temperature. At the higher temperatures achieved in the core of massive stars it is the CNO cycle which is dominant in energy production during hydrogen burning [2].

The overall effect of the CNO cycles is that $4^1\text{H} \rightarrow {}^4\text{He} + 2\text{e}^+ + 2\nu$ using C, N, O and F as catalysts. The CNO cycles are shown in Fig. 1.5. The main energy generation comes from the CNO1 cycle in which the slowest reaction is the ^{14}N(p,γ) reaction which acts as a bottleneck in the cycle producing a build up of ^{14}N [2].

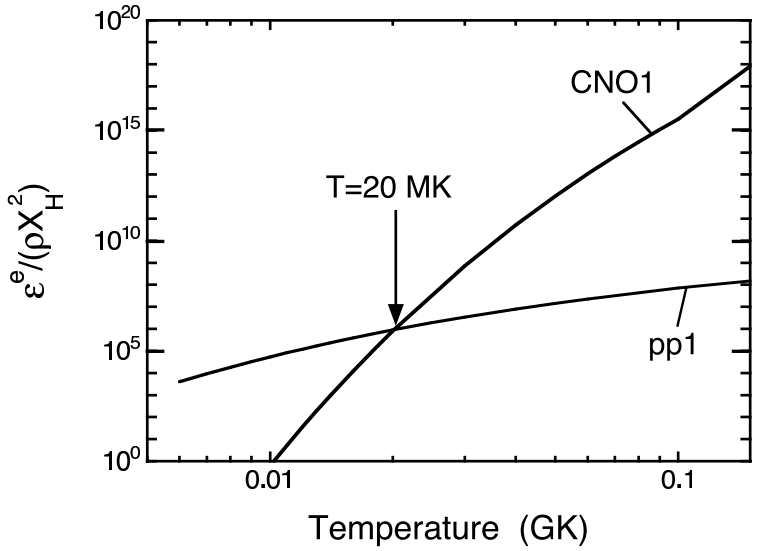

Fig. 1.4 Equilibrium energy generation rates ($\epsilon^e/(\rho X_H^2)$) of the pp1 chain and CNO1 cycle as a function of temperature [2].

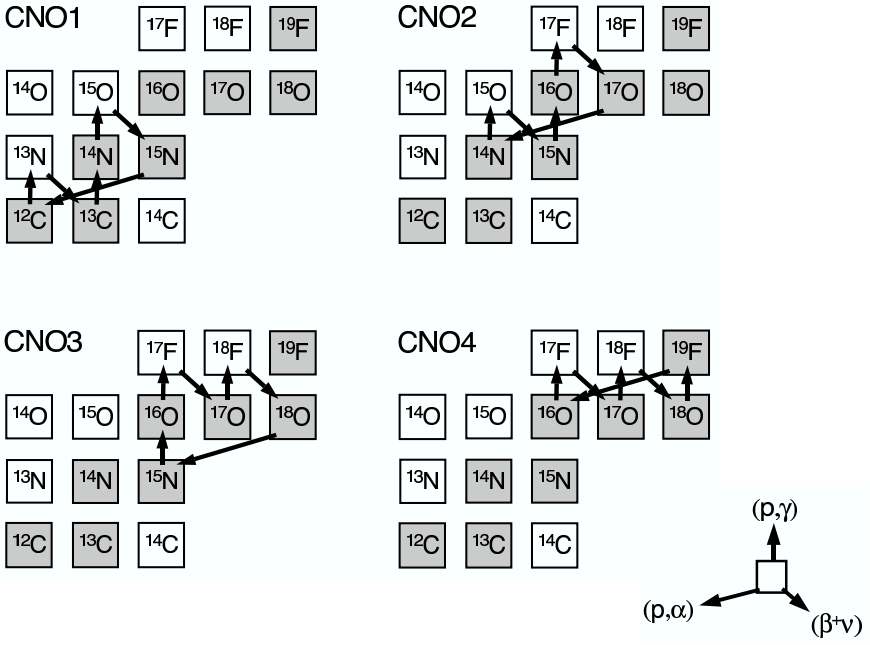

Fig. 1.5 Diagram showing the CNO cycles which burn hydrogen into helium. Stable nuclei are shown in grey boxes [2].

Proton induced reactions on unstable nuclei are of little importance as the radionuclides beta decay with short lifetimes. Nuclei with A≥20 are unlikely to be produced in the CNO cycle. However at higher temperatures the ^{19}F(p,γ)^{20}Ne reaction could provide a breakout to reaction chains involving heavier nuclei via the

NeNa and MgAl cycles shown in Fig. 1.6. These processes are important to note as ^{26}Al can be produced.

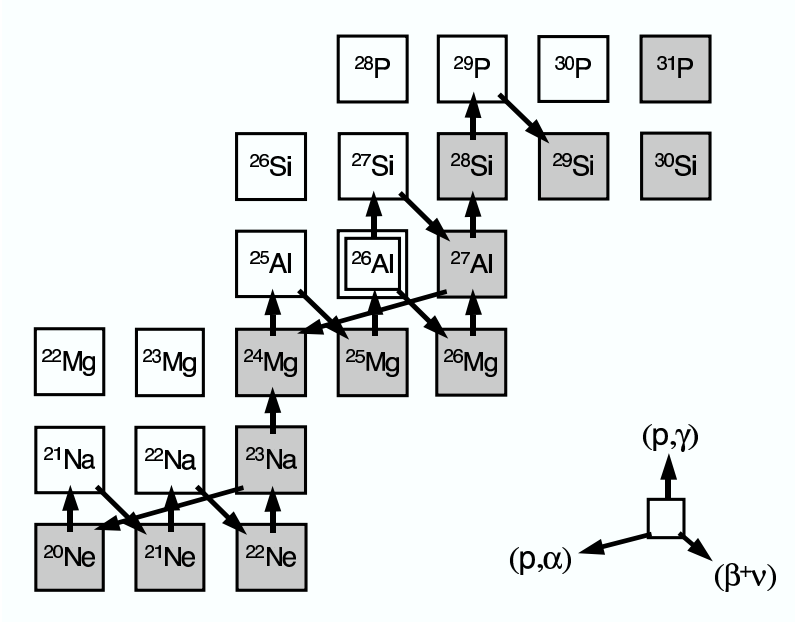

Fig. 1.6 The NeNa and MgAl cycles which take place during hydrostatic hydrogen burning. Stable nuclei are shown in grey boxes [2].

When the hydrogen in the core of the star has been converted to helium the star begins to contract under gravity and the temperature increases until helium burning is ignited in the core of the star halting the collapse. Helium burning occurs at temperatures of $T_9 \sim 0.2$ and densities of around 10^3g cm^{-3}. During this phase radiation pressure causes the outer layers of the star to expand and cool and the star enters the Red Giant phase of its life. Helium burning proceeds via the triple alpha process via the reactions

$$^4He + ^4He \leftrightarrow ^8Be \tag{1.1}$$

$$^8Be + ^4He \leftrightarrow ^{12}C^* \rightarrow ^{12}C + \gamma \tag{1.2}$$

^{8}Be is unstable and decays back to two ^{4}He particles with a lifetime of $T_{1/2} = 6.7\times10^{-17}$s. At the temperature and density relevant for He burning, the production rate becomes equal to the decay rate and there is a small probability ^{8}Be can capture

a further ^{4}He nucleus to produce ^{12}C. This process is made possible by the existence of the Hoyle state, a 0^+ resonance state near the alpha particle threshold in ^{12}C [14] which can subsequently decay to the ground state of ^{12}C.

As ^{12}C begins to build up ^{16}O is produced via the reaction ^{12}C(α,γ)^{16}O. The abundance ratio of ^{12}C to ^{16}O of $\approx$ 0.30 - 0.85 after helium burning suggests that this reaction is slow and so some ^{12}C remains after the helium burning phase. Subsequent alpha capture reactions ^{16}O(α,γ)^{20}Ne and ^{20}Ne(α,γ)^{24}Mg occur but do not contribute to the final abundances, with the final mass fractions of ^{20}Ne and ^{24}Mg, being $\approx 10^{-5}$ and $\approx 10^{-11}$, respectively after helium burning [2].

Once all the helium has been burnt in the core, the star begins to contract under gravity again. If a star has an initial mass M$\geq$8M$_{\odot}$ carbon burning will ignite at T$_9$ $\sim$ 0.8 and density of $\sim 10^5$g cm^{-3}. The main reactions involved in the carbon burning phase are:

$$^{12}C + ^{12}C \rightarrow ^{20}Ne + ^{4}He \tag{1.3}$$

$$^{12}C + ^{12}C \rightarrow ^{23}Na + p \tag{1.4}$$

$$^{12}C + ^{12}C \rightarrow ^{23}Mg + n \tag{1.5}$$

The most abundant nuclei in the core at the end of carbon burning are ^{16}O, which survives the burning, ^{20}Ne, ^{24}Mg and ^{23}Na [2]. Once carbon burning can no longer produce enough energy to withstand gravitational collapse the star contracts again and when the core temperature reaches T$_9$ $\sim$1.4 and the density reaches $\sim 10^7$g cm^{-3} neon burning is ignited in the core. Neon burning proceeds via the primary reaction ^{20}Ne(γ,α)^{16}O which produces α particles allowing the secondary reactions:

$$^{20}Ne(\alpha,\gamma)^{24}Mg(\alpha,\gamma)^{28}Si \tag{1.6}$$

$$^{23}Na(\alpha,p)^{26}Mg(\alpha,n)^{29}Si \tag{1.7}$$

The main energy producing reactions are ^{20}Ne(γ,α)^{16}O and ^{20}Ne(α,γ)^{24}Mg and so the neon burning stage of the stars life is characterised by these two reactions. At the end of the helium burning phase the most abundant nuclei in the core are ^{16}O and ^{24}Mg. Again the core contracts until it reaches a temperature of T_9 ~2 and a density of ~10^7g cm^{-3} at which point oxygen burning ignites in the core. There are many reactions involved in oxygen burning with the primary ones being:

$$^{16}O +^{16} O \rightarrow {}^{31}P + p \tag{1.8}$$

$$^{16}O +^{16} O \rightarrow {}^{30}Si + 2p \tag{1.9}$$

$$^{16}O +^{16} O \rightarrow {}^{28}Si +^{4} He \tag{1.10}$$

$$^{16}O +^{16} O \rightarrow {}^{24}Mg + 2^{4}He \tag{1.11}$$

$$^{16}O +^{16} O \rightarrow {}^{30}P + d \tag{1.12}$$

$$^{16}O +^{16} O \rightarrow {}^{31}S + n \tag{1.13}$$

At the end of oxygen burning the core is 90% ^{28}Si and ^{32}S [14]. Again the core contracts and when the temperature reaches T_9 ~3.5 and density reaches ~10^8g cm^{-3} silicon burning begins [14]. Photodisintegration of less tightly bound nuclei occurs via reactions such as:

$$^{28}Si + \gamma \rightarrow {}^{24}Mg + \alpha \tag{1.14}$$

$$^{24}Mg + \gamma \rightarrow {}^{20}Ne + \alpha \tag{1.15}$$

Alpha, proton and neutron capture of the liberated particles leads to heavier and heavier elements being produced in a complex chain of reactions leading towards the Fe peak. When silicon burning comes to an end the star has an onion structure. After each burning stage ends in the core, burning shells form around the core which has moved onto the the next stage of burning and so the star ends with a core which

consists primarily of ^{56}Fe and ^{52}Cr. Figure 1.7 shows this onion-like structure before core collapse occurs.

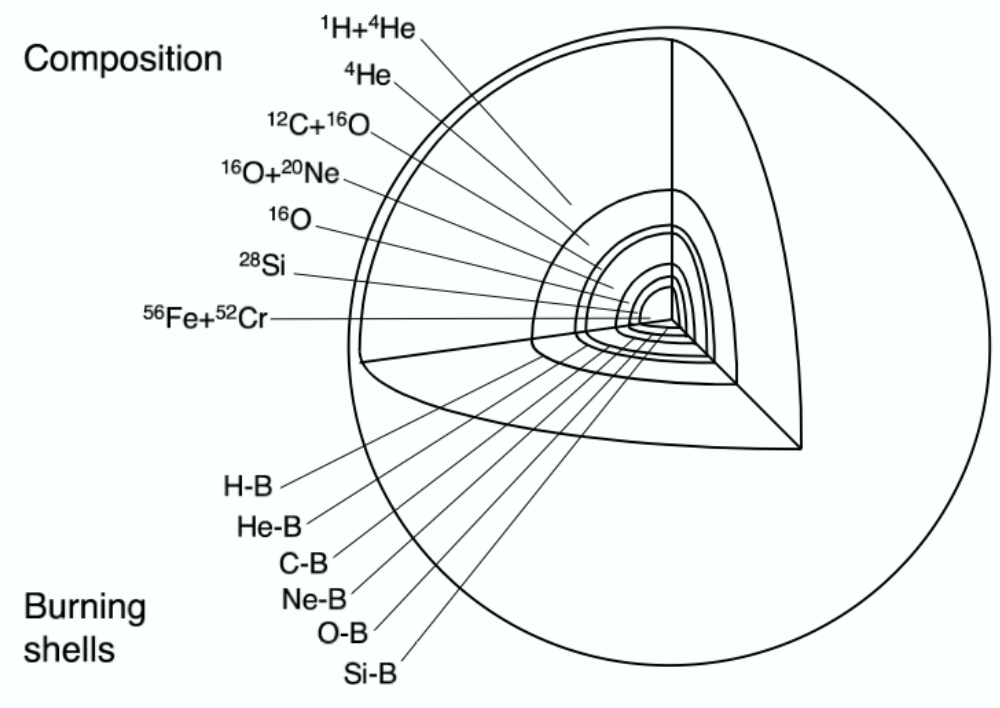

Fig. 1.7 Diagram showing the onion structure of a massive star at the end of silicon burning. The upper left side shows the most abundant nuclei in the shell labelled, the lower left side shows the burning shells around the core [2].

The core collapses until it becomes electron degenerate at which point the collapse is halted. However the ashes from the shells burning around the core continue to add to the mass of the electron degenerate core until it exceeds the Chandrasaker mass limit of 1.4M$_{\odot}$. At this point electron degeneracy can no longer counteract gravity and the core begins to collapse again. As the core collapses, and electron density increases, electrons are captured by nuclei, reducing the number of electrons contributing to electron degeneracy pressure and accelerating the collapse. As well as this, as the temperature increases, iron peak nuclei are photodisintegrated into lighter nuclei, removing energy that could have contributed to the pressure.

The core continues to collapse until it overshoots the nuclear density of $\approx 10^{14}$ g cm^{-3} at which point nuclei begin to feel the short-range nuclear force. The nuclear force is repulsive at short distances resulting in a rebound of the inner core. The rebounding inner core collides with the in-falling outer layers of the core, creating a

shock wave that propagates outwards compressing and heating the outer layers of the star resulting in explosive burning in the shells. The outer layers of the star are blown off and the core of the star becomes a neutron star or a black hole.

1.1.2 ^{26}Al Production in the C/Ne Convective Shell

In order to predict the abundance of ^{26}Al produced in massive star evolution Iliadis *et al.* [13] carried out detailed network calculations for three burning scenarios. Firstly during hydrogen burning in the core of Wolf-Rayet stars, secondly with explosive Ne/C burning during core collapse and thirdly in the pre-supernova star during C/Ne convective shell burning [13].

In the case of the C/Ne convective shell the network calculation uses the temperature-density-time profile from the stellar evolution code of a 60M$_\odot$ star with an initial solar metallicity used by Limongi and Chieffi [11]. The time axis of the profile is compressed by a factor of 60 to reproduce the effects of convection in the post processing model. Convection brings fresh fuel to the burning region as well as carrying away fragile nuclei from the burning region which lengthens the timescale of nuclear burning. Therefore in order to use this profile in a post processing code they must compress the time axis to prevent the fuel being destroyed faster than in the stellar evolution model.

Thermal Equilibrium of ^{26}Al

A level scheme for ^{26}Al decaying to ^{26}Mg is shown in Figure 1.8. The ground state of ^{26}Al beta decays to several excited states in ^{26}Mg with a half life of T$_{1/2}$=7.17$\times$10^{5}y. Some of these excited states decay to the first excited state in ^{26}Mg, which lies at 1.809 MeV, and the consequent decay ^{26}Mg to its ground state results in the observed gamma-ray line.

The first excited state in ^{26}Al is an isomer, which decays to the ground state in ^{26}Mg without the emission of the 1.809 MeV gamma-ray, and with a half-life of T$_{1/2}$ = 6.34 s. This is due to the large angular momentum difference between

the 0^+ first excited state and the 5^+ ground state in ^{26}Al. The ground state and first excited state in ^{26}Al are therefore linked via thermal excitations to higher excited states. At temperatures above T∼0.4 GK [15] the ground state, ^{26}Al^g and isomer ^{26}Al^m fall into thermal equilibrium. This means their abundance ratio can be determined from the Boltzmann distribution and the internal equilibrium method is not important. Therefore they can be treated as one species, ^{26}Al^t. At lower temperatures they fall out of thermal equilibrium and act as two species which decay with their characteristic half lives.

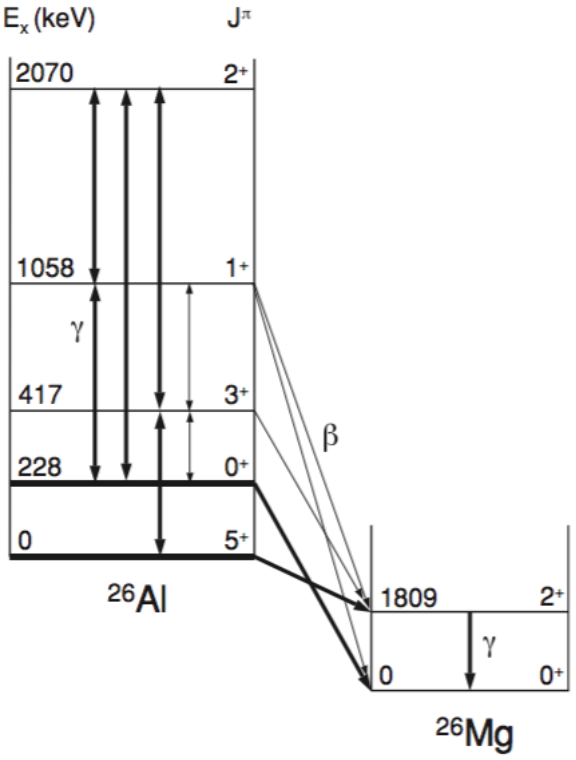

Fig. 1.8 The level scheme for the decay ^{26}Al to ^{26}Mg [2].

^{26}Al Production in the C/Ne Convective Shell

The temperature and density of the carbon burning shell is not usually enough for a substantial amount of ^{26}Al to be produced. In becomes possible as the star begins to contract and heat up and mixing occurs. The burning in the model begins with a temperature of T_9 ∼1.13 and density of 6.3×10^4 g/cm^3 and ends with a temperature of T_9 ∼1.44 and density of 1.1×10^5 g/cm^3. The time for the profile is 5.24×10^4 s.

The most abundant nuclei at the beginning of the burning are ^{16}O, ^{12}C and ^{20}Ne. Burning proceeds primarily through the main carbon burning reactions:

$$^{12}C +^{12} C \rightarrow {}^{20}Ne +^{4} He \tag{1.16}$$

$$^{12}C +^{12} C \rightarrow {}^{23}Na + p \tag{1.17}$$

These release alpha particles and protons which fuel the secondary reactions, building up towards ^{26}Al:

$$^{16}O +^{4} He \rightarrow {}^{20}Ne + \gamma \tag{1.18}$$

$$^{23}Na + p \rightarrow {}^{20}Ne +^{4} He \tag{1.19}$$

^{26}Al is produced mainly by the reaction ^{25}Mg(p,γ)^{26}Al^{t}. ^{25}Mg is produced via the reactions ^{22}Ne(α,n)^{25}Mg, which is also the main neutron source, and ^{24}Mg(n,γ)^{25}Mg shown in Fig.1.9. The low neutron abundance means that the main destruction of ^{26}Al^{t} is through its beta decay to ^{26}Mg.

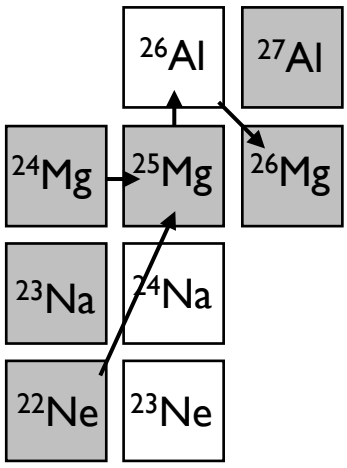

Fig. 1.9 The reaction chain for the production and destruction of ^{26}Al in the C/Ne convective burning shell of massive stars. The arrows indicate the reactions used to produce and destroy ^{26}Al. Grey boxes represent stable nuclei.

The main proton producing reaction for the production of ^{26}Al is the ^{12}C(^{12}C,p)^{23}Na, with the second most important proton production reaction being ^{23}Na(α,p)^{26}Mg. The Iliadis [2] study varied the reaction rates of 66 forward and reverse reactions, and Table 1.1 shows the list of most influential reactions found by the study. The other reactions and the abundance changes listed "..." in the table changed the final amount of ^{26}Al by less than 20%. It is the fourth most important reaction ^{23}Na(α,p)^{26}Mg that is the focus of this thesis.

Reaction	Rate Multiplied By				Uncertainty
	10	2	0.5	0.1	
^{23}Na(p,α)^{20}Ne	0.15	0.61	1.6	4.2	6%
^{26}Al^{t}(n,p)^{26}Mg	0.16	0.65	1.4	1.9	
^{25}Mg(p,γ)^{26}Al^{t}	6.2	2.0	0.46	0.10	5%
^{23}Na(α,p)^{26}Mg	3.0	1.3	...	0.71	
^{26}Mg(α,n)^{29}Si	0.40	0.83	...	1.3	29%
^{24}Mg(n,γ)^{25}Mg	2.1	1.3	...	0.70	

Table 1.1 The table shows the nuclei and abundance changes produced by varying the reaction rates assuming a single species of ^{26}Al during convective shell C/Ne burning. Abundance changes denoted "..." indicate less than 20% change in the final amount of ^{26}Al [13].

Due to insufficient data a statistical-model cross-section calculation was used to calculate a reaction rate for the ^{23}Na(α,p)^{26}Mg reaction in the network calculations. Previous experimental measurements of this reaction will be discussed in the next chapter. This reaction was therefore highlighted as being of great importance for a cross section measurement so that better constraints of nucleosynthesis models could be applied. It is this reaction that forms the core of this thesis.

1.2 Type 1a Supernovae

Type Ia supernovae are important astrophysical objects as the nature of their peak luminosity curve means that they can be used as standard candles to measure cosmological distances. They are also important for the chemical evolution of

galaxies as they are responsible for the production of most of the Fe peak nuclides and are a key target for gamma-ray astronomy [16]. However, the astrophysical scenario by which they come about is still not understood, with many models still being proposed. It is possible that more than one model is needed to explain the observed SN1a.

Unlike type II supernovae which are powered by core collapse, type I supernovae are powered by thermonuclear explosions resulting from thermonuclear runaway reactions. The favoured explosion mechanism which describes the majority of SN1a is the carbon-oxygen white dwarf in a binary star system with a main sequence star or Red Giant. A carbon oxygen white dwarf is the end point of a star with initial mass $M<8M_{\odot}$. After the helium burning phase the core of the star begins to collapse and the outer layers are blown off becoming a planetary nebula. Temperatures do not reach the temperature needed to ignite carbon burning and so the star ends its life as a degenerate core of carbon and oxygen.

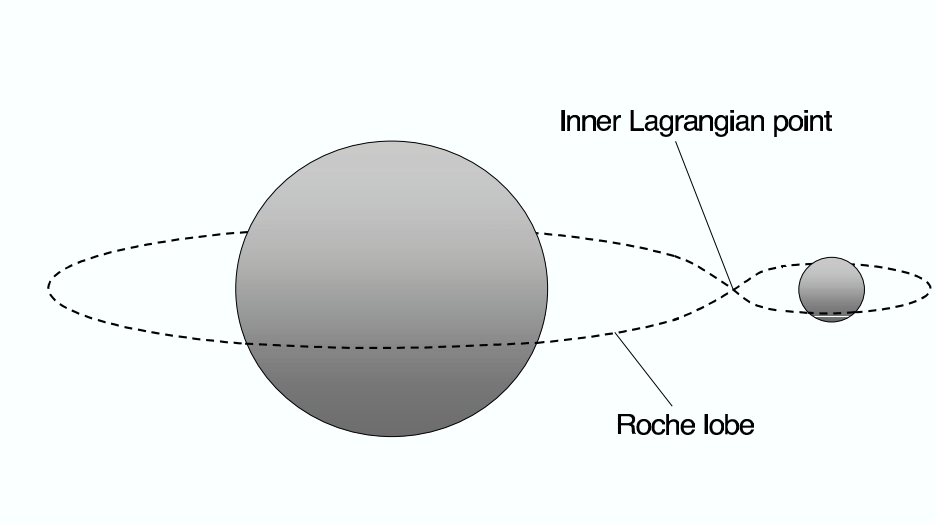

Fig. 1.10 Binary system of two stars, the point where the two Roche Lobes touch is called the Lagrangian point [2].

Figure 1.10 shows a diagram of a pair of stars in a binary system. The Roche Lobe represents the region around a star in which orbiting material is gravitationally bound to the star. Where the Roche lobes of the two stars touch is the Lagrangian point. In this system, matter from the periphery of the companion star is accreted

onto the surface of the white dwarf until a mass near the Chandrasaker mass limit is reached and carbon burning ignites under degenerate conditions [2]. The degenerate conditions mean that temperature and pressure are decoupled and so as the star heats up it does not expand and cool, leading to thermonuclear runaway. There are two theories as to how the burning flame propagates through the star. The first is a supersonic detonation where the shock front heats the fuel. The second is subsonic deflagration whereby hot burning material heats the next layer of material.

At temperatures of $\sim 5.5 \times 10^9$K and densities of $\sim 10^8$ g cm^{-3}, nuclear statistical equilibrium (NSE) is achieved and the the nuclear reactions no longer depend on reaction rates but on bulk properties of the nucleus such as mass [16]. Freeze-out occurs when temperatures and densities decrease to where reaction equilibrium is no longer possible.

The abundance pattern of the ejecta is characterised by five burning regimes [17]. The first regime consists of normal and alpha rich freeze-out reactions from NSE in the inner regions of the star. Normal freeze-out occurs due to a lack of alpha particles which are necessary to maintain NSE. In alpha-rich freeze-out the free alpha particles merge in successive (α,γ) reactions leading to the iron peak [2]. The outer layers of the star undergo incomplete Si burning, explosive oxygen burning and C/Ne burning. Figure 1.11 shows the burning zones as the deflagration wave propagates outwards.

Temperatures increase to reach 10^9 and 10^{10}K and the explosion and nucleosynthesis lasts only a few seconds. The energy released is enough to unbind the whole star and it ejects all material into the interstellar medium. The importance of type Ia supernovae as standard candles in astrophysics has meant that a lot of effort is put into understanding the mechanism behind the explosion.

Bravo *et al.* [16] carried out post processing calculations varying 1099 pairs of reaction rates by factors of 0.1 and 10. The species ^{14}N, ^{21}Ne, ^{23}Na, ^{29}Si, ^{32}P, ^{33}S, ^{37}Cl, ^{40}Ca, ^{45}Sc, ^{44,47}Ti showed an increase by a factor of between 0.12 and 2 for a

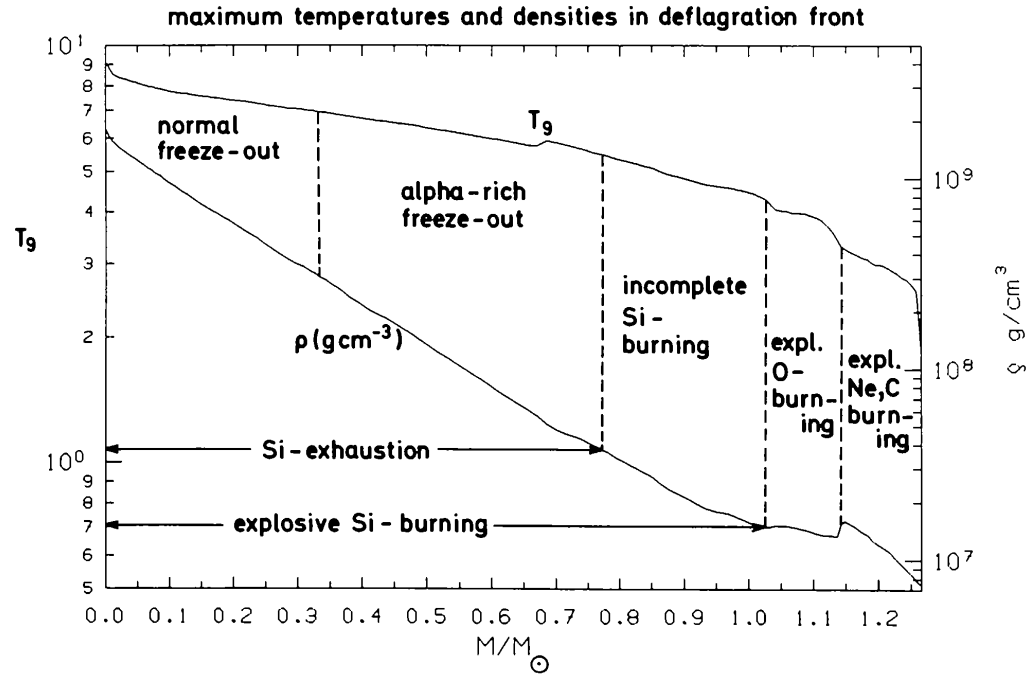

Fig. 1.11 The zones of different explosive burning as a function of Lagrangian mass coordinate $M/M_\odot$ and temperatures and densities achieved during the outward propagation of the deflagration burning front for type 1a supernovae. [18].

factor of ten increase in the ^{23}Na(α,p)^{26}Mg reaction rate and the nuclei ^{26}Mg and ^{43}Ca showed a factor of at least 2 increase if the reaction rate is increased by 10.

Parikh *et al.* also carried out detailed network calculations using several explosion models, the ^{23}Na(α,p)^{26}Mg reaction was found to influence abundances of several nuclei. They found that when the reaction rate was increased by a factor of ten the ^{23}Na abundance changed by a factor of 0.47, ^{24}Na changed by a factor of 0.3 and ^{53}Cr changed by a factor of 2.1. In each case, rather than using experimental data, the Hauser Fesbach statistical model calculations were used to calculate a reaction rate. As discussed in the next chapter, the applicability of the statistical model is uncertain for these circumstances. An experimental measurement of the cross-section is essential.

Chapter 2

Astrophysical Reaction Rates

2.1 Astrophysical Reaction Rate

The aim of this work is to measure cross sections for the reaction ^{23}Na(α,p)^{26}Mg in order to calculate a reaction rate for temperatures relevant to C/Ne convective shell burning in massive stars. If we consider two particles in a plasma with number densities n_A and n_B particles per unit volume interacting such that:

$$A + B \rightarrow C + D. \tag{2.1}$$

The likelihood of this reaction occurring will depend on the number densities of A and B, n_A and n_B, the reaction cross section σ and the relative velocity, v of the particles A and B [19]. The reaction rate is given by:

$$R_{AB} = n_A n_B \sigma v. \tag{2.2}$$

In general the statistical distribution of velocities for particles inside a stellar gas can be described by the Maxwell-Boltzmann distribution which describes the distribution of relative velocities v as [19]:

$$\phi(v) = 4\pi v^2 \left(\frac{\mu_{AB}}{2\pi k_B T}\right)^{\frac{3}{2}} exp\left(-\frac{\mu_{AB} v^2}{2k_B T}\right) \tag{2.3}$$

where k_B is the Boltzmann constant, μ_{AB} is the reduced mass of particles A and B and T is temperature. The total reaction rate summed over all velocities is [19]:

$$R_{AB} = n_A n_B \langle \sigma v \rangle \tag{2.4}$$

where $\langle \sigma v \rangle$ is the average value of the product of σv given by [19]

$$\langle \sigma v \rangle = \int_0^\infty \sigma v \phi(v) dv. \tag{2.5}$$

Transforming the variable of integration to energy as $E = \frac{1}{2}\mu v^2$, the reaction rate can be written in terms of energy as [19]

$$\langle \sigma v \rangle = \sqrt{\frac{8}{\pi \mu_{AB} (k_B T)^3}} \int_0^\infty E \sigma(E) exp\left(-\frac{E}{k_B T}\right) dE. \tag{2.6}$$

In low-energy astrophysical environments reaction cross sections drop rapidly with energy due to Coulomb barrier repulsion. In order to extrapolate to lower astrophysically relevant energies it can be useful to use the astrophysical S factor which varies much more slowly with energy [19]. The astrophysical S factor, S(E), is defined such that

$$\sigma(E) = \frac{1}{E} exp(-2\pi\eta) S(E), \tag{2.7}$$

where

$$\eta = \frac{Z_A Z_B e^2}{4\pi\epsilon_0 \hbar v}. \tag{2.8}$$

Here $Z_A Z_B e^2$ is the product of charges and v is the relative velocity of the incident particles [19]. The exponential factor represents penetrability through the Coulomb barrier [19]. The reaction rate can also be rewritten substituting the cross section for the S factor into equation 2.6 [19] as

$$\langle \sigma v \rangle = \sqrt{\frac{8}{\pi \mu_{AB} (k_B T)^3}} \int_0^\infty S(E) exp\left(-\frac{E}{k_B T} - \sqrt{\frac{E_G}{E}}\right) dE. \tag{2.9}$$

The energy constant E_G is given by

$$E_G = 4\pi^2\eta^2 E = \frac{2\mu_{AB}}{\hbar^2}(\pi Z_A Z_B e^2)^2 \tag{2.10}$$

The product of the two exponential terms in Equation 2.9 gives a value for the integral which has a peak at the effective burning energy, this is the Gamow energy which is the energy where the reaction is most likely to occur [19]. Figure 2.1 shows the Gamow peak which has an energy E_0 given by

$$E_0 = \left(\frac{E_G k_B^2 T^2}{4}\right)^{\frac{1}{3}} \tag{2.11}$$

and a width Δ given by

$$\Delta = \frac{4}{3^{\frac{1}{2}}}(E_0 k_B T)^{\frac{1}{2}} \tag{2.12}$$

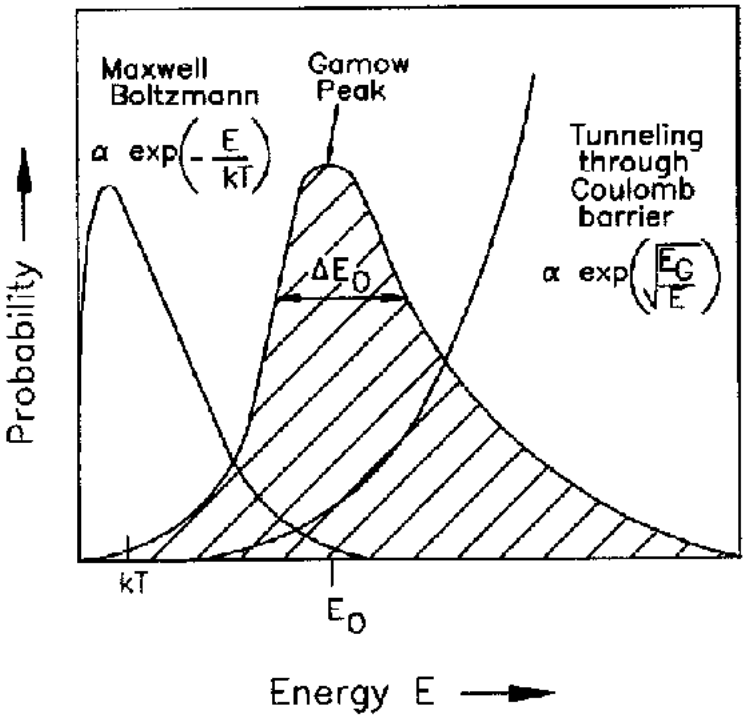

Fig. 2.1 The product of the tunnelling probability and the Maxwell-Boltzmann probability results in the Gamow peak energy which is the effective burning energy. Note that here the height of the Gamow peak has been exagerated so that it is shown clearly with the Maxwell-Boltzmann probability and the tunnelling probablilty curves. Figure taken from Ref [20].

The reaction rate derived above is the energy-averaged reaction rate. If a resonance is present the Breit-Wigner resonance cross section is substituted into Equation 2.6 [19]. The single level Breit-Wigner cross section for resonance p is given by

$$\sigma_{BW}(E) = \frac{\pi}{k^2} g_{J_{tot}} \frac{\Gamma_{p\alpha}\Gamma_{p\alpha'}}{(E-E_p)^2 + \frac{\Gamma_p^2}{4}}, \tag{2.13}$$

where $g_{J_{tot}}$ is the spin weighting factor given by

$$g_{J_{tot}} = \frac{2J_{tot}+1}{(2J_A+1)(2J_B+1)}, \tag{2.14}$$

where k is the wave number equal to $p^2/\hbar^2$, $\Gamma_{p\alpha}$ and $\Gamma_{p\alpha'}$ are the partial width of the entrance and exit channels respectively and Γ_p is the total width of the excited state in compound nucleus. J_{tot} is the angular momentum of the excited state in the compound nucleus J_A and J_B are the angular momentum of particle A and B and E_p is equal to the energy of the resonance [19].

This gives a resonant reaction rate per particle pair of

$$\langle \sigma v \rangle = \left(\frac{2\pi}{\mu_{AB} k_B T}\right)^{\frac{3}{2}} \hbar^2 g_{j_{tot}} \frac{\Gamma_{p\alpha}\Gamma_{p\alpha'}}{\Gamma_p} exp\left(-\frac{E_p}{k_B T}\right). \tag{2.15}$$

2.2 Hauser-Feshbach Model

In the case of the ^{23}Na(α,p)^{26}Mg reaction, post processing model calculations have utilised the Hauser-Feshbach theoretical cross section calculations to calculate the rate. This is the cross section averaged over any resonance structure, the energy averaged cross section. The equation for the energy averaged Hauser-Feshbach formula [19] is derived by summing over Breit-Wigner resonances and is given by

$$\langle \sigma_{re}(\alpha, \alpha') \rangle = \frac{\pi}{k^2} \sum_{J\pi} g_{J_{tot}} W_{\alpha\alpha'} \frac{T_\alpha T_{\alpha'}}{\sum \alpha'' T_{\alpha''}}, \tag{2.16}$$

where α is the incoming channel and α' is the outgoing channel. The sum over α'' is the sum over all channels that are energetically possible for the decay of the compound nucleus. Transmission coefficients T_α describe the formation probability of single-particle levels and are calculated using optical-model potentials which represent the average nuclear potential [2]. $W_{\alpha\alpha'}$ is the width fluctuation factor.

The applicability of this model depends on several factors, firstly, the energy of the incident nucleus must be sufficiently low that a compound nucleus reaction will take place. These compound nucleus reactions are lower in energy than direct reactions which are faster, meaning all nucleons interact and form a compound nucleus. The compound nucleus processes have less memory about direction than direct reactions and are usually symmetric around 90^o [14]. As well as this, the level density in the energy range of the reaction in the compound nucleus must be sufficiently high for a statistical approach to be taken into account. In the case of the ^{23}Na(α,p)^{26}Mg reaction, in the energy range measured in this work the model is not expected to be accurate due to the low level density in the compound nucleus of approximately 5 states per 100 keV [7]. However, since an estimate of reaction rate was needed for astrophysical models, the calculations were carried out. The statistical model calculations used in this work were carried out by Thomas Rauscher using the codes NON-SMOKER [21] and SMARAGD [22].

Chapter 3

Previous Measurements and Current Status

The cross section of the ^{23}Na(α,p)^{26}Mg reaction has been measured in previous works by Kuperus [23] and Whitmire and Davids [24]. It has also been measured during the course of this thesis by Almaraz-Calderon *et al.* [25] and by Howard *et al.* [26], the latter of which published their work at the same time as this thesis data were published. These measurements are discussed in this chapter.

3.1 Early Experiments

In 1954 Temmer and Heyenburg [27] measured the γ-ray yield from the ^{23}Na(α,p)^{26}Mg* reaction in the energy range $E_{c.m.}$=1.3 - 3.1 MeV. However, they did not measure a cross section or resonance strength needed to calculate an astrophysical reaction rate and so further work was needed [24].

In 1964 Kuperus [23] carried out an experiment using an alpha-particle beam incident on NaCl targets evaporated onto thick copper backings. Measurements were made in the energy range $E_{c.m.}$ = 0.9 - 2.8 MeV and 38 resonances were observed. However because only protons to the ground state in ^{26}Mg, referred to as p_0 protons, were measured the reaction rate calculated from this work was considered incomplete

as protons from higher excited states in ^{26}Mg are expected to make a substantial contribution to the cross section [24].

In a similar setup, Whitmire and Davids [24] carried out an experiment using copper backed NaCl targets and a ^{4}He beam. Measuring protons from reactions to the first excited state in ^{26}Mg, referred to as p_1 protons, they determined the resonance strengths for 30 new p_1 resonances as well as measuring 9 new p_0 resonances from reactions to the ground state. The measurement was made in the energy range $E_{c.m.}$ = 2.0 - 3.1 MeV. During the experiment they noted that the melting temperature of the NaCl targets is 801°C which meant that at beam intensities just higher than those used the targets would evaporate. The targets were therefore monitored for evaporation by comparing the yield from the same resonance on the same target spot after 10 to 20 hours of bombardment [24]. The strengths were calculated assuming a target stoichiometry of 1:1 for the NaCl targets relative to an absolute strength measurement for the resonance at E_{lab} = 3.051 MeV. A reaction rate was then calculated and found to be enhanced by a factor of four at T=3 GK and three at T=2 GK compared to the reaction rate calculated from the work by Kuperus.

Despite this measurement being made the reaction network calculation studies chose to use the recommended rate calculated using Hauser-Feshbach cross sections. According to work by Paine et al. [28] at the beam current used during the experiment by Whitmire and Davids the Na/Cl ratio would change from 1:1 to 5:3 in $\sim$ 200 seconds [28, 29]. This would mean that the stoichiometry used to calculate the resonance strengths and therefore the astrophysical reaction rate could have been calculated using the wrong target stoichiometry. As well as this, the uncertainty on the resonance energies is $\approx$10 keV which is relatively large and the energy range covered does not cover a reliable portion of the Gamow window for C/Ne convective shell burning at T$\sim$1.25 GK and E_G=1.2 - 2.2 MeV. This led to the statistical model rate being used in astrophysical models.

3.2 Recent Measurement in Inverse Kinematics

The data for this thesis were taken over three sets of beam time. The first set of data was measured and analysed followed by a further two sets of measurements. During the data analysis of the first set of measurements, Almaraz-Calderon *et al.* [25] carried out an experiment in inverse kinematics using a ^{23}Na beam on a cryogenic ^{4}He gas cell target. The entrance and exit windows to the target were made of titanium foils. The experimental setup is shown in Figure 3.1. The protons resulting from the ^{23}Na(α,p)^{26}Mg reaction were detected in the silicon detector and α-particles scattered in the target were stopped in the aluminium foil. The monitor detector was used to monitor the beam intensity via scattering of the beam from the gold foil.

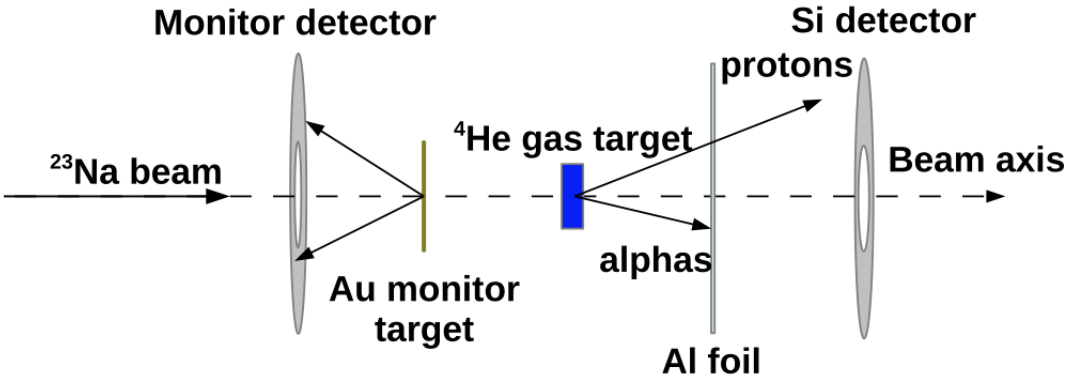

Fig. 3.1 The setup for the experiment carried out at Argonne National Laboratory by Almaraz-Calderon *et al.* [25]

Cross sections, shown in Fig. 3.2, were extracted for ^{23}Na(α,p_0)^{26}Mg at three energies and an upper limit of the cross section was found for the lowest energy data point. Cross sections for ^{23}Na(α,p_1)^{26}Mg were extracted at the two higher energy data points. The two lower energy p_1 cross sections are found by extrapolating the fit of the CIGAR Hauser-Feshbach calculation to the data. To calculate the total cross sections the p_0 and p_1 cross sections are summed. To calculate an angle integrated cross section, the angular distributions from the ^{27}Al(α,p)^{30}Si reactions were used. This reaction has a similar J^{π} configuration to the ^{23}Na(α,p)^{26}Mg reaction and so it was thought the angular distributions would be similar.

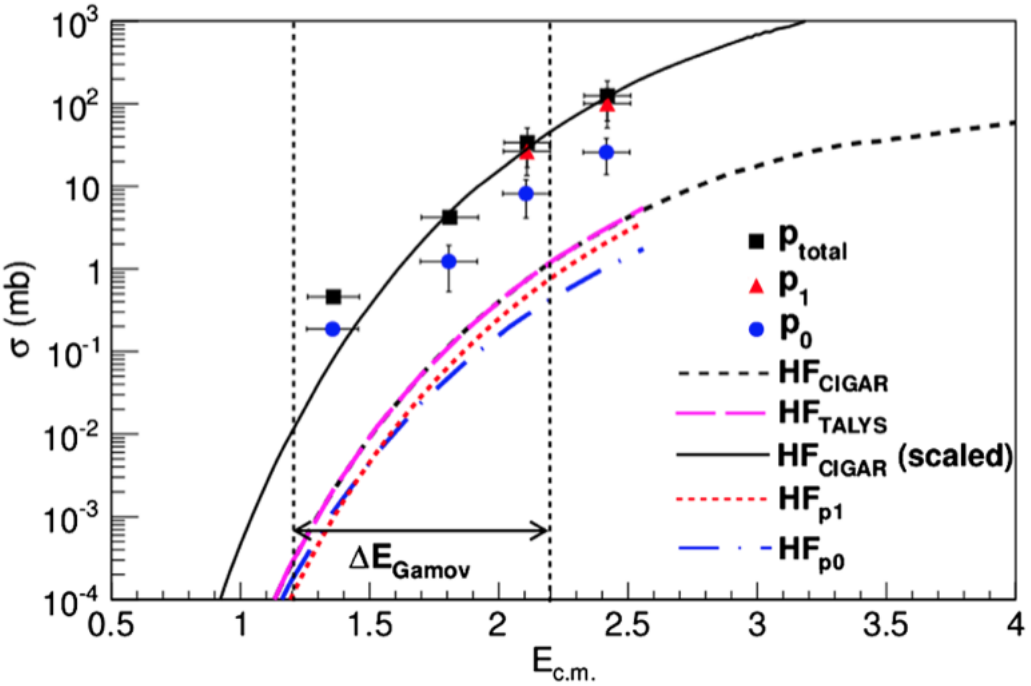

Fig. 3.2 Cross sections calculated by Almaraz-Calderon *et al.* compared to various Hauser Feshbach model calculations [25]. See text for details of the Hauser Feshbach model predictions.

The Gamow window shown in the cross section plot in Fig. 3.2 is the Gamow window for C/Ne convective shell burning in massive stars. The cross sections are compared to the HF cross sections calculated by the codes TALYS and CIGAR.

Figure 3.3 shows the reaction rate calculated using the total cross sections calculated in their work plotted with the JINA REACLIB [21] recommended rate which is the same as the rate used by Illiadis *et al.* in the reaction network calculations. The reaction rate is a factor of 40 higher than the recommended rate. This result was very significant since a factor of ten increase in the reaction rate changes the abundance of ^{26}Al produced in the C/Ne convective shell of massive stars by a factor of 3.

This result was found to not fit the trend by a study by Mohr [30]. He investigated the cross sections of α-induced reactions on nuclei in the mass range A$\approx$20-50 by comparing the reduced cross sections of data and calculations by the statistical models. In order to compare data from different nuclei the reduced energy and reduced cross section is calculated. The reduced energy takes into account the different heights

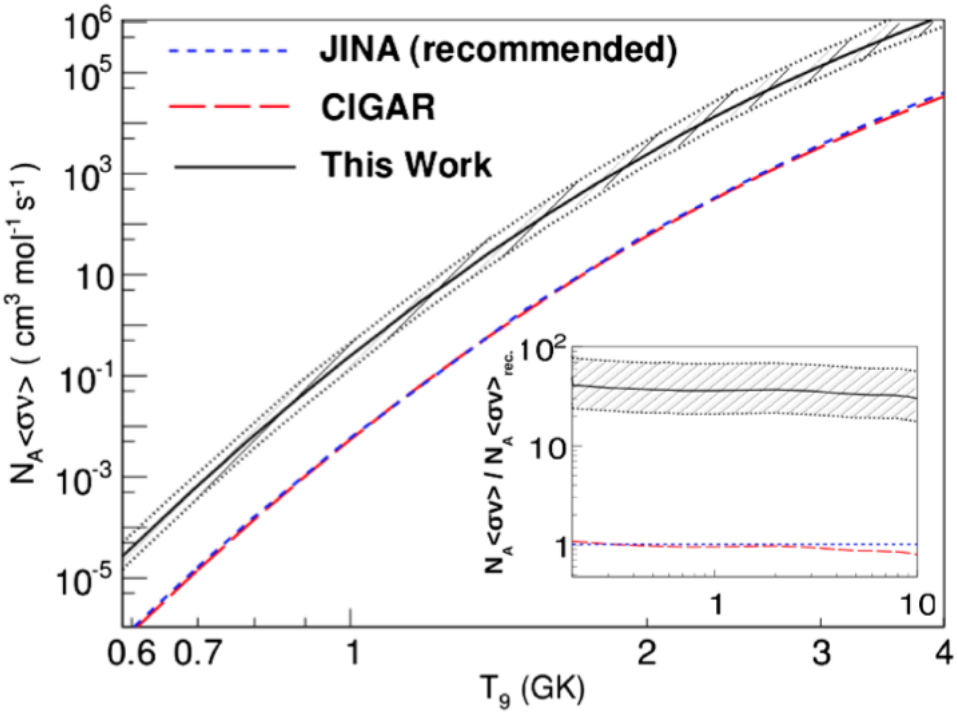

Fig. 3.3 Reaction rate calculated by Almaraz-Calderon *et al.* compared to the JINA recommended rate and the rate calculated using the Hauser Feshbach cross sections calculated using the code CIGAR [25].

of the Coulomb barrier for the different nuclei. The reduced cross section scales the measured total reaction cross sections according to the geometrical size of the projectile-plus-target system. In general these reduced cross sections are similar in value and in trend, however the experimental data for ^{23}Na by Almaraz-Calderon *et al.* was one of four nuclei that did not follow the trend.

Figure 3.4 shows the reduced cross sections calculated from the cross sections published in Almaraz-Calderon *et al.* compared to the reduced cross section trend of statistical model calculations. The cross sections from the work by Almaraz-Calderon *et al.* are larger when compared to reduced cross sections and the trend is steeper than expected.

3.3 Measurement in forward kinematics

A further measurement of the ^{23}Na(α,p)^{26}Mg reaction cross section was made in forward kinematics by Howard *et al.* [26] in the energy range $E_{c.m.}$ =1.7 - 2.5 MeV.

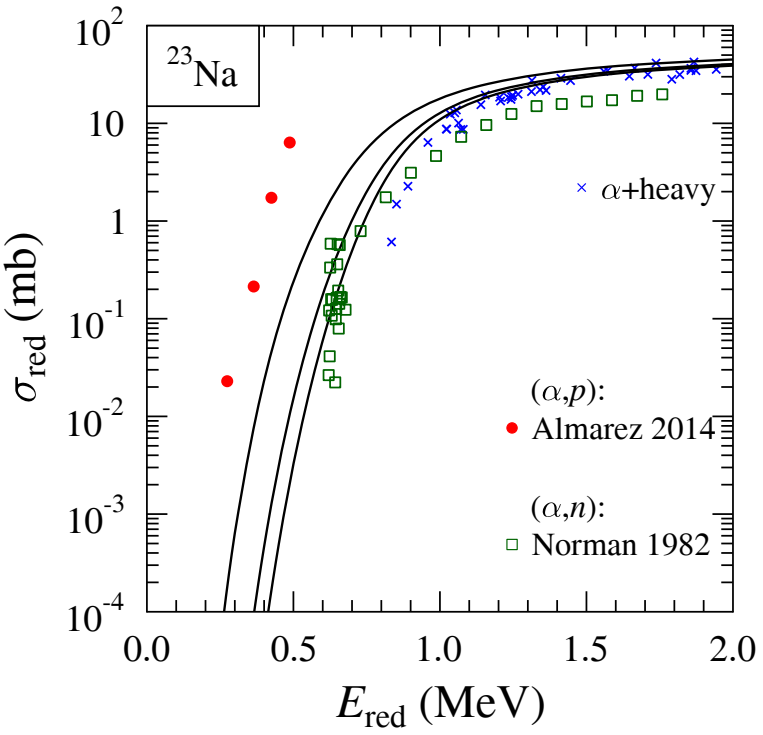

Fig. 3.4 Reduced cross sections of alpha induced reactions on ^{23}Na. The black solid lines show the statistical model calculations from left to right for ^{21}Ne, ^{36}Ar and ^{51}V. [30]

A ^{4}He beam was incident on a carbon backed NaCl target. The protons from ^{23}Na(α,p_0)^{26}Mg and ^{23}Na(α,p_1)^{26}Mg were detected by a silicon detector array. By simultaneously detecting Rutherford scattered alpha particles they were able remove the dependencies on properties of the target which caused uncertainty in previous forward kinematics measurements.

Howard *et al.* were able to extract angular distributions from their data and calculated total cross sections at 8 energies. The cross sections are shown in Fig. 3.5 and are compared to the cross sections calculated by Howard *et al.* It can be seen that the cross sections are in good agreement with the NON-SMOKER cross sections and disagree with the cross sections produced by Almaraz-Calderon *et al.* The work by Howard *et al.* was published simultaneously with the work from this thesis [31].

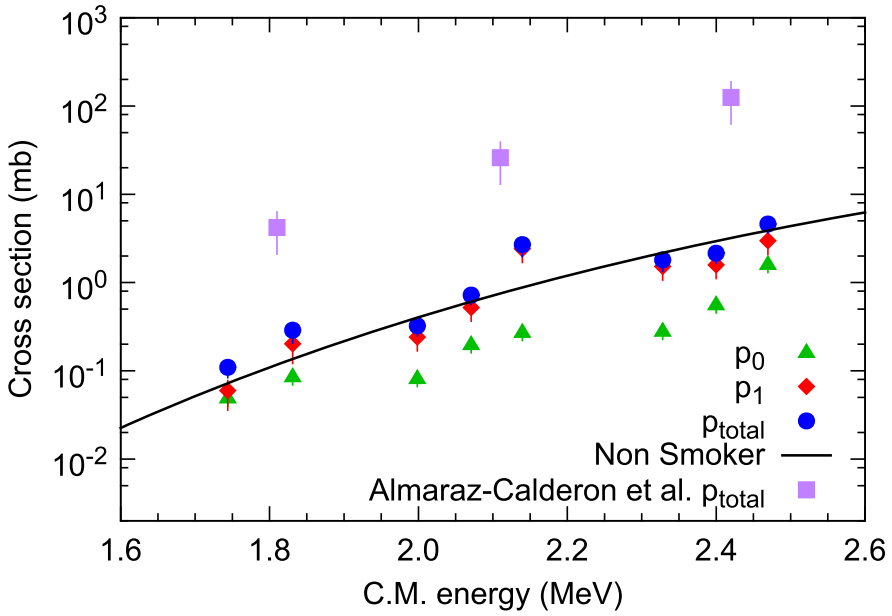

Fig. 3.5 Cross sections calculated by Howard *et al.* compared to the statistical model cross section calculations and the cross sections calculated by Almaraz-Calderon *et al.* [26].

Chapter 4

Experimental Setup and Procedure

Measurements of the ^{23}Na(α,p)^{26}Mg reaction were carried out using the TUDA (TRIUMF UK Detector Array) Scattering Chamber at the ISAC-I (Isotope Separator and Accelerator) facility at TRIUMF (TRI University Meson Facility), Canada. The experiment was carried out in three stages, with two slightly different experimental setups. The experimental setup for the first stage of data taking was improved upon based on analysis and so the setup was modified slightly for second two stages of data taking. This chapter will begin by discussing the ^{23}Na beam production and acceleration, and will go on to describe the experimental setups inside TUDA and the experimental methods used.

4.1 ^{23}Na Production and Acceleration at ISAC-I

The ISAC-I facility at TRIUMF is a Radioactive Isotope Beam (RIB) facility capable of the post acceleration of both stable and radioactive beams up to energies of 1.9 MeV/u, where u is one atomic mass unit. Stable beams such as ^{23}Na are produced with the Offline Ion Source (OLIS) [32]. Figure 4.1 shows the ISAC-I experimental hall including OLIS and the acceleration stations before the TUDA scattering chamber.

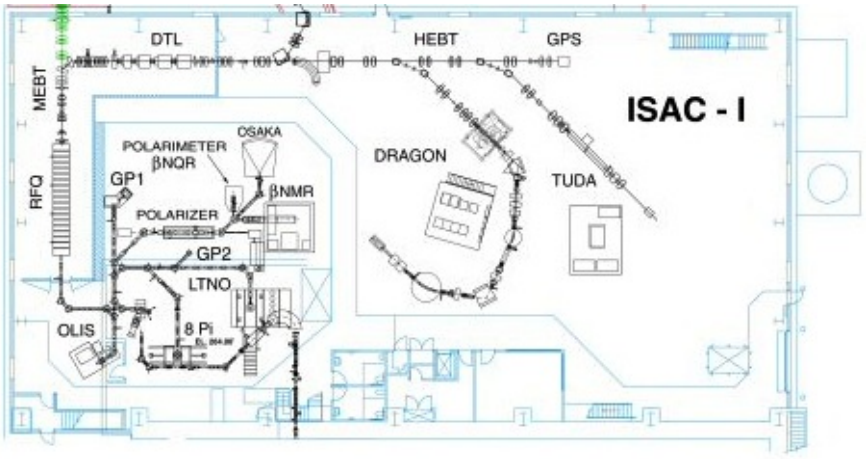

Fig. 4.1 OLIS and the ISAC-I hall at TRIUMF. Figure from Reference [33]. See text for details.

4.1.1 ^{23}Na Beam Production OLIS

The OLIS terminal consists of a surface ion source, a microwave ion source and a hybrid surface-arc discharge ion source. An electrostatic switch allows for any source to be selected without mechanical intervention [34]. For the first experimental setup, $23Na^{+}$ was produced in the surface ion source. For the second experimental setup the beam was produced by injecting ^{23}Na into the microwave ion source. The ^{23}Na was then extracted and accelerated in the low energy beam transport (LEBT) to the first stage of acceleration.

4.1.2 ^{23}Na Beam Acceleration and Tuning

The first stage of acceleration is the room temperature Radio Frequency Quadrupole (RFQ) which can accelerate particles with $3 \leq A/Q \leq 30$ from 2 keV/u to 150 keV/u [35], where A is the atomic mass number and Q is the charge of the particle. Before the beam enters the RFQ it is bunched to improve the beam quality and transmission. This is done using a three harmonics electrostatic buncher located in the LEBT which bunches at 11.78 MHz, the third subharmonic of the RFQ resonant frequency of 35.36 MHz. This gives a time structure to the beam leaving the RFQ characterised by a main bunch with two satellite bunches separated by 28.3 ns on either side. Transmission through the RFQ is 75% if the beam is pre-bunched in this way, if the

beam is not pre-bunched only 25% transmission is achieved [32]. After the RFQ the beam enters the medium energy beam transport (MEBT). Here an 11.74 MHz chopper is used to remove the two satellite peaks giving only the main bunches separated by 84.8 ns [35].

The next stage of acceleration is a Drift Tube Linac (DTL) which has an A/Q acceptance ratio of $2 \leq A/Q \leq 6$ [35]. A carbon stripping foil in the MEBT section upstream of the DTL is used to achieve this and has a stripping efficiency of between 30% and 50% [32]. For the ^{23}Na ions the charge state was increased from a 1^+ state to a 5^+ state. The beam is bunched at the foil using a 106.08 MHz MEBT buncher in order to reduce the longitudinal emittance from the foil and then again just upstream of the DTL using a 35 MHz spiral buncher. The DTL can accelerate ions from 150 keV/u to 1.9 MeV/u with a transmission of more than 85% [32].

Finally the beam enters the High Energy Beam Transport (HEBT) where two bunchers, one at 11.98 MHz and one at 35.36 MHz, are used to manipulate the longitudinal emittance from 4 ns to 1 ns in time or 0.4% to less than 0.1% in energy [32]. The beam then enters the TUDA scattering chamber.

4.2 The TUDA Scattering Facility

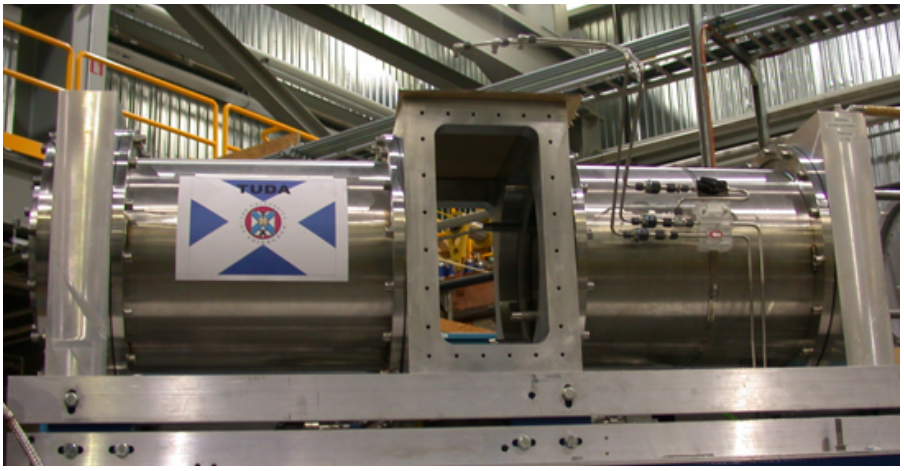

Fig. 4.2 Image of the TUDA Scattering chamber [36]. See text for additional details about the geometry.

The TRIUMF-UK Detector Array (TUDA) is a 1.5 m long scattering chamber which consists of two cylindrical ends attached either side of a central rectangular section as shown in Fig. 4.2. The chamber sits coaxial to the beam line in the ISAC-I hall and is designed to house arrays of charged particle detectors which are mounted on rails that run through the chamber. The central rectangular section houses target ladder apparatus for up to three target ladders which are operated using calibrated linear drives on the top of the chamber. Target ladder positions are illustrated in Figs. 4.3 and 4.4. Targets mounted on these target ladders can be either solid or gas. A gas handling system for gas cell targets feeds in through the top plate of the rectangular section to the gas cell target which was positioned on target ladder 1. Ports on the top of the chamber and on the downstream flange of the chamber allowed for electrical feedthroughs into the chamber for the detector electronics. Four vane monitors were used for the purpose of tuning the beam to the target position and anti-scatter collimators were used to prevent beam scattering into the detectors.

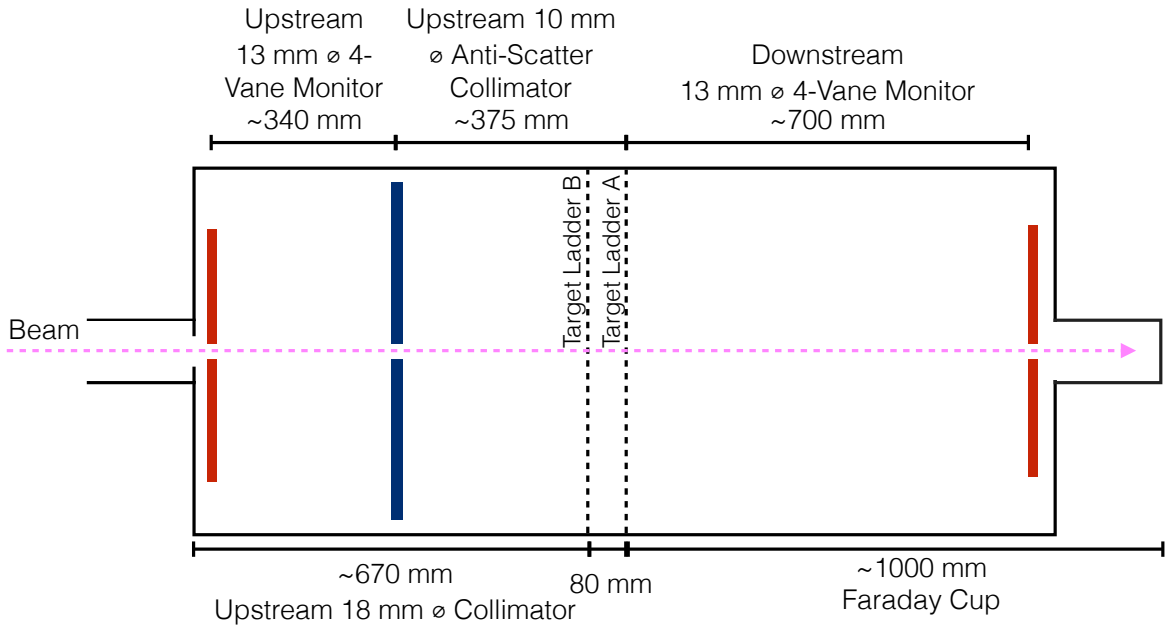

Fig. 4.3 Schematic of the diagnostic setup of TUDA for the first experimental setup. The symbol $\varnothing$ = diameter.

The beam was tuned to be no more than 3mm in diameter at the target position. In order to achieve this the beam was tuned at each energy. For the first experimental

run a 10 mm collimator was placed at the target position and the optical settings were manipulated to achieve >95% transmission through the chamber. This was then replaced by a 5 mm collimator and the same procedure repeated. Finally a 2 mm collimator was put into the target position and the beam tuned to >90% transmission through the aperture. For the second experimental run the beam was initially tuned through a blank space on the target ladder until transmission was >95%. It was then tuned in the same way through a 6 mm collimator and finally through a 3 mm collimator until transmission was ∼95 %.

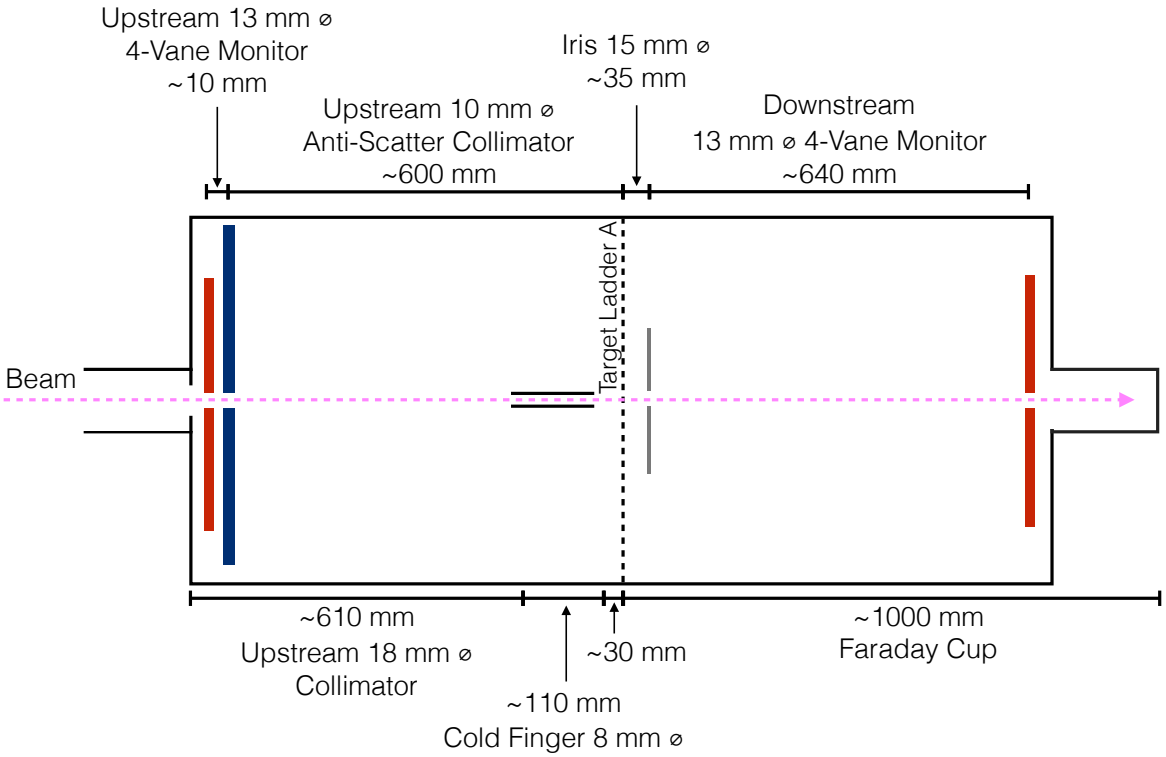

Fig. 4.4 Schematic of the diagnostic setup of TUDA for the second experimental setup.

The chamber runs at typical pressures of 1×10^{-6} mbar and utilises a roughing pump, a turbo pump and a cryogenic pump attached to the chamber below the rectangular central section. Firstly the roughing pump is used to reduce the pressure in the chamber to <330 mbar. The fragile nature of the gas cell target windows and foils in the chamber meant this had to be done at a rate of <0.5 Torr/s (<0.7 mbar/s). The valve to the roughing pump is then closed and the turbo pump is turned on.

Once the chamber reaches $\sim 1 \times 10^{-3}$ mbar the valve to the cryogenic pump can be opened. The chamber then reduces to $\sim 1 \times 10^{-6}$ mbar.

4.2.1 The Edinburgh Gas Cell Target

The Edinburgh gas cell target was used for this experiment. This is an aluminium gas cell target with gas inlets on either side for gas to flow in and out. A schematic of the gas cell target is shown in Fig. 4.5. The target length was 2 cm with a 1 cm diameter entrance window and a 4 cm diameter exit window. The entrance and exit windows were made of nickel, the entrance window was 2.5 μm thick and the exit window 6 μm thick. The beam was stopped in the exit window. At one energy a 4 μm titanium entrance window was used in order to replicate more closely the experimental setup of Almaraz-Calderon *et al.* [25]. The gas cell was filled with $\sim$110 Torr ($\sim$147 mbar) of ^{4}He.

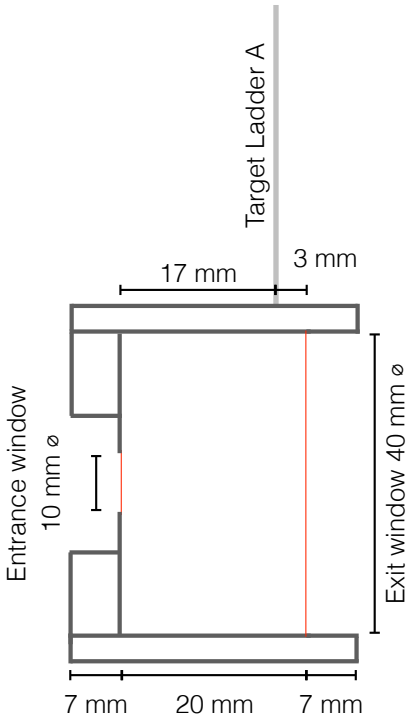

Fig. 4.5 Schematic of the Edinburgh gas cell target.

Gas was inserted into the target using a set of valves at a rate of $\sim$0.1 Torr/s ($\sim$0.13 mbar/s) and removed from the chamber by bypassing the gas lines into TUDA. Figure 4.6 shows the positions of the gas inlets and outlets on the gas cell. Leak

checking was performed on each gas cell prior to its use by inserting 110 Torr of ^{4}He into the cell and monitoring the pressure for a period of hours. A pressure change of no more than 2 mbar per hour is considered an acceptable cell. During the first experimental run the system of pipes used to insert gas into the cell was extensive and leak checking was time consuming. For the second experimental setup the gas line system was simplified to cut out all unnecessary pipe work and reduce the risk of a leak.

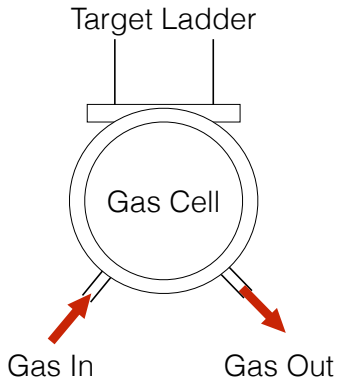

Fig. 4.6 Diagram of gas inlets and outlets on the Edinburgh gas cell.

During the first experimental run fusion evaporation of the beam with hydrocarbons built up on the entrance window caused a background of protons in the same energy region as reaction protons from ^{23}Na(α,p)^{26}Mg. This background was seen with both gas in the target and gas out of the target. A build up of hydrocarbons could be seen on the outer surface of the entrance window from the first experimental run, shown in the image in Fig. 4.7.

After the first experimental run the entrance window of the gas cell was tested at The University of Surrey Ion Beam Centre. Proton beams at energies of 1.74 MeV and 2.04 MeV were used to irradiate the entrance window material. The lower beam energy is more sensitive to surface carbon and the higher is more sensitive to back surface oxygen. The results showed a carbon oxide surface contamination on the upstream side of the foil and surface oxidation on the back side of the foil which is predominantly NiO and Al_2O_3.

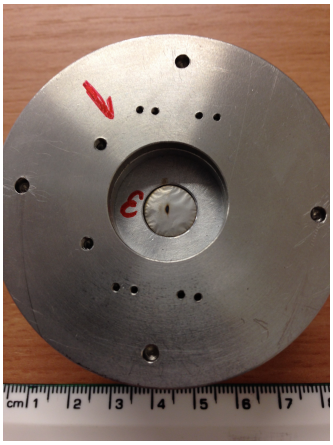

Fig. 4.7 Entrance window side of the gas cell target for the first experimental run. Beam induced hydrocarbon buildup can be seen as the small black spot on the entrance window.

In order to try and reduce the hydrocarbon buildup during the second and third experimental runs a cold finger was used. The cold finger is a liquid nitrogen cooled copper cone with a hollow copper tube for the beam to pass through. It is positioned upstream of the target as shown in Fig. 4.8. This provides a place for the hydrocarbons around the target to condense. The cone is cooled using a liquid nitrogen reservoir positioned on the side flange of TUDA's central rectangular section which was filled once the chamber reached $\sim 1 \times 10^{-5}$ mbar.

4.2.2 Semiconductor Detectors

During the experiment silicon semiconductor detectors were used for the detection of charged particles. The detectors used are P-N junction type detectors. One side of the detector is doped using an element that has an extra valence electron (N-type region) and so has an excess of electrons. The other side is doped with an element which has one fewer valence electron creating an excess of unfilled holes (P-type region) [37].

At the boundary between these two types, the P-N junction, there is a charge discontinuity and so migration of majority carriers occurs across the boundary. This creates fixed impurity sites, giving a net positive space charge on the N side and a net negative space charge on the P side of the junction, creating an electric field which

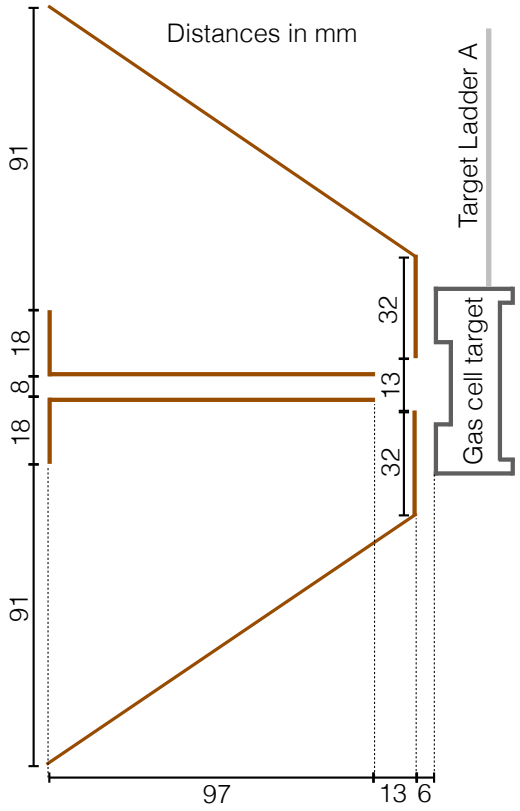

Fig. 4.8 A schematic of the cold finger position in the chamber. The cold finger is shown in brown.

prevents further migration. This region of charge imbalance is called the depletion region. Applying a reverse bias across the detector, with positive voltage applied to the p side of the junction compared to the n side, can extend the depletion region out further into each side of the detector. This reverse bias gives the detector better charge collection and reduces noise [37].

The detectors are biased to give as large a depletion region as possible, however the depletion region does not extend all the way out to the surface layer of the detector. This surface layer is referred to as the dead layer of the detector. Ionising radiation must pass through this dead layer before entering the 'active' region of the detector and so the energy loss of the particle in the dead layer must be accounted for in calibrations [37].

The two sides of the detector are connected by an external circuit. When an ionising particle passes through the semiconductor material electron hole pairs are created as the particle excites electrons into the conduction band. The movement of

these charges in the electric field induces a current in the external circuit which is the signal that is measured [37].

S2 Detector Array

The S2-type detector is a double sided silicon strip detector which has 48 annular strips on the front p-doped side of the detector and 16 radial strips on the back n-doped side of the detector. An image of a detector's front and back faces is shown in Fig. 4.9. The front annular strips are not complete rings. The percentage of the total ring that each front strip subtends varies between 82% for the outer ring and 100% for the inner-most ring. The front 48 strips have a strip width of 491 μm and a strip separation of 100 μm. The inner active diameter is 22 mm and the outer active diameter is 70 mm [38]. The active area of the detector is the area in which particles are detected.

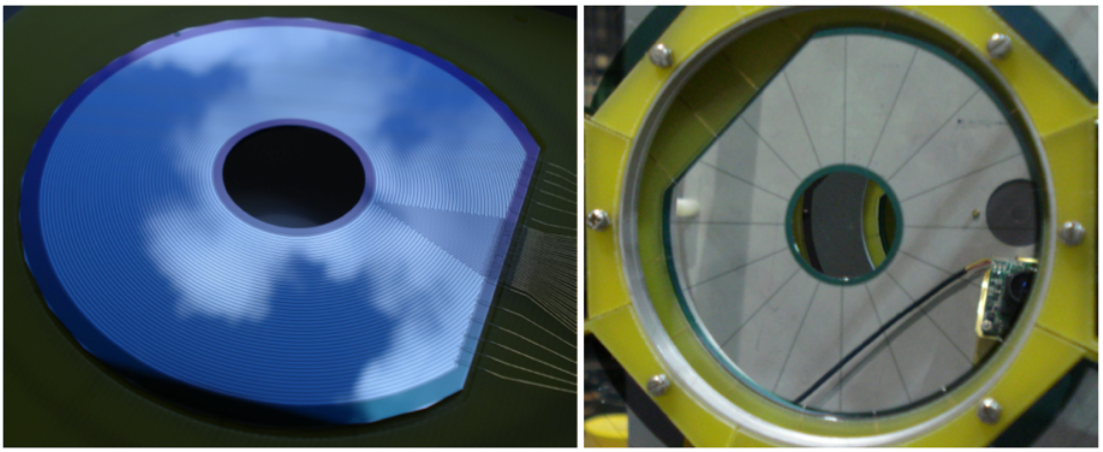

Fig. 4.9 The S2 detector front 48 annular strips (left) and back 16 radial strips (right). Figure taken from Reference [36].

For the first experimental setup four S2 detectors were used making up two telescopes. The first telescope comprised a 65 μm ΔE and a 508 μm E detector and the second telescope, positioned further downstream was made up of a 74μm ΔE and a 1051 μm E detector. The thicker E detector was placed further downstream as reaction kinematics meant that this was where the higher energy protons would be detected.

For the second experimental setup the telescope further downstream was removed. During the first experiment it was found that the downstream telescope did not provide a sufficient yield due to its small angular coverage. Therefore only one telescope was used for the second experimental setup which was made up of a 65 μmΔE detector and a 1051 μm E detector. The S2 detectors have a dead layer of 0.25 μm Al plus 0.5 μm Si [39]. The product codes and manufacturer's description of the S2 detectors can be found in Appendix A along with information on the angular coverage of each strip.

LEDA Detector Array

The Louvain-Edinburgh Detector Array (LEDA) is a single sided silicon strip detector array designed for nuclear physics measurements at Louvain-la-Neuve radioactive beam facility. They are Micron Semiconductor Ltd (MSL) type YY1 detectors which can be mounted onto a frame holding eight segments. Each segment has 16 radial strips which are 49 mm wide separated by 100 μm [40].

During the first experimental run the LEDA detector was used to measure backscattering of the beam from the entrance window. Four LEDA segments were used as shown in Fig. 4.10. During the second experimental run LEDA was used to measure backscattering of the beam from a gold foil placed 0.7 cm upstream of the entrance window to the gas cell. Seven LEDA segments were used in this case. The manufacturers detector specifications and angular coverage of each strip can be found in Appendix A.

Photodiodes

Two Hamamatsu S3590-06 PIN photodiodes with dead layers of $\sim$0.5 μm Al [39] were mounted on target ladder one for each experimental setup for beam energy measurements. During the first experimental run a piece of 2.5 μm Ni foil cut from the same piece of foil as the entrance window to the gas cell was mounted on a target ladder at target ladder two position. This allowed for beam energy measurements

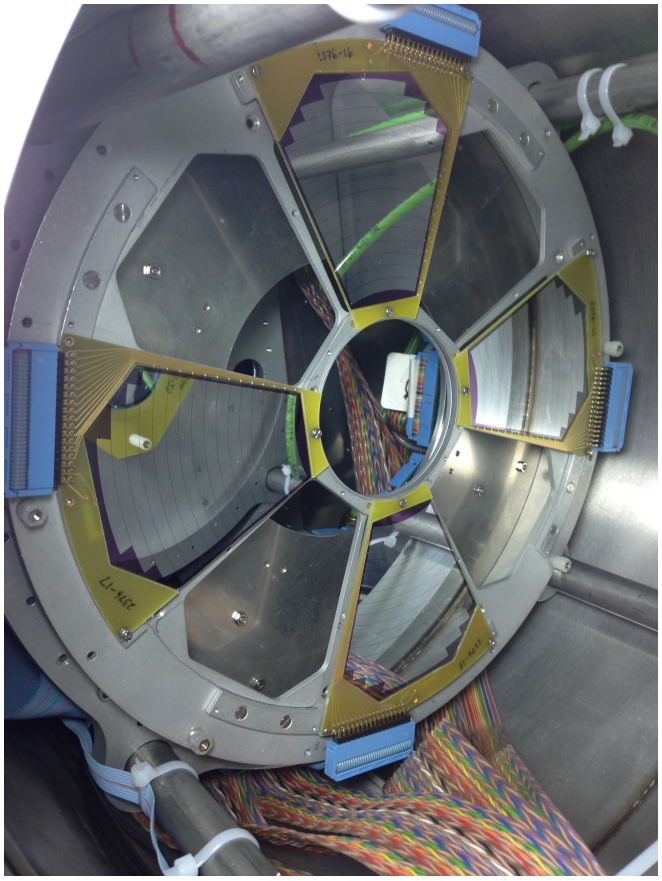

Fig. 4.10 The LEDA detector array in the first experimental setup. Each segment has 16 strips.

both with and without the entrance foil material. During the second experimental setup a 10 mm aperture was mounted in front of the photodiode so that half the surface of the photodiode could be covered with a 2.5 μm Ni foil. This technique was used as the cold cone in the second setup prevented the use of a second target ladder.

4.2.3 Detector Positions

A detector position diagram for setup one is shown in Fig. 4.11. The ΔE and E detectors were separated by 14mm for telescope 1, covering angles of $\theta_{\text{lab}} \sim 14.9°$ - 31.4° from the centre of the gas cell target. For telescope two the detectors were separated by 11 cm and the $\theta_{\text{lab}} \sim 2.8°$ - 8.9°.

For the second experimental setup several improvements were made. Firstly, a better tuning procedure was adopted. An iris was installed to protect the detectors

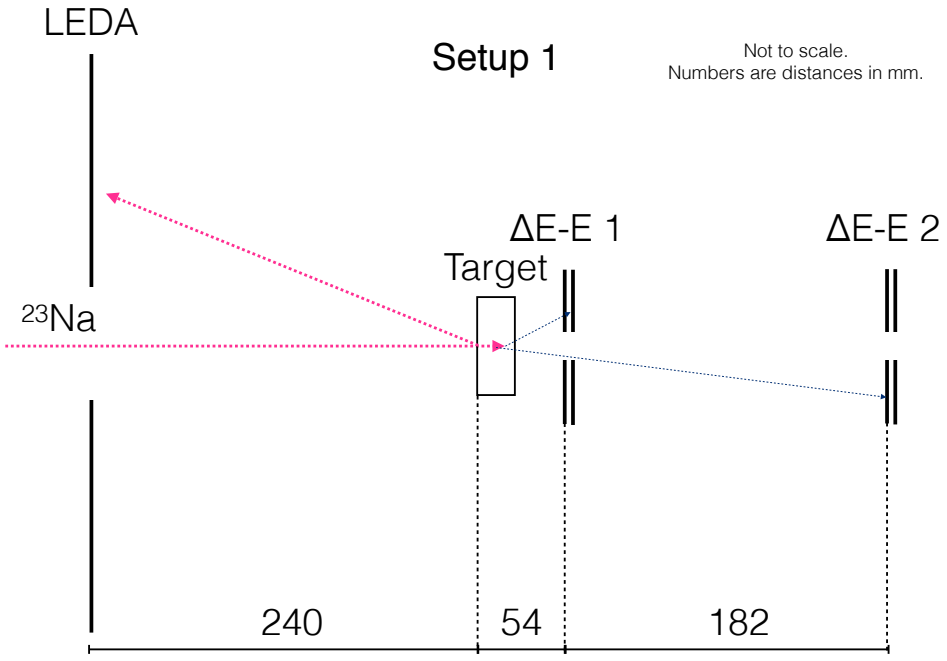

Fig. 4.11 Detector configuration for experimental setup 1.

during tuning which was mechanically controlled using a linear drive at the target ladder two position. This meant, unlike during the first experimental setup, the chamber didn't need to be opened before and after tuning to install detector shields and so the chamber was kept under vacuum conditions for most of the experiment.

Secondly, during the first experimental run it was found that due to the thickness of the Ni entrance window the backscattered beam energies meant a full yield could not be extracted above the energy threshold of the LEDA detector. This meant other methods had to be used to calculate a beam intensity. To extract a beam intensity more easily in the second experimental setup, backscattering of the beam from a 0.252 μm gold foil was measured in the LEDA array. The gold foil was attached to the gas cell target 7 mm upstream of the entrance window.

For the second experimental setup a single ΔE-E telescope covered angles of $\theta_{\text{lab}} \sim 10.2^\circ$ - 26.7° from the centre of the gas target. A detector configuration is shown in Fig. 4.12. The second downstream telescope was removed as it measured insufficient counts for ^{23}Na(α,p)^{26}Mg during the first experimental run. The thicker E S2 detector from the downstream telescope was used in the single S2 telescope

for the second setup as during the first experimental run protons were observed punching through the thinner upstream E detector.

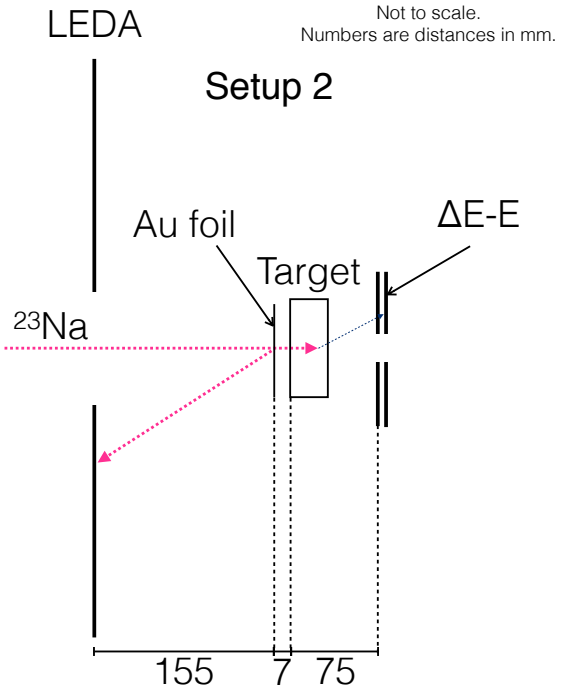

Fig. 4.12 Detector configuration for experimental setup 2.

4.3 Detector Electronics and Data Acquisition

4.3.1 Preamplifiers and Amplifiers

When an ionising particle passes through the detector the initial stage of signal processing for the induced current is an RAL 108 charge sensitive preamplifier [41]. The charge sensitive preamplifier produces an output voltage proportional to the total input charge from the detector which is proportional to the energy of the ionising particle. In order to minimise noise the preamplifiers are located as close to the detectors as possible inside TUDA, minimising the capacitance loading on the preamplifier with the shortest possible cables [37].

The vacuum conditions in the chamber mean that cooling can not occur via conduction and convection and so a coolant loop is used to cool the preamplifiers during the experiment. The preamplifiers are mounted onto copper cooling plates

and the coolant loop set to -10°C. The preamplifier temperature was monitored with a thermocouple and remained at 4±1°C throughout the experiment. The high voltage power supply for each detector and the pulser input as well as the power supply for each preamplifier are fed into the chamber through the back flange of TUDA.

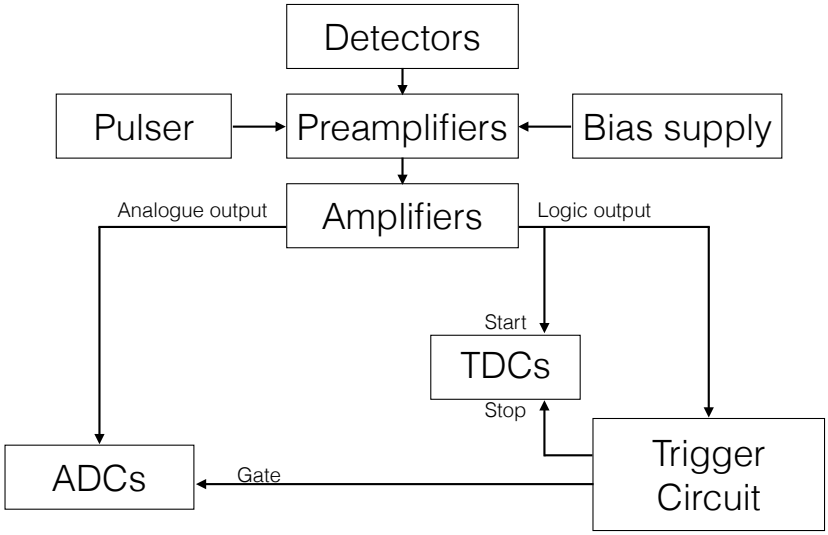

Fig. 4.13 Diagram shows the path of signals from the detectors, though amplifiers and into the trigger circuit.

Signals from the preamplifiers are fed via 32-way twisted pair cables through the back flange of TUDA into a module which inverts the signal and splits each input cable into two 8-way cables. These modules, along with the rest of the trigger circuit electronics are located in an air conditioned copper shack.

The 8-way cables are fed into the RAL 109 shaping amplifiers which produce two signals for each channel, one digital, one analogue. The digital trigger pulse is produced when the input signal is above a set discriminator threshold. This signal feeds into CAEN V1190A multi hit Time to Digital Converters (TDCs) and a trigger circuit. The analogue signal produced is read into SILENA 9418/6V Analogue to Digital Converter (ADC) modules which convert the analogue signal into a digital signal for processing by the computer. Figure 4.13 shows a diagram of the signal path from the detectors into the trigger circuit.

The discriminator threshold for each amplifier can be set using a front panel screwdriver adjust. The gain of each amplifier can be changed by using different resistor packs which attach to the motherboard. For the purpose of this the S2 detector amplifiers used 22 Ω resistors, giving 20 MeV full scale range. The full scale range of the LEDA detectors was ∼40 MeV.

4.3.2 Trigger Circuit

Figure 4.14 shows the trigger circuit. The discriminated logic output from the Amplifier feeds into logic shaped output modules. Each module takes 3 × 16 channels, if a signal is received in any detector channel by the logic shaped output module, a signal is sent into a set of Fan In/Fan Out (FI/FO) modules. The FI/FO modules are arranged such that there is a module for each of the ΔE-E S2 telescopes and the LEDA detectors. If a signal is received by the FI/FO module a signal is sent into a Quad Coincidence module with a gate set to 'OR'. The result is that if any strip in any detector registers a hit above the amplifier discriminator threshold, a shaped output from a quad coincidence module is sent to the next stage of the trigger circuit.

The shaped output from the quad coincidence module is sent to a second quad coincidence module, if this signal coincides with the signal from the delayed beam pre-buncher, a signal is sent to the Silena 9148 ADC controller (SAC). If the ADCs are not busy the SAC sends a signal to the ADCs to digitise the analogue signal from the amplifiers and record the data. This signal is also read out by a visual scaler as triggers presented to the DAQ and the CAEN V560 scaler module. If the SAC is not busy, and the ADCs accept the trigger, a signal is sent to a quad coincidence module to be put into coincidence with the delayed ADC trigger signal. If a coincidence is registered a signal is sent to the visual scaler as triggers accepted which is also fed into the scaler module for analysis. The triggers presented and triggers accepted by the DAQ can then be used to calculate the dead time of the ADCs in the analysis.

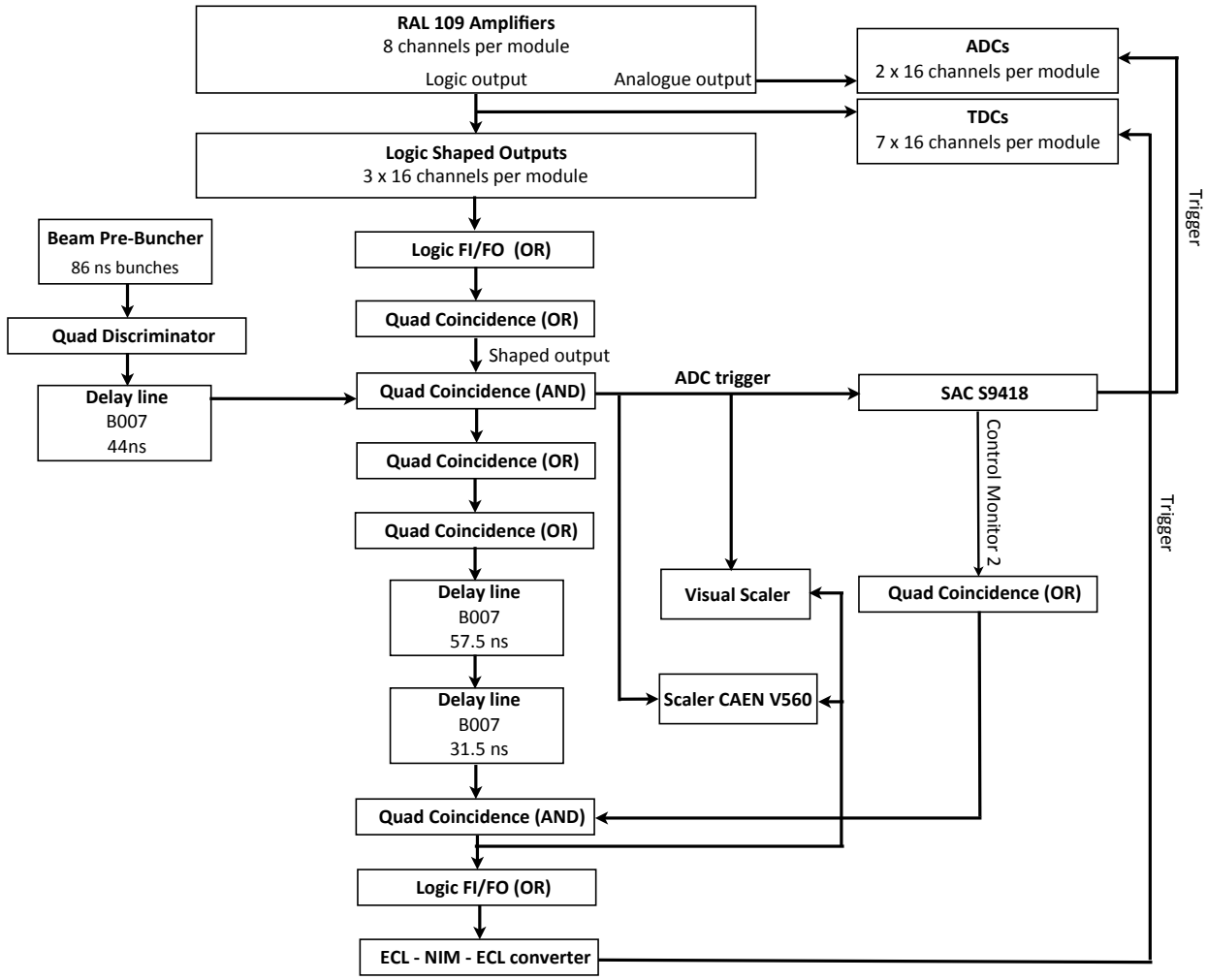

Fig. 4.14 The trigger circuit used to process signals from the detectors before they are recorded. See text for full details.

The timing information is calculated by the 128 channel TDCs. The clock for a given detector strip is started by the discriminated logic output signal from the amplifiers. They are then stopped by the ADC trigger signal from the coincidence between the TDC 'start' signal and the beam pre-buncher coincidence which is delayed to allow the ADCs to process data and the accepted Control Monitor 2 signal. For the purpose of this analysis the timing information was not used to identify particles.

The SILENA 9418/6V ADC modules, CAEN V1190A TDC modules, CAEN V560 scaler module and the SILENA 9148 SAC module make up the Virtual Machine

Environment (VME) modules which are configured by the MIDAS (Multi Instance Data Acquisition System) data acquisition and analysis software. The MIDAS software was used for both experimental control as well as online data analysis which is performed as data is taken and offline data analysis, performed on the saved data files. The scaler channels recorded were triggers presented to the SAC, triggers accepted by the SAC and a 1 kHz clock. The clock is used to calculate the time for each run and also to calculate scaler rates.

4.4 Experimental Procedure

The experiment was carried out over three sets of beam time using two different experimental setups. The experimental setup inside the chamber and the electronic configuration was set up over a week in the month before the beam time to allow time for problem solving should any arise. The target ladders and targets were aligned to the beam line and in the case of the second setup the cold cone was also aligned. The first set of data were taken over 7 days of beam time in August 2013, the second set of data were taken over 6 days of beam time in July 2014 and the third set of data were taken over 4 days of beam time in August 2014.

Before and after each experimental run the S2 and LEDA detectors were calibrated using a triple alpha source consisting of ^{239}Pu, ^{241}Am and ^{244}Cm and a Berkley Nucleonics Corporation (BNC) Model PB-5 pulse generator. The photodiode detectors were calibrated using the triple alpha source data taken before the experiment and the beam data taken during the experimental run.

A 5^+ beam of ^{23}Na was used for each of the experimental runs. For the first experimental run four beam energies were measured. These were chosen such that the energy range of the beam in the gas target overlaps slightly with adjacent energy measurements. During the planning stages of the experiment the beam energy expected at the centre of the gas target was calculated using the The Stopping Range and Energy Loss (SRIM) software [42] and DEDX energy loss code. DEDX

is an energy loss code developed by the Nuclear Structure Facility at Daresbury Laboratory based on the code SPAR [43].

For each of the experimental runs one energy at the centre of the target was chosen to be repeated to check the reproducibility of the cross section calculated. The second run focused on a lower energy measurement which resulted in an upper limit to the cross section being measured. The third experimental run focused on higher energy data. Table 4.1 shows the beam energies measured during each experimental run and the time each beam was incident on the gas filled target. Times were measured to the closest minute in the data.

The energy loss through a piece of 2.5 μm Ni foil cut from the same sheet of foil as the entrance window to the gas cell was measured at each beam energy. Before reaction data were taken the attenuated beam was incident directly onto a photodiode, the target ladder position was then changed so that the beam passed through the Ni foil before entering the photodiode. The beam energy loss through the gas cell target was calculated using the SRIM energy loss software [42].

Experimental Run	E_{Lab} (MeV/u)	Time (minutes)
1	1.18	2434
	1.21	1128
	1.25	466
	1.35	62
2	1.19	3090
	1.39	106
3	1.39	63
	1.43	92
	1.46	69
	1.49	66
	1.52	63
	1.55	58
	1.58	43
	1.61	53
	1.64	58
	1.67	39
	1.7	40
Ti Window	1.39	213

Table 4.1 Beam energies before the target entrance window and gold foil (when present). Times shown are the total time the beam was incident on the gas filled target.

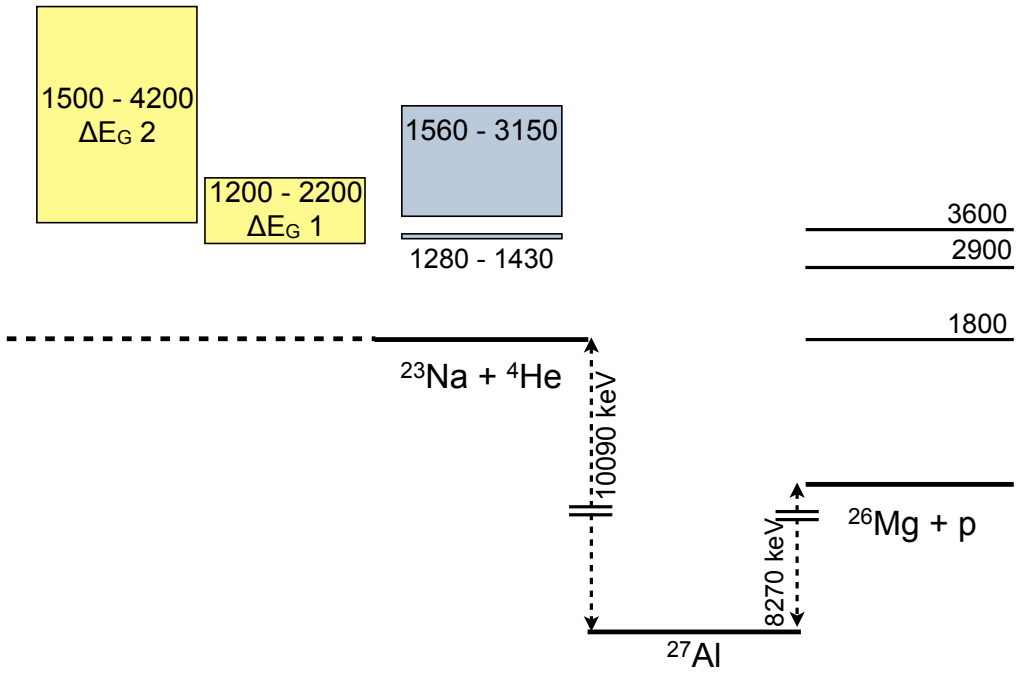

Fig. 4.15 The energy range covered during this thesis work is shown in grey, $\Delta E_G 1$ is the Gamow window for Ne/C convective shell burning in massive stars and $\Delta E_G 2$ shows the Gamow window for nucleosynthesis in Type 1a supernovae. The first three excited states in ^{26}Mg are also shown. Energies are in keV.

Figure 4.15 shows the energy range covered during the experiment. The first three excited states in ^{26}Mg are shown, although there are further excited states above those shown here, reactions were only observed to the ground state and first two excited states during this experiment.

Data were taken with gas in (gas-in data) the target and gas out (gas-out data) of the target so that a background subtraction could be made during analysis. The gas-in data is taken in ∼one hour runs before the cell was emptied and gas-out data were taken for approximately the same amount of time.

The beam intensity was measured and recorded at the beginning and end of each run (approximately every hour) using the beam dump Faraday cup located on the downstream flange of TUDA. The beam intensity was also monitored indirectly during the run using the triggers presented and accepted by the DAQ which are integrated every second and displayed. The total number of beam particles incident on the target was calculated using scattering data during analysis.

Chapter 5

Data Analysis

This chapter describes the data analysis techniques used to calculate cross sections from the data. The data were analysed from two different experimental setups as described in the previous chapter and analysis techniques varied slightly for each setup. Where possible the same analysis technique was used. Due to the data published by Almaraz-Calderon *et al.*, checks were made wherever possible to ensure the values calculated were correct since there was a large discrepancy between the results of the first set of data analysed in this work and the results presented in Reference [25].

5.1 Calibration of Silicon Detectors

Each strip of the S2 and LEDA silicon detectors were calibrated such that the energy in MeV for a given channel number could be calculated using Formula 5.1.

$$Energy = Constant \times Gain \times (Channel - Offset) \tag{5.1}$$

To calculate the parameters in this equation, firstly, a Berkeley Nucleonics Corporation (BNC) Model PB-5 pulse generator was used to perform the pulser walkthrough in order to calculate an offset for each channel. The pulses were increased

from an amplitude of 10000 to 90000 in increments of 10000 such that the pulse at 90000 corresponded to about 90% of the full scale range of the ADC. An example of an uncalibrated pulser spectrum for a front strip of an S2 is shown in Figure 5.1. A linear fit was performed on the peak position verses pulse number (1 to 9) to calculate the intercept. This intercept was the offset for each detector strip.

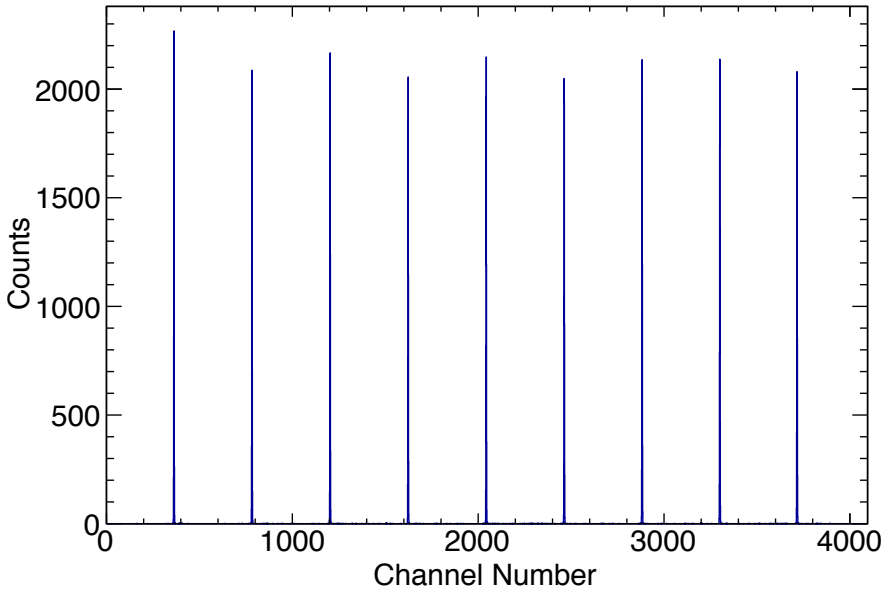

Fig. 5.1 Example of pulser spectrum used to calculate offsets.

A triple-alpha source, consisting of ^{239}Pu, ^{241}Am and ^{244}Cm with peak energies of 5.16, 5.49 and 5.80 MeV, was used to calculate the gain of each strip. An example of an uncalibrated alpha particle spectrum is shown in Fig. 5.2. The alpha particle data were sorted by applying the offsets calculated with the pulser data to each ADC channel. The energy loss of the alpha particle in the dead layer of the detector was calculated using the energy loss code DEDX and subtracted from the real energy of the alpha particles. A linear fit was then performed on the peak position verses the corrected energy of the alpha particles. The slope of this fit was equal to the gain.

During the second set of data taking the incorrect resistors were used in the amplifiers for the back strips of the S2 detectors giving a non linear scale in these ADC channels. In order to correct for this, a third order polynomial fit was made to the pulser data which created a linear scale before calculating a gain with the alpha particle spectra.

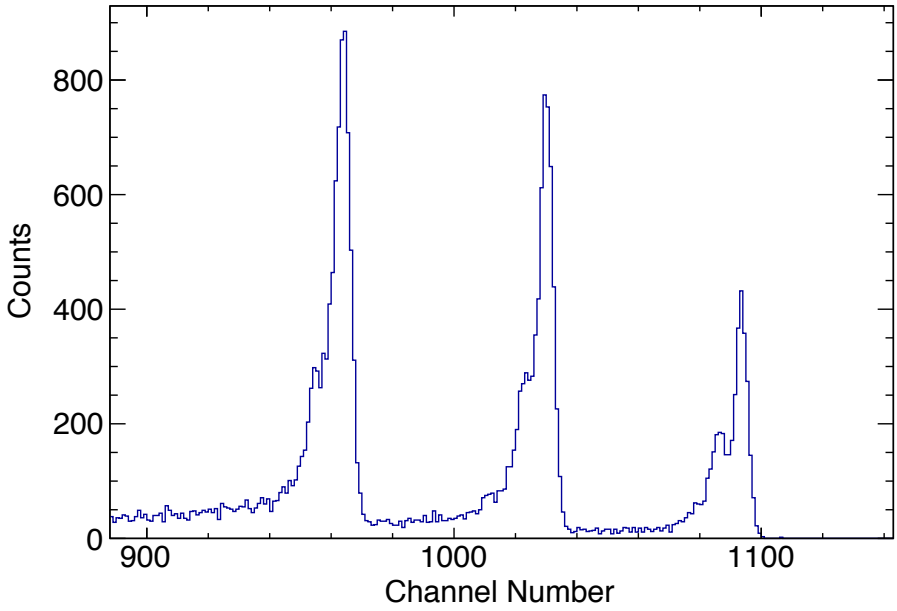

Fig. 5.2 An example of an alpha spectrum used to calculate the gains.

Once the offsets and gains had been calculated, the alpha source data were re-sorted applying these offsets and gains. A constant was then calculated using Equation 5.2 to calibrate the ADC scale to energy using the central channel of the ^{241}Am peak and accounting for energy loss in the dead layer of the detector as explained earlier.

$$Constant = \frac{E_{241Am}}{Channel} \tag{5.2}$$

To calibrate the photodiodes an attenuated ^{23}Na beam at each energy was impinged directly into the photodiodes. At some energies, these beam data showed some signs that the beam was clipping an object, most likely the cold finger, before it reached the photodiode. Overall, transmission through TUDA was found to be good at over 90% at each beam energy.

During the first experimental run, the photodiodes were calibrated using both beam and the triple alpha source data. A linear fit was performed on the peak position versus the energy of the beam and the triple alpha peak energies taking into account dead layer corrections. This was carried out for two cases: the first

being individual energies with the alpha particles, the second being all energies the photodiode was used for.

For the second and third experimental runs the photodiodes were calibrated in three ways to check the reproducibility of the calibration. Firstly, the beam was used to obtain a calibration using a linear fit of peak channel number vs peak energy. Secondly, both the beam and the alpha particles were used, using several beam points and the alpha particles. Thirdly, a calibration was performed using the individual beam energies and the triple alpha source data.

5.2 Beam Energy Calculation

For the first experimental run, the beam entered the gas cell through a 2.5 μm Ni foil. In order to calculate the energy of the beam after the entrance window, beam entered the photodiode through a piece of 2.5 μm Ni cut from the same sheet as the entrance window. The peak energy was calculated using each calibration of the photodiode and compared. In this case the calibration using the single beam point and the triple alpha source was used as the final energy calculation.

For the second and third experimental runs the beam entered the gas cell through a 251 μm gold foil and then the 2.5 μm Ni entrance window. In this case the peak position of the beam measured in the photodiode after passing through the 2.5 μm foil was calculated using each calibration method. This energy loss was also calculated using DEDX and a scaling factor (S.F.) was calculated using equation 5.3.

$$S.F. = \frac{DE_{Calibration}}{DE_{DEDX}} \tag{5.3}$$

The energy loss through the gold foil was calculated using DEDX followed by the energy loss through the 2.5 μm Ni foil. This energy loss through the Ni foil was then scaled with the scaling factor. Again the energy loss through the ^{4}He in the gas target was calculated using DEDX with an expected error of $\sim$20%. The

energy calculated from the calibration using beam points was used for the final beam energy. Using the beam to calibrate eliminated any effects of pulse height defect between alpha particles and ^{23}Na for these points. For the data point with the Ti window the same method was used. A comparison of the energy difference between the calibration techniques resulted in an error in the calibration of 0.4 MeV in the lab frame.

At energies where similar energies were calculated for the calibrations, the ^{23}Na(α,p)^{26}Mg proton energies and scattering data from Rutherford scattering of the ^{4}He target with the ^{23}Na beam were compared. In order to perform a comparison between experimental setups 1 and 2 a selection of strips covering the same angles was used. It was found that the point at 1.35 MeV/u and with the Ti foil corresponded to different beam energies than calculated by their original calibrations.

The cross section for ^{23}Na(α,p)^{26}Mg is larger at the start of the gas target where the beam energy is higher and so the average energy of the beam in the target must be weighted with cross section. The energy was scaled using Hauser Feshbach cross sections calculated by Thomas Rauscher with the code NON-SMOKER [21]. The effect was minimal at higher energies and only became apparent at lower energies. The centre of mass energies were calculated using Equation B.1 in Appendix B.

5.3 Yield Extraction

To extract a yield of protons from the ^{23}Na(α,p)^{26}Mg reaction, cuts were applied to reduce the background as much as possible. However, there were sources of background that could not be removed with cuts and so data were taken with gas in and out of the target so that a background subtraction could be performed. The same cuts were applied to both the gas-in and gas-out data so that the gas-out data could be scaled to the gas-in data and subtracted. The following section explains the method used to extract the yield.

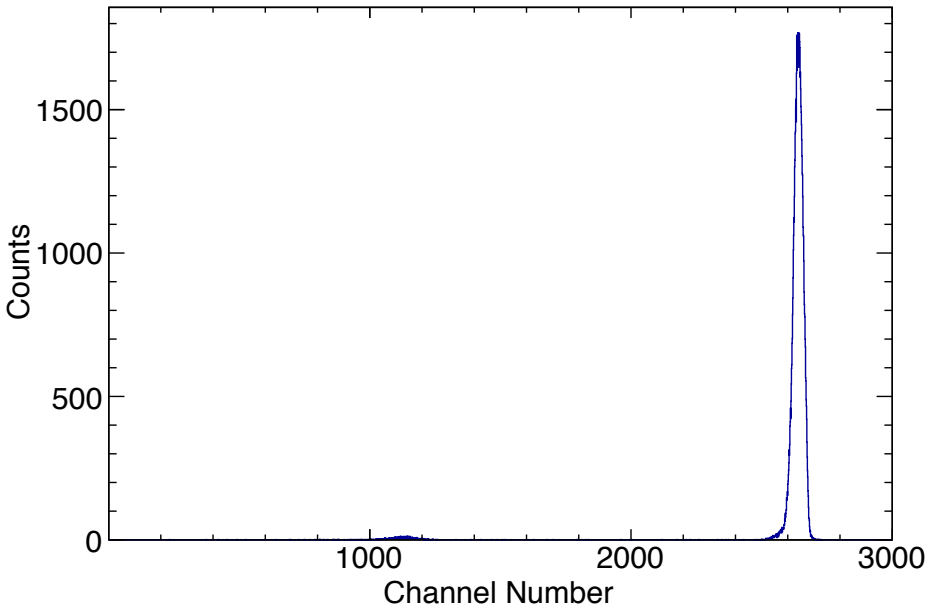

(a) Beam directly into PD.

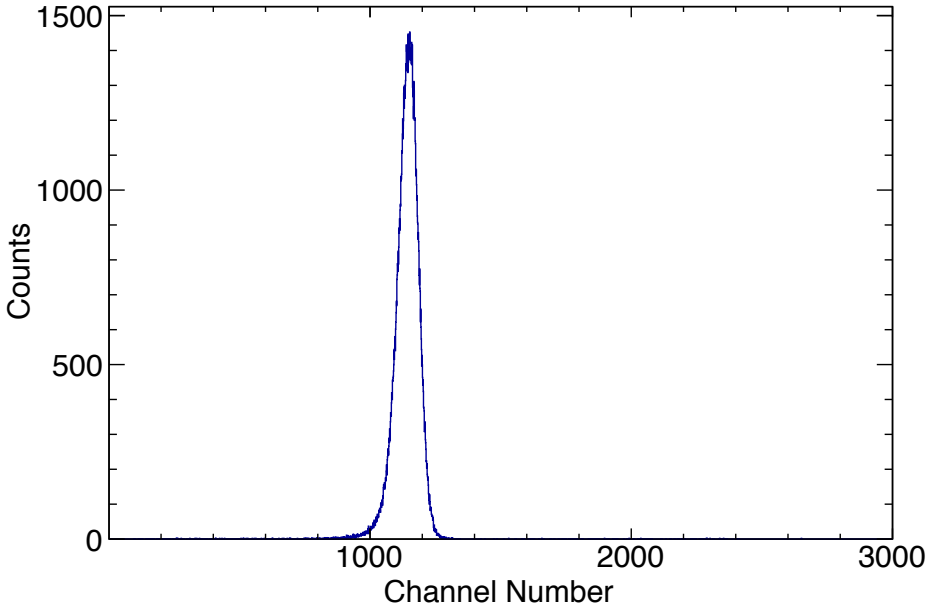

(b) Beam into PD through 2.5μm Ni foil.

Fig. 5.3 Uncalibrated photodiode (PD) spectra for beam energy $E_{c.m.} = 2.14$ MeV. Panel (a) shows the spectrum produced by the beam impinging directly into the PD, panel (b) shows the beam entering the PD through a 2.5 μm Ni foil.

5.3.1 Monte Carlo Simulation

A Monte Carlo simulation was used to simulate the kinematics of protons from the reactions ^{23}Na(α,p) in the gas target region and ^{23}Na(p,p) with protons on the outer surface of the entrance window. The code was written by Professor Alex Murphy and modified for this experimental configuration. It modelled the gas cell target, the gold foil (if present), and the S2 ΔE-E telescopes for each experimental setup.

The initial beam energy is inputted into the code and a random distance into the gas target for the reaction is selected. In the case of ^{23}Na(p,p) reactions with protons from water on the entrance window, the outer, upstream side of the entrance window was fixed as the location of the reaction. The code then calculates the energy loss to the point of the reaction, taking into account straggling of the beam. The reaction kinematics were then calculated and the projectile energy loss, through the exit foil material and dead layers of the detectors, was calculated and energy and angle were outputted. All energy losses were calculated with the energy loss code SRIM [42].

5.3.2 Sources of Background

There are several sources of background in the data from alpha particles and protons. The main source of alpha particle background comes from ^{23}Na(α,α) Rutherford scattering of the beam within the gas target. These alpha particles deposit energy in the detector from below the threshold energy to $\sim$9 MeV at the highest beam energy. This is not energetic enough to punch through the first detector and so they can easily be cut out by applying a condition that both the ΔE and the E detector must register a hit.

Secondly, alpha particles from ^{23}Na(p,α) reactions with protons from water contamination on the entrance window of the gas cell target were detected. This reaction has a Q-value of 2.38 MeV. These alpha particles were at much higher energies than those scattered from the gas target and do punch though the ΔE detector before being stopped in the E detector. They were easily removed from the data with a particle identification cut as discussed later.

Background from protons is dominated by ^{23}Na(p,p) scattering of protons from water contamination on the entrance window. These lie lower in energy than the protons from reactions to the ground state in ^{26}Mg, ^{23}Na(α,p_0), however they cover the same energy range as protons from reactions to the first excited state in ^{26}Mg, ^{23}Na(α,p_1). These background protons were seen in both gas-in and gas-out data and can therefore be removed using a background subtraction as described later in this section. The secondary source of background data were protons from fusion evaporation of the beam with carbon and oxygen on the entrance window.

Figure 5.4a shows a plot of energy vs strip for the reaction protons detected, compared to an energy vs strip plot produced from the Monte Carlo simulation of proton data in Fig. 5.4b. In Fig. 5.4a protons from fusion evaporation reactions of the beam with carbon and oxygen on the entrance window can be seen.

The energy expected for each of these sources of background was calculated and compared to data. The fusion evaporation calculations were carried out by Barry Davids using LISE++ [44]. The ^{23}Na(p,α) calculations were carried out using kin2b, a kinematics code written by Dr. Thomas Davinson [45], and the other calculations were carried out using kin2b and using the Monte Carlo simulation of the experimental setup.

5.3.3 Sort Code

Figure 5.5 shows the structure of the sort code used. Numbers in circles represent when histograms were incremented. The sort code was originally written by Thomas Davinson and modified throughout the analysis.

The scaler data which includes triggers presented to the DAQ, triggers accepted by the DAQ and a 1 KHz clock were read in and the rate of triggers presented and triggers accepted in Hertz were calculated. These rates were then plotted onto a one dimensional (1D) histogram and used to calculate the detector live time as described in section 5.11.

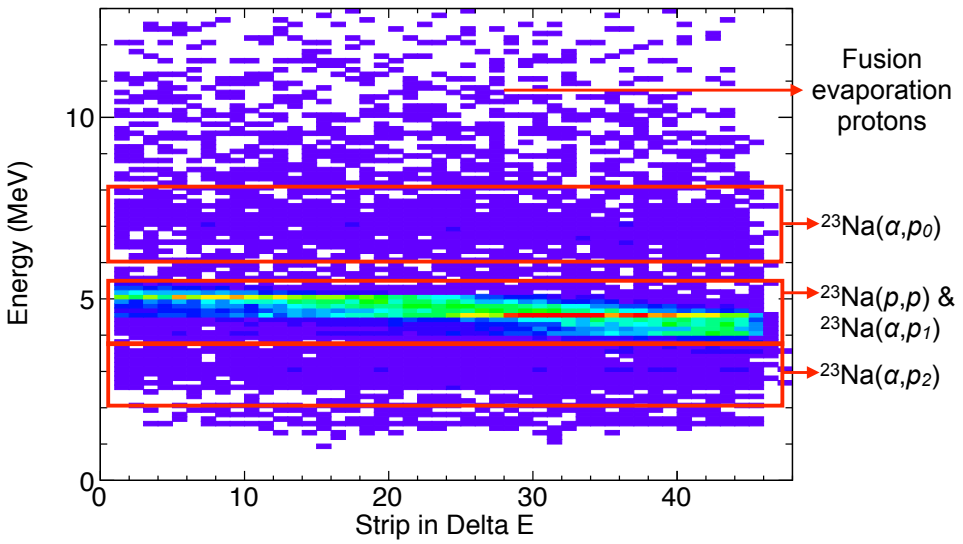

(a) Data

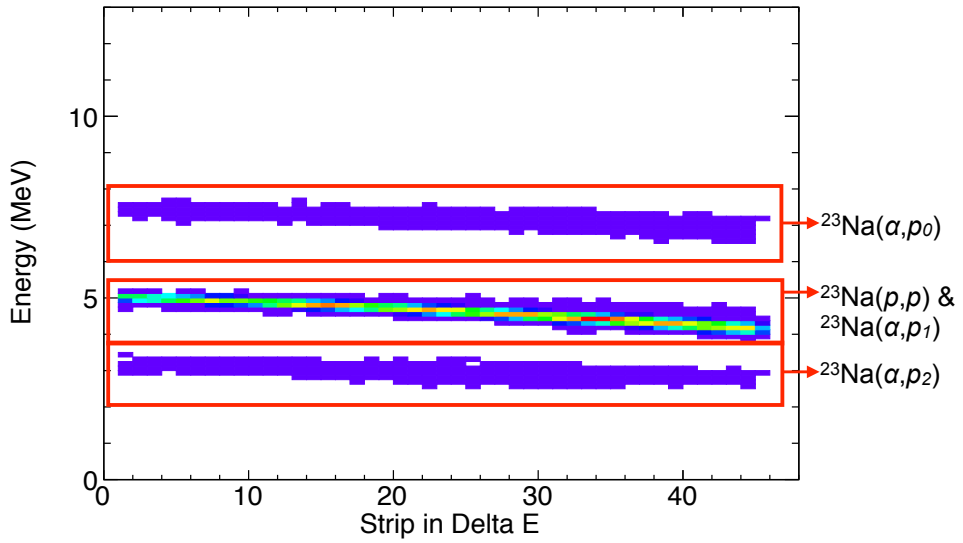

(b) Monte Carlo simulation

Fig. 5.4 Total energy vs strip proton spectra at $E_{c.m.} = 2.55$ MeV. Data from the experiment with gas in the target are shown in panel (a) and Monte Carlo simulation output is shown in panel (b). The different proton sources are labelled.

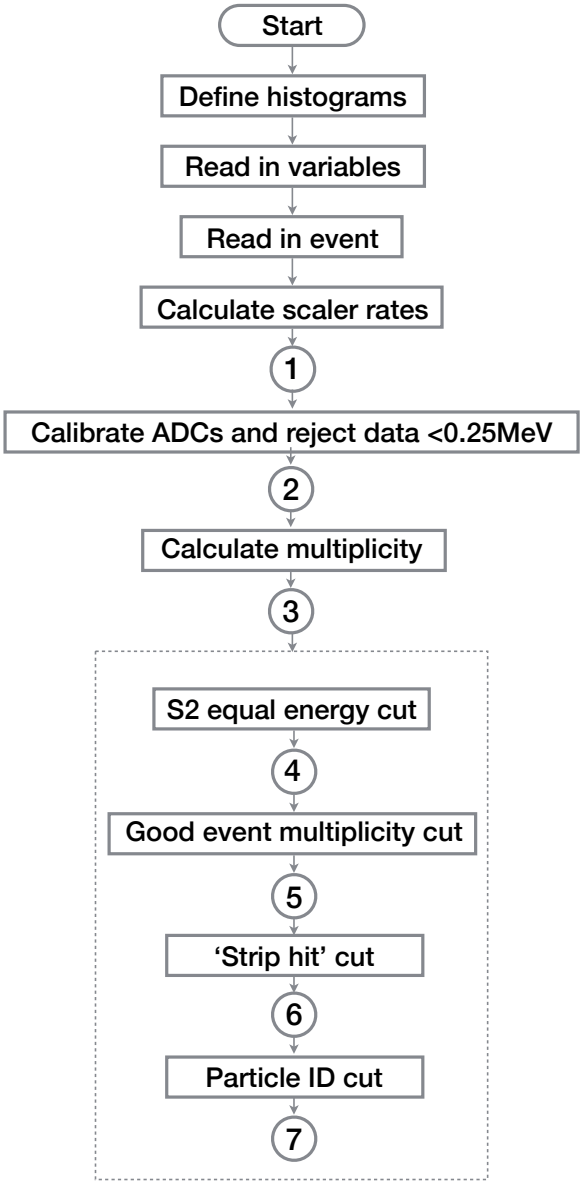

Fig. 5.5 Block diagram showing the structure of the sort code used to apply cuts to the data.

The ADC data were read in and calibrated and data less than 0.25 MeV were rejected. After this, 1D energy histograms were incremented (shown at point two shown in Fig. 5.5) for each of the S2 and LEDA detector strips. The LEDA energy spectra were used to calculate beam intensity as described in section 5.7. The multiplicity is equal to the number of strips that register a hit greater than 0.25 MeV. This was expected to show a peak at a multiplicity of two because of the double sided nature of the S2 detectors. 1D multiplicity histograms were incremented to check that the multiplicity peaked at two.

The sort code then focused on the S2 detectors. The front-back equal energy cut stated that for each S2 there must be a hit in a front strip of the detector and a hit in a back strip of the detector. As well as this, the energy deposited in the front strip and back strip must be equal to within a window of ±250 keV. This removed particles hitting the inter strip region of the detector and noise in the front or back strips of the detector. The strip ordering was then checked using the kinematic locus in a plot of energy vs strip for each detector. If the strips were out of order due to cabling the ordering was corrected and the data were resorted.

There was then a good event multiplicity cut for each ΔE-E telescope. This means there must be a hit in each S2 in the telescope which satisfies the previous selection rules. This cut removes alpha particles from ^{23}Na(α,α) scattering which are stopped in the ΔE detector.

Strip Hit Cuts

At point five in Fig. 5.5, histograms were incremented for the front strip hit patterns and the back strip hit patterns between the two S2 detectors in each ΔE-E telescope. The hit patterns were calculated as the difference in the back spoke hit ($\Delta\phi$) and the difference in the front annular strip hit (ΔStrip) between the ΔE and E detector in the telescope. These differences were calculated with the equations:

$$\Delta\phi = Back\ Spoke\ \Delta E - Back\ Spoke\ E + 200, \tag{5.4}$$

$$\Delta Strip = Front\ Strip\ \Delta E - Front\ Strip\ E + 2000. \tag{5.5}$$

A particle that enters the ΔE detector at a certain radial angle ϕ was expected to register a hit at the same ϕ in the E detector. An example of a $\Delta\phi$ distribution is shown in Figure 5.6. A peak in the $\Delta\phi$ plot was expected at 200 and this was the case for all energies. The number 200 in Eqn. 5.4 is added to shift the peak up the

spectrum to prevent it from appearing at 0. A $\Delta\phi$ cut was applied to the data such that $199 \leq \Delta\phi \leq 201$.

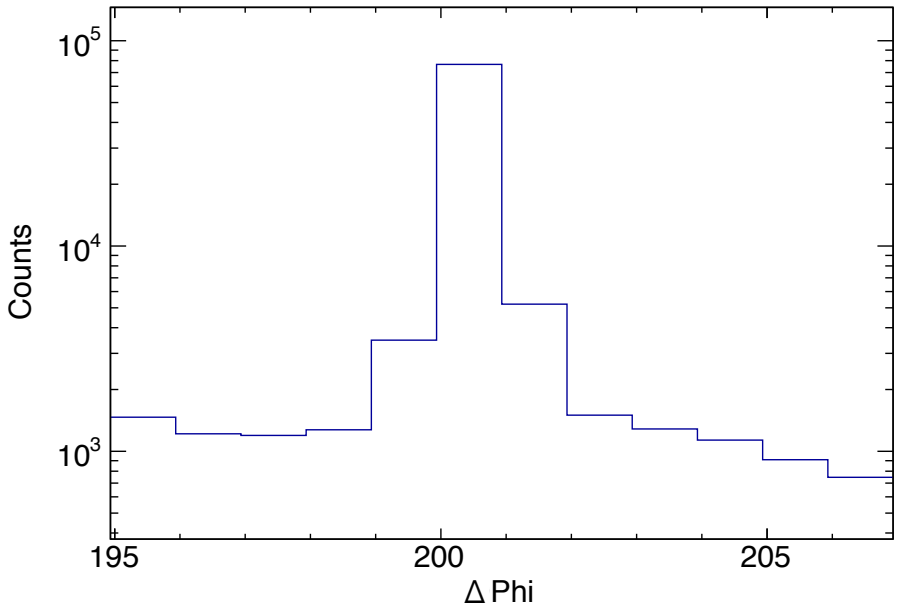

Fig. 5.6 $\Delta\phi$ distribution for $E_{c.m.} = 1.88$ MeV.

For ΔStrip, the hit pattern was dependent on how far apart the ΔE and E detectors were. S2 detector strips are numbered from 0 at the inner radius to 47 at the outer radius. Particles were expected to hit a lower numbered strip in the ΔE detector then, travel radially outwards towards the E detector, hitting a higher numbered strip. The peak should therefore be below channel number 2000 in the histogram. The number 2000 is used in Eqn. 5.5 to shift the peak up the spectrum to prevent it appearing below zero.

Figure 5.7 shows an example of a ΔStrip distribution for the second experimental setup. Here the ΔE and E detector were closer together and so the distribution was peaked at a higher channel number than for the second experimental setup. A ΔStrip cut was applied to the data such that $\Delta\text{Strip} \leq 2001$.

These cuts were checked and the data sorted without the cuts to ensure that important events were not being discarded from the data. It was found that no important events were being discarded from the data.

During the first experimental run the S2 detectors in the ΔE-E 1 (Upstream) telescope were separated by 1.4 cm. This large separation resulted in a line of sight

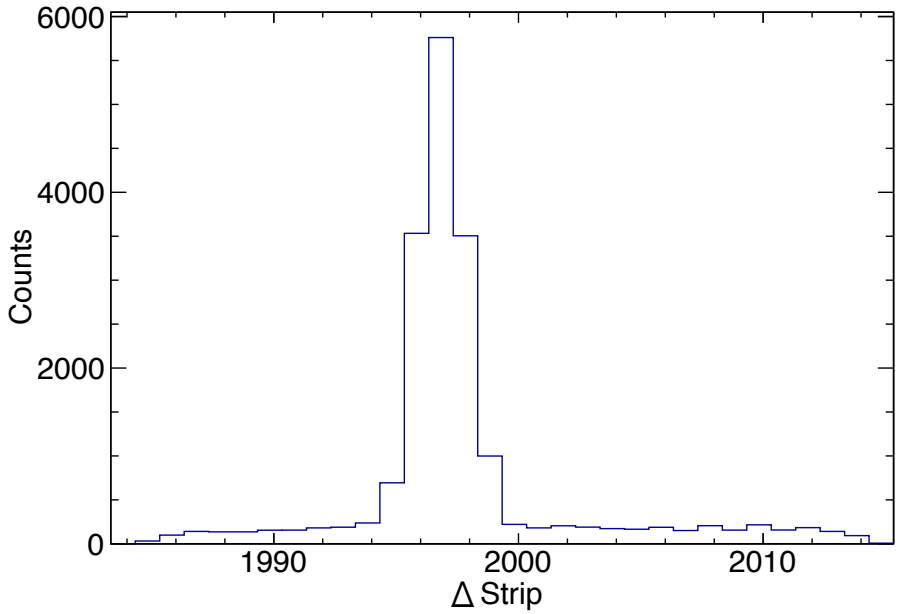

Fig. 5.7 ΔStrip distribution for $E_{c.m.}$ = 2.33 MeV.

for particles scattered from the target to hit the inner strips of the E detector without first passing through the ΔE detector. Random coincidences were therefore observed in the telescope and a strip hit cut was implemented to remove these random particles. Any hits in the first 6 strips of the upstream E detector were discounted.

Particle Identification Cuts

The particle identification cut employed the empirical range-energy relationship [46] formula:

$$R = aE^b \tag{5.6}$$

where R is the range of the particle in the absorber, a is a constant depending on the type of particle, E is the incident particle energy and b is a constant equal to 1.73 for Z = 1 and 2 ions [47]. The particle energy can be described by the formula

$$TM^{(b-1)}Z^2 = (E + \Delta E)^b - (E)^b \tag{5.7}$$

where T is the thickness of the ΔE detector, M is the atomic mass of the ion and Z is the atomic number of the ion [39]. In the sort code $(E + \Delta E)^{1.73} - (E)^{1.73}$ was calculated and because this function is proportional to Z^2, as shown in Eqn. 5.7, different values for alpha particles and protons are obtained. A 1D gate was applied in the sort code to remove background alpha particles. An example of this particle identification plot is shown in Fig. 5.8.

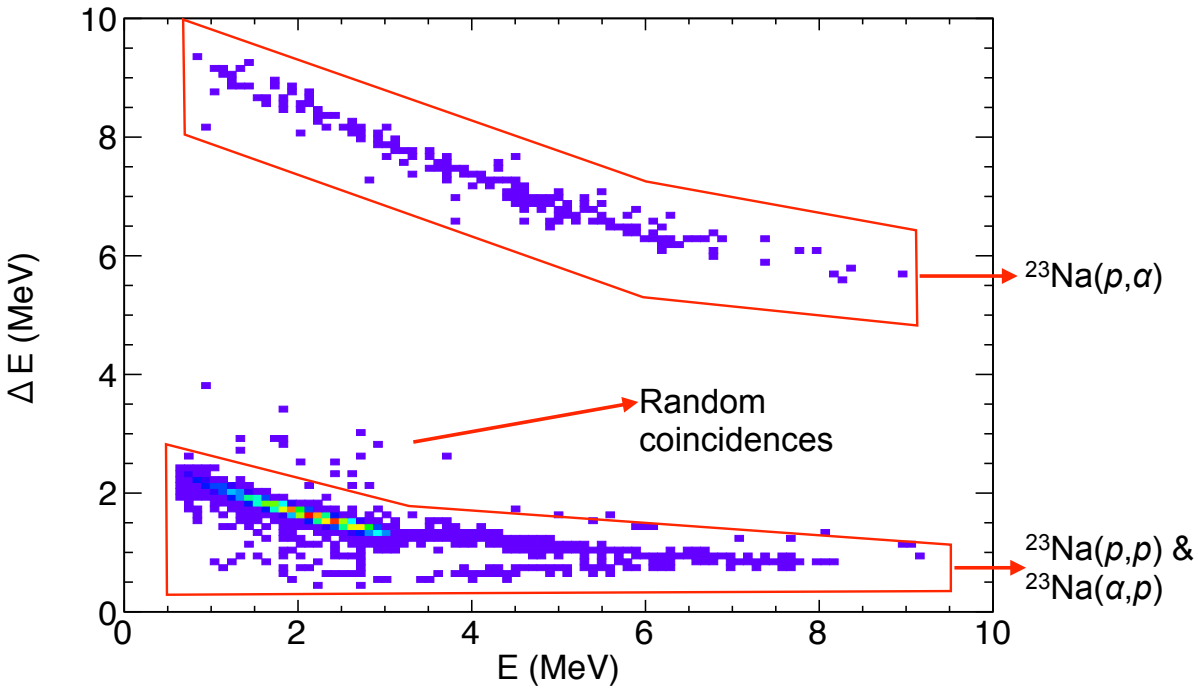

Fig. 5.8 Energy in ΔE detector vs energy in E detector at E_{cm} = 1.99 MeV with gas in the target. Outlined are the different particle types.

After each of these cuts had been applied, the total energy was calculated for each particle. This is the energy deposited in the ΔE detector plus the energy deposited in the E detector. The same cuts were applied to both gas-in and gas-out data so that a background subtraction could be performed.

5.3.4 Background Subtraction

^{23}Na(α,p_0)

The background subtraction was performed on the 1D total energy plot, which is the energy in the ΔE detector plus the energy in the E detector. Two separate methods were used to check the reproducibility of the result. Firstly the background protons from fusion evaporation, which are at energies higher than the background protons from ^{23}Na(p,p), were fitted with a single Gaussian in the gas-out data as shown in Fig. 5.9. The fit parameters of this Gaussian were then exported and the same Gaussian was drawn onto the gas-in data to model the background. The amplitude of the fit was varied to fit the background using higher energy fusion evaporation protons. This is shown in Fig. 5.10.

In order to ensure that different background fit methods resulted in a similar yield the background data were also fitted with a double Gaussian. This Gaussian included the background peak of protons produced from ^{23}Na(p,p) reaction with protons from water contamination on the entrance window of the gas cell. Using different background fit methods did not significantly change the final yield, producing changes in yield of no more than a third of the error in the yield.

For consistency, a single Gaussian fitted to the protons produced by fusion evaporation was used as the background at each energy. The proton peak from ^{23}Na(α,p_0) in the gas-in data was then fitted with a Gaussian, an example of which is shown in Fig. 5.11, and the area under this curve was integrated. The same integration limits were used to integrate the background fit onto the gas-in data, and this was subtracted from the yield of particles from the fit of the ^{23}Na(α,p_0) peak to calculate a yield.

Errors from this method come from the statistical error in the number of counts. In order to check that there is not a larger error than this arising from the scaling of the height of the background fit, the height of the background fit on the gas-in data was adjusted slightly in both positive and negative directions. The effect of this was within a third of the statistical error. As well as this the limits of integration for the

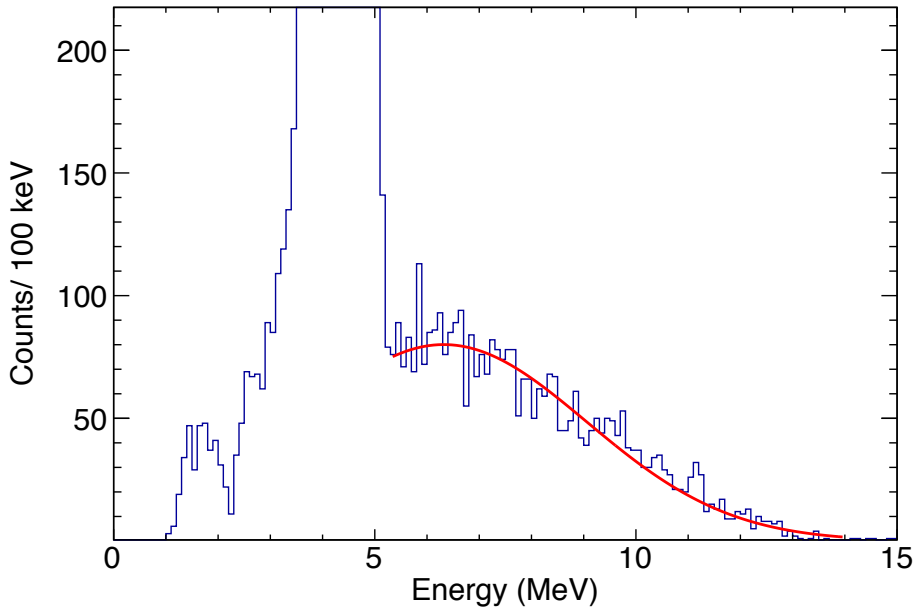

Fig. 5.9 Total energy plot for E_{cm} = 2.42 MeV with no gas in the target. A single gaussian is fitted to the background.

proton peak from ^{23}Na(α,p)^{26}Mg were adjusted slightly to the left and right, this also produced small differences in the yield that were within a third of the statistical error.

The second method used to extract a yield was direct scaling and subtraction. The gas-in and gas-out data were overlaid on the same plot and the gas out data scaled using the higher energy protons from fusion evaporation. An example of this is shown in Fig. 5.12 where the gas out data has been scaled to the gas in data. The gas out data were then subtracted from the gas in data and the ^{23}Na(α,p_0)^{26}Mg proton peak integrated. Again the calculated error in this method was statistical. However to check that there was not a larger error from the scaling method used, again, the height of the gas-out background data was adjusted slightly in positive and negative directions and subtracted. These differences were again within a third of the statistical error. As a check the scaling was also calculated using total beam intensity and the result was found to be the same.

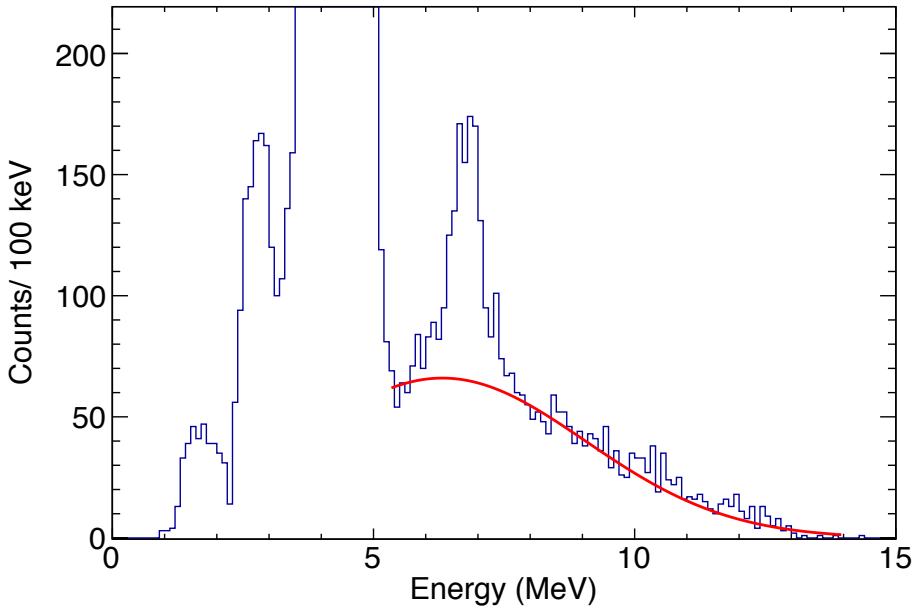

Fig. 5.10 Total energy plots for E_{cm} = 2.42 MeV with gas in the target (blue). The single gaussian (red) from the background data is fitted to the background.

^{23}Na(α,p_1) and ^{23}Na(α,p_2)

In order to extract protons from ^{23}Na(α,p_1) and ^{23}Na(α,p_2) the background fitting method could not be used as these protons are covered by a background peak from proton scattered from water on the entrance window. In this case the method of overlaying the gas-in and gas-out data and scaling as shown in Fig. 5.12 was used. Some examples of the subtracted data compared to Monte Carlo simulation are shown in Figs 5.13, 5.14 and 5.15. It should be noted that the Monte Carlo calculates energies but does not take into account cross section and so the ratio of counts in each peak has been modified to fit the data.

For the lower energy runs it was not possible to extract protons from reactions to the first excited state in ^{26}Mg (p_1 protons) or protons from reactions to the second excited state in ^{26}Mg (p_2 protons) as the runs were much longer and the amount of water on the window did not remain constant. This meant that the background scaling did not remove all of the background protons produced by the beam scattering protons from water on the entrance window. At higher energies the Monte Carlo shows that reactions to the third excited state in ^{26}Mg (p_3 protons) should be seen

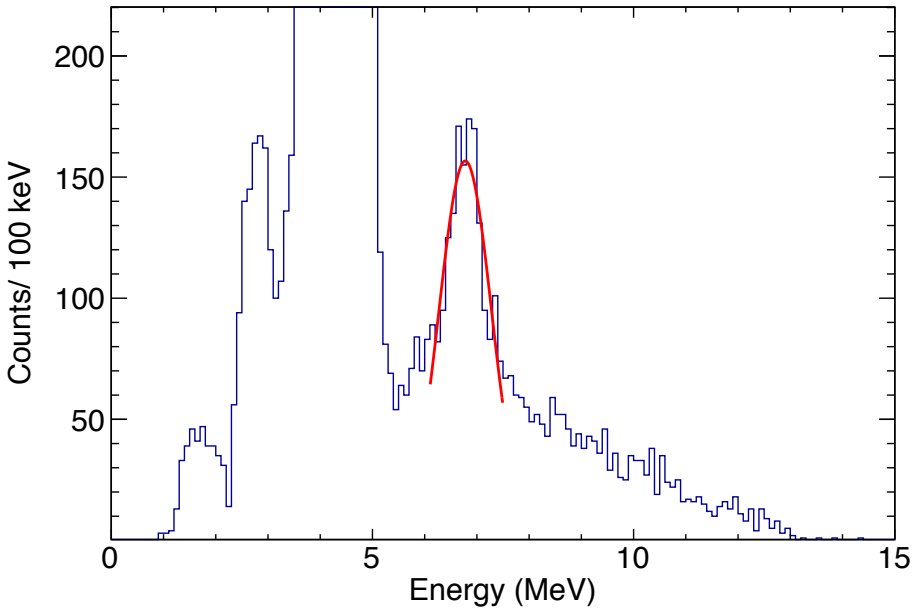

Fig. 5.11 Total energy plots for E_{cm} = 2.42 MeV with gas in the target (blue). The single gaussian (red) is fitted to the ^{23}Na(α,p_0) protons.

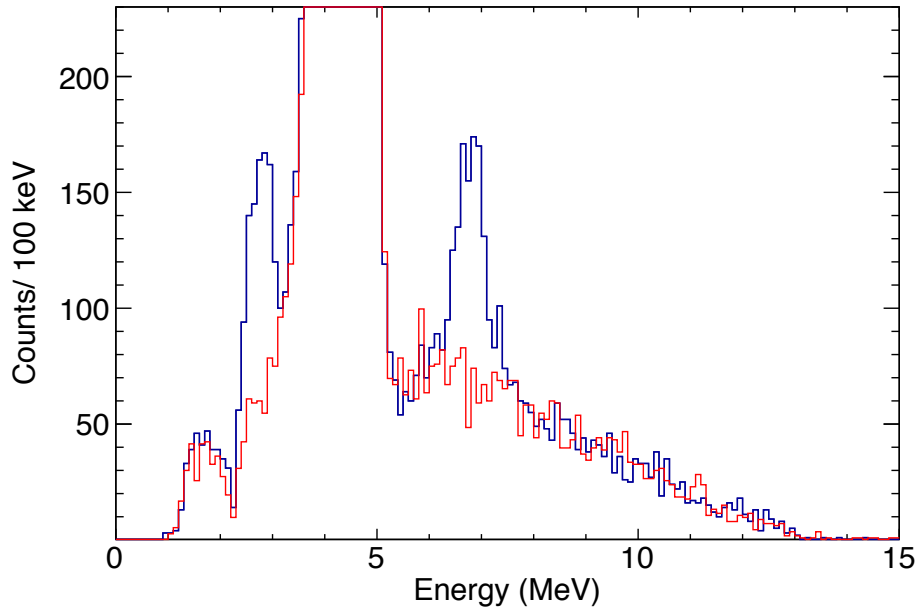

Fig. 5.12 Total energy plot for E_{cm} = 2.42 MeV. The gas-out data (red) have been scaled to the gas-in data (blue).

in the data as shown in Fig. 5.15. These protons are not seen in the data because the detector thresholds are very slightly higher than in the simulation.

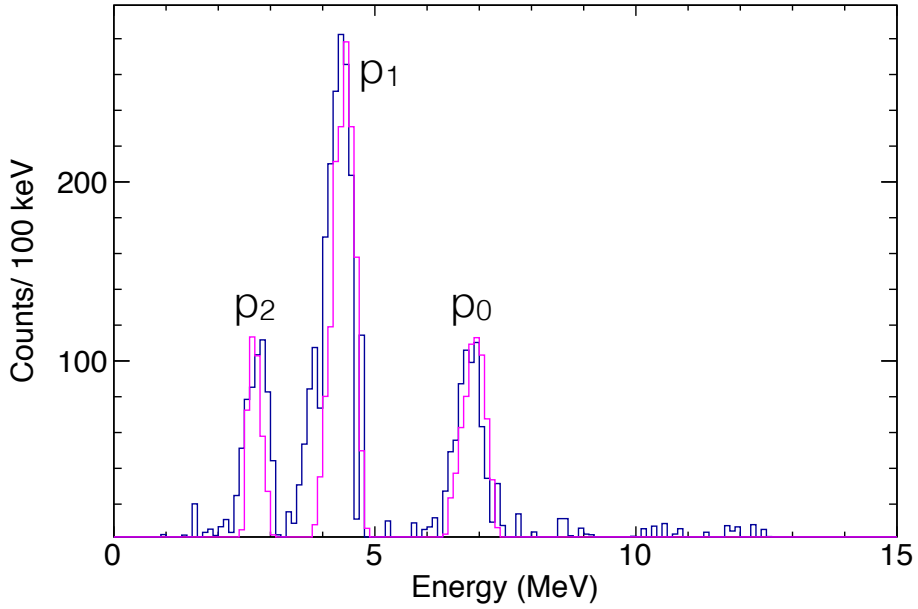

Fig. 5.13 Total energy plot for E_{cm} = 2.42 MeV. The background subtracted data are shown in blue, Monte Carlo simulation is shown in pink. Proton peaks from the ground (p_0), first excited (p_1) and second excited (p_2) states in ^{26}Mg are labelled.

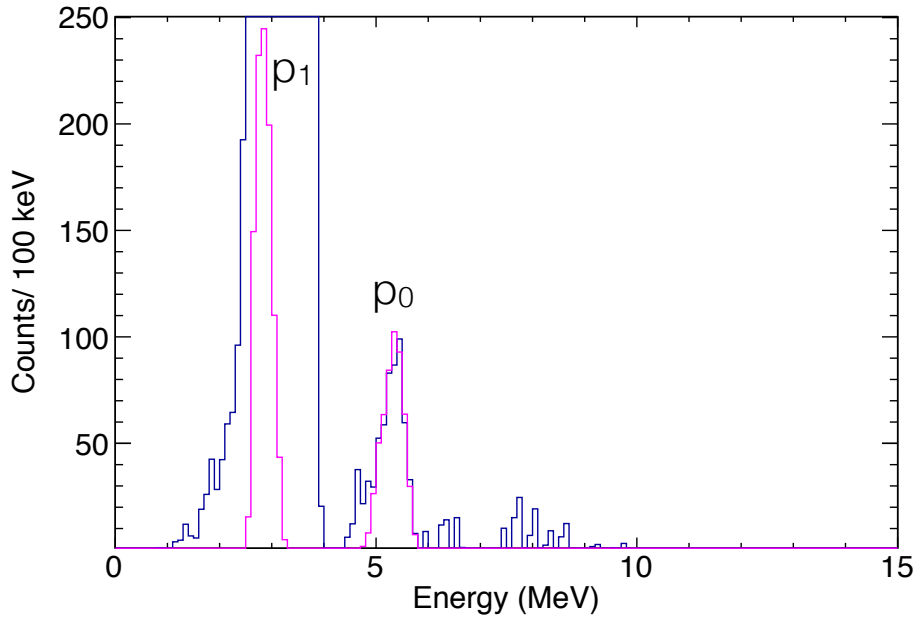

Fig. 5.14 Total energy plot for E_{cm} = 1.74 MeV. The background subtracted data are shown in blue, Monte Carlo simulation is shown in pink. Proton peaks from the ground (p_0) state in ^{26}Mg are labeled for both simulation and data, however the first excited (p_1) state in ^{26}Mg could not be resolved from the background subtraction in the data and is shown only for the Monte Carlo simulation.

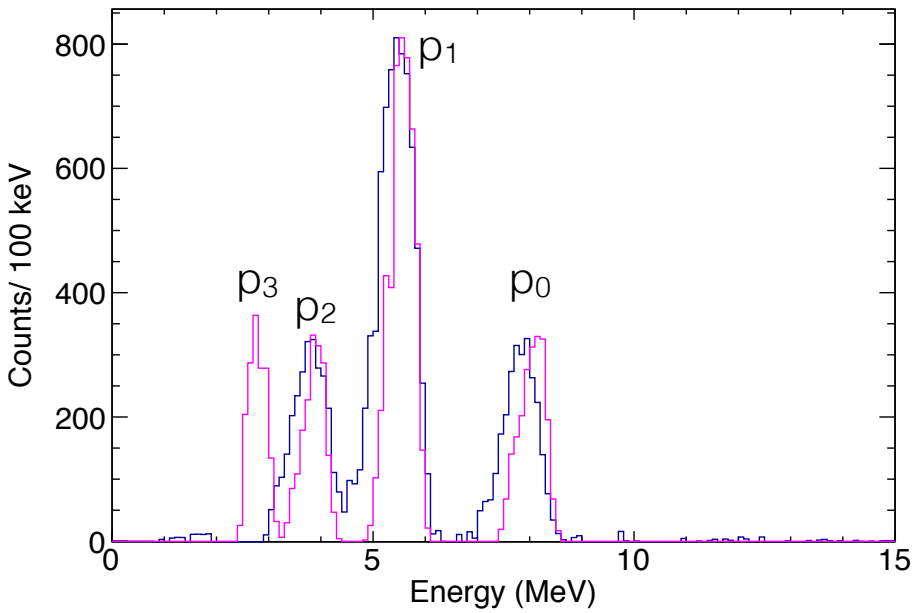

Fig. 5.15 Total energy plot for E_{cm} = 3.03 MeV. The background subtracted data are shown in blue, Monte Carlo simulation are shown in pink. Proton peaks from the ground (p_0), first excited (p_1) and second excited (p_2) states in ^{26}Mg are labelled for both data and simulation. Protons from reactions to the third excited state in ^{26}Mg (p_3) are not seen in the data.

5.4 Target Nuclei Calculation

The number of target atoms per centimetre squared was calculated using Equation 5.8 and Equation 5.9 [2]. In Equation 5.8 N is the number density of target nuclei in units of atoms per cubic centimetre, v is the number of atoms per molecule, P is the pressure of the gas target in Torr, T is the temperature of the target in Kelvin and the Loschmidt constant $L = 2.68677 \times 10^{19}$ cm^{-3}. In Equation 5.9 N_t is the number of target nuclei in units of target nuclei per squared centimetre, and d is the thickness of the gas cell target in centimetres, in this case 2 cm.

$$N = vL\frac{P}{760\ Torr}\frac{273\ K}{T} \tag{5.8}$$

$$N_t = N \times d \tag{5.9}$$

At 1.35 MeV/u initial beam energy the gas cell target pressure was 100 Torr, giving a target areal density of 6.59×10^{18} cm^{-2}. For all other beam energies the

target pressure was 110 Torr giving a target areal density of 7.25×10^{18} cm^{-2}. The temperature was taken as 293 K which was the approximate temperature of the experimental hall but an error of ± 5 K was assumed on this value as the temperature would vary from day to night. An error also comes from the fact that the pressure did not remain completely constant and could decrease by $\sim$1 Torr per hour. As short runs were used with gas being in the target for no more than 2 hours, an error of $\pm$ 2 Torr is assumed. Combining the error in temperature and the error in pressure leads to an error of 2.6% at 100 Torr and 2.5% at 110 Torr.

5.5 Solid Angle Calculations

The solid angle of each S2 detector strip was needed to calculate a total cross section. The solid angle of the annular strips of the S2 detectors was calculated using equation 5.10 which was found by integrating over the area of the ring in the detector from 0 to 2π in ϕ. Here θ_1 and θ_2 are the inner and outer centre of mass angles of the detector strip. The rings of the S2 detectors are incomplete in ϕ and so the solid angle calculated was multiplied by the fraction of each strip that actively detects particles. The angular coverage in ϕ of each detector strip can be found in Appendix A. Calculations are carried out in the centre of mass reference frame, with lab to centre of mass angle conversions calculated using Equation B.2.

$$\Sigma = 2\pi(cos\theta_1 - cos\theta_2) \times Active\,Area \tag{5.10}$$

5.6 Efficiency Calculations

The detection efficiency was calculated using Equation 5.11 where ε_{Tot} is the total efficiency and Ω is the solid angle, in the centre of mass frame, of the DE detector from the centre of the target taking into account dead strips. $\varepsilon_{Telescope}$ is the fraction of protons that would hit the E detector after hitting the DE detector taking into account dead strips in each detector. This fraction was calculated using a Monte Carlo

simulation modelling the geometry of the detectors. During the second experimental run the arm of the S2 shield was blocking part of the detector some of the data taken. This was accounted for by calculating the amount of active area of the detector that the arm blocked and subtracting it from the total active area of the detector.

$$\varepsilon_{Tot} = \frac{\Omega}{4\pi} \times \varepsilon_{Telescope} \times live\,time \tag{5.11}$$

The centrality of the beam was checked using alpha particles scattered by the beam in the gas target into the DE S2 detector. The total number of alpha particles was integrated for each back spoke of the DE detector. It was found that the beam was approximately 1 mm off the centre of the beam axis due to the rails that the detectors were held on dipping at the centre of the chamber. The rails on which the detectors are mounted are supported by the upstream flange and the downstream flange and are not supported in the centre of the chamber. The effect of the 1 mm offset on the solid angle coverage of the detectors was found to be negligable compared to the large error which results from the 2 cm target length.

The dominant error in the efficiency, and in the cross section came from the solid angle calculation because of the length of the gas cell target and the proximity of the ΔE-E telescope to it. The error was calculated assuming a 20 mm long gas cell with an error in the position of the detectors relative to the gas cell of ± 2 mm. The solid angle coverage of the detectors was calculated for a reaction at the beginning and end of the target including the error in the length and this was taken as the error on the solid angle.

The efficiency was also calculated with the Monte Carlo simulation to confirm the method. The Monte Carlo calculated the number of particles which would register a 'good hit' in the detectors as a fraction of the total number of reactions in the simulation. Live time was calculated as the ratio of triggers presented to the DAQ divided by triggers accepted by the DAQ. These data were read in as scaler data.

5.7 Beam Intensity Calculations

Experimental Run 1

Due to the fact that there was not a gold foil present to measure backscattered beam during the first experimental setup, the beam intensity was calculated using the Faraday Cup reading at the beginning of each run and the backscattered ^{23}Na beam particles from the Ni entrance window detected in LEDA. The beam intensity in particles per second (pps) was calculated using Equation 5.12 where N_b is the number of beam particles per second, I_{FC} is the electric current reading on the Faraday Cup and Q_b is the charge state of the beam. The beam was in a charge state of 5^+ and so a reading of 1 enA on the Faraday Cup corresponds to 1.25×10^9 pps.

$$\frac{N_b}{t} = \frac{I_{FC}}{Q_b} \tag{5.12}$$

The data were sorted for the first ten minutes of a run at each energy and the backscattered beam from the gas cell entrance window was integrated in each individual strip of LEDA. The counts per minute were taken to correspond to the beam intensity recorded on the Faraday Cup just before the run. To check that the beam intensity did not change significantly during these ten minutes the triggers presented and accepted were checked to be constant. The data for the total run time was then sorted and the total backscattered beam into each strip of LEDA was integrated. The average beam current was calculated by taking the ratio of the counts per minute from the total run to the counts per minute from the first ten minutes and multiplying by the beam current on FC4 at the beginning of the run.

The Faraday Cup reading is taken from FC4 which was located just upstream of TUDA. The beam transmission through TUDA was therefore taken into account in the beam intensity calculation. The error in this method was dominated by the reading on FC4. This was estimated to be 0.2 nA. The total beam on target was calculated by multiplying the average beam intensity in particles per second by the

time in seconds at each energy. The total time each energy was run for is calculated using the 1 kHz clock scaler data.

Rutherford scattering of the ^{23}Na beam with the ^{4}He target was used as a check to ensure the beam intensity calculated was correct. To do this a simulation was written which divided the gas cell target into fifty 0.5 mm steps. This method of dividing the gas cell target was used because of the large change in angular coverage of each strip. Beam energy losses through the target were calculated using SRIM energy loss tables. At each step the Rutherford cross section for each annular strip in the downstream ΔE S2 detector was calculated by integrating Equation B.4 over θ for each strip. The yield of scattered alpha particles expected in each strip was then calculated using the equation:

$$Yield = \sigma N_B N_T \varepsilon \tag{5.13}$$

where σ is the Rutherford cross section integrated over a strip, N_B is the number of beam particles incident on the target, N_T is the number of target nuclei in the target and ε is the efficiency [2]. The yield calculated at each step in the target was summed over all steps through the gas cell target giving a total yield for each strip.

The energy distribution of alpha particles emitted at the larger angles subtended by the upstream S2 telescope meant that some of the alpha particles fell below the energy threshold and so a full yield could not be integrated. Therefore the downstream ΔE detector was used as the full alpha particle yield could be integrated above the energy threshold of the detector system. The data were re-sorted so that any particles that registered a hit in both the ΔE and the E detector were discounted, and only particles that hit the ΔE detector were plotted and integrated over the energy range expected for each strip in the downstream telescope. The calculated alpha particle yield from the simulation and the alpha particle yield extracted from the LEDA data were then compared on plots shown in Chapter 6.4.

Experimental Run 2

For the second experimental setup, Rutherford scattering of the ^{23}Na beam on a gold foil fixed in front of the gas cell target, was used to calculate the total number of particles incident on the target. The Rutherford scattering cross section was calculated for each strip of the LEDA detector using Equation B.4. The energy was taken to be the energy of the beam at the centre of the foil. The cross section varied by no more than ±5% from this based on the thickness of the foil.

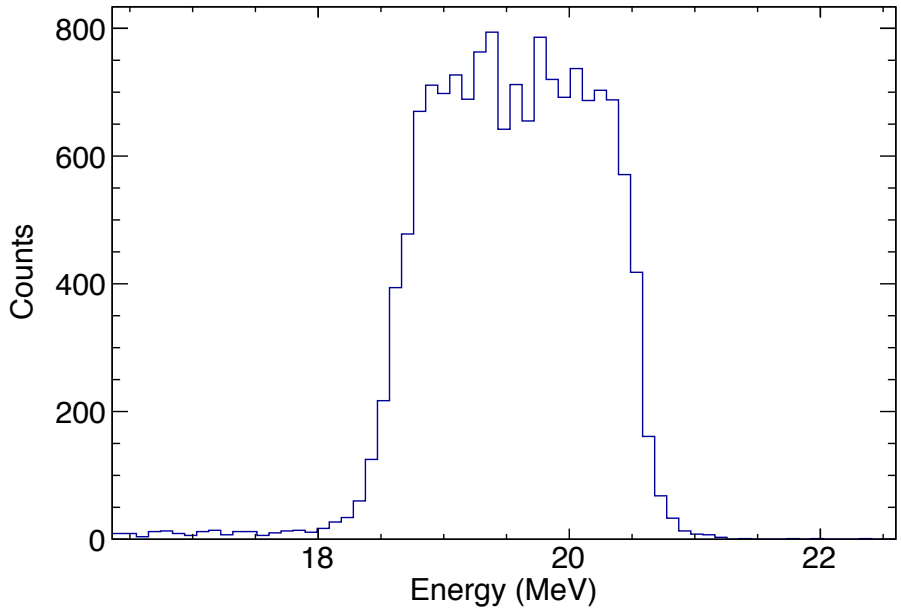

Fig. 5.16 A strip in the LEDA detector showing backscattered beam from the Au foil at E_{cm} = 2.26 MeV.

The total number of beam particles was calculated by re-arranging Equation 5.13 for N_B, where the yield is extracted from the LEDA data for each strip, an example LEDA spectrum is shown in Fig. 5.16. The number of target nuclei were calculated for the gold foil. The efficiency is the measured dead time of the detector system. The average total number of beam particles was then calculated by averaging over the strips of the LEDA array. The error in the beam intensity is the standard deviation of the number of particles for each strip. Beam intensities and their associated errors are shown in Chapter 6.4.

5.8 Angular Distributions

Differential cross sections were calculated using the equation:

$$\frac{d\sigma}{d\Omega} = \frac{Y(\Omega)}{N_B N_T \varepsilon d\Omega} \tag{5.14}$$

where Y(Ω) is the yield of reaction products within a solid angle Ω, N_B is the total number of beam particles incident on the target, N_T is the number of target nuclei per cm^2, ε is the efficiency and dΩ is the solid angle in the centre of mass frame [2].

The detectors were divided by grouping the front annular strips into groups of 6 or 8, depending on the number of counts and dΩ was calculated for each group of strips. The number of target particles and beam particles remained the same as for the total cross section calculations. The yield was extracted for each group of strips, using the same scaling method as was used for the extraction of a yield for the whole detector. The efficiency is calculated as $\varepsilon_{Telescope} \times$ live time, where $\varepsilon_{Telescope}$ is calculated as previously for each group of strips.

Angular distributions were calculated for both experimental setups, however not all energies from the second experimental setup were calculated. Due to the proximity of the detector to the target in each experimental setup the error in angle for each strip was large, equal to $\sim \pm 10^\circ$ in the centre of mass frame for the first experimental setup and $\sim \pm 5^\circ$ in the centre of mass frame for the second experimental setup. This meant that it was not possible to fit the angular distributions leading to an isotropic angular distribution assumption to be made for the total cross section calculations.

5.9 Total Cross Sections

The total cross section in mb was calculated using equation 5.15 [2], where Y is the yield of reaction products measured, N_B is the total number of beam particles

incident on the target, N_T is the number of target nuclei per cm^2 and ε_{Tot} is the efficiency. This is the cross section assuming a flat angular distribution.

$$\sigma = \frac{Y}{N_B N_T \varepsilon_{Tot}} \times 1 \times 10^{-27} \tag{5.15}$$

Cross sections were calculated for ^{23}Na(α,p_0) at all energies. At higher energies where background subtractions were possible ^{23}Na(α,p_1) and ^{23}Na(α,p_2) cross sections were also calculated. In order to calculate an astrophysical reaction rate a total cross section was needed at each energy. At higher energies the total cross section is the sum of the cross sections as calculated using Equation 5.16.

$$\sigma_{Tot} = \sigma_{\mathrm{p_0}} + \sigma_{\mathrm{p_1}} + \sigma_{\mathrm{p_2}} \tag{5.16}$$

At lower energies where cross sections to excited states could not be extracted the total cross section was calculated using the SMARAGD Hauser-Feshbach cross sections. The ratio of $\sigma_{\mathrm{SMARAGD_{p_0}}}/\sigma_{\mathrm{SMARAGD_{Tot}}}$ is within error of the ratio calculated from this data at higher energies. Therefore at lower energies where only the cross section σ_{p_0} is measured from the data, the total cross section is calculated using the relationship

$$\sigma_{Tot} = \frac{\sigma_{\mathrm{SMARAGD_{Tot}}}}{\sigma_{\mathrm{SMARAGD_{p_0}}}} \times \sigma_{p_0}. \tag{5.17}$$

5.10 Reaction Rate Calculation

To calculate a reaction rate the code exp2rate.f [48] written by Thomas Rauscher was used. The code calculates a reaction rate by numerically integrating the equation for reaction rate per particle pair from the input cross sections. The total cross sections

were used to calculate a reaction rate. In the case of the lowest energy point, which is an upper limit, the lower limit to the cross section was 0 mb. In the case of all other data points upper and lower limits were input as the error bars on each cross section point. The temperature range is determined from the energy range of the data.

Chapter 6

Results and Discussion

6.1 Beam Energy Results

The beam energies and their associated errors are shown in Table 6.1, the corrections to the beam energies are described in this section. The error on the beam energy accounts for the beam energy through the gas target plus the uncertainty in the beam energy calculation. At data points where beam energies were similar, the beam energies were checked by comparing proton data from ^{23}Na(α,p)^{26}Mg and by comparing Rutherford scattering of the ^{4}He gas target with the ^{23}Na beam. The result of this check was that two energies were changed from their original calibration. Firstly, the beam energy at E_{beam} =1.35 MeV/u. The beam energy at the centre of the target was calculated to be $E_{c.m.}$=2.42 MeV. This was similar in energy to the data at E_{beam} =1.52 MeV/u which also has a centre of mass energy of $E_{c.m.}$=2.42 MeV. A selection of strips from each of the different setups was chosen such that approximately the same angles were covered, and the protons from ^{23}Na(α,p_0)^{26}Mg were compared. The distributions of the two sets of data are expected to be slightly different due to the difference in the proximity of the detector telescope to the gas cell target, however the total energy seen should be approximately the same for the strips selected. The result of the comparison between the total energy plot for E_{beam} =1.35 MeV/u and E_{beam} =1.52 MeV/u is shown in Fig. 6.1.

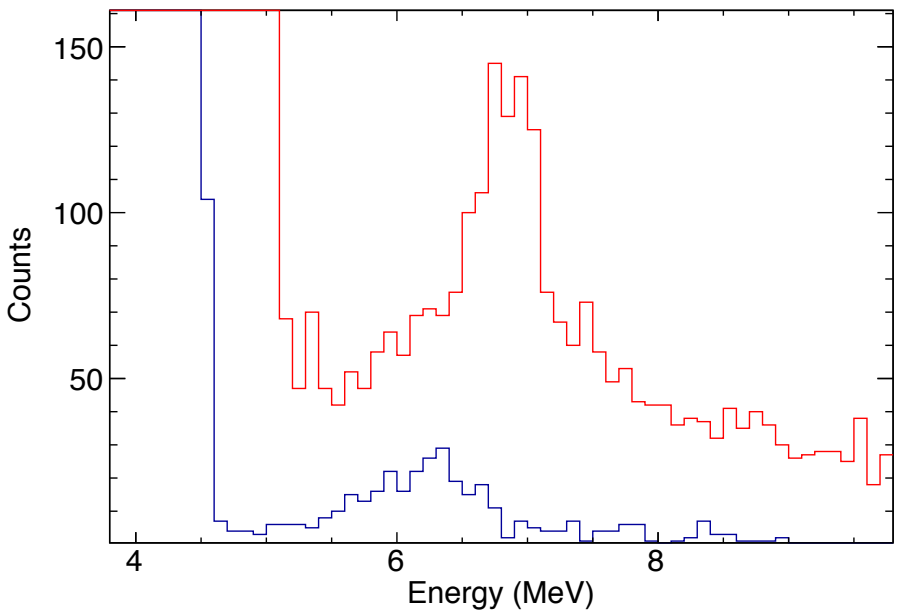

Fig. 6.1 Total energy plot for E_{beam}= 1.35 MeV/u (blue) and E_{beam}= 1.52 MeV/u (red) for a selection of strips which cover approximately the same angles. The plot shows that the energy of the protons from reactions at each beam energy are not similar.

There is clearly a discrepancy between the energies of the proton energy peak from the ^{23}Na(α,p_0)^{26}Mg reaction in Fig. 6.1. The data for E_{beam}= 1.35 MeV/u was compared to data at other energies. It was found that the energy distribution was similar to the beam energy at E_{beam}= 1.46 MeV/u as shown in Fig. 6.2. A comparison of the Monte Carlo simulation to data for E_{beam} =1.52 MeV/u is shown in Fig. 5.13 and was shown to match predictions. The centre of mass energy of the data point for E_{beam}= 1.35 MeV/u was therefore changed to $E_{c.m.}$=2.26 MeV.

The reason for the data corresponding to a different beam energy to the calibration is not clear. It was possible that for this calibration run the beam hit a point on the foil which was thinner. It could also have been that the initial beam energy was lower than expected. The resistors in the LEDA detectors were changed before the data at E_{beam} =1.35 MeV/u, and so the data for the beam backscattered from the entrance window and detected in LEDA does not have a calibration as a calibration run was not performed. It could be possible that the beam energy provided was incorrect.

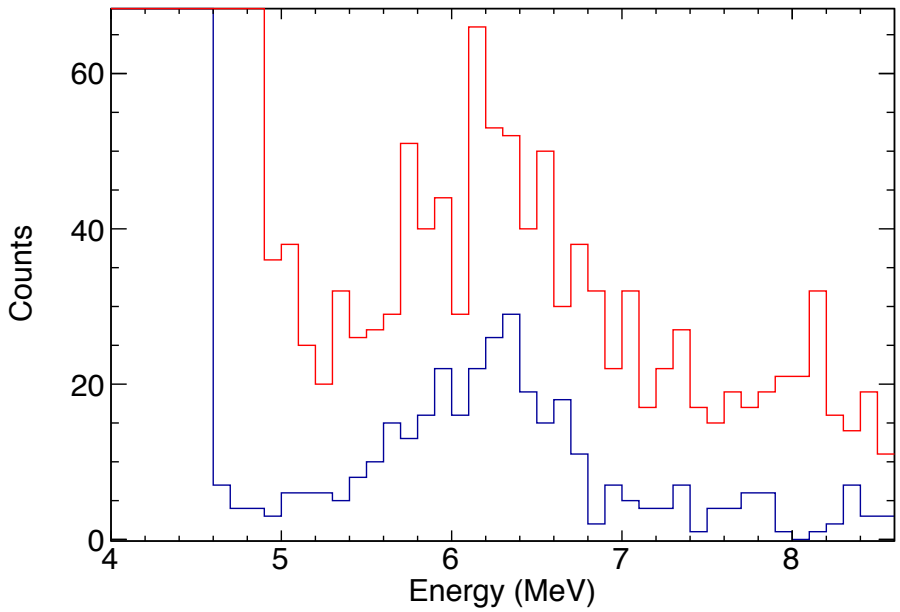

Fig. 6.2 Total energy plot for E_{beam}= 1.35 MeV/u (blue) and E_{beam}= 1.46 MeV/u (red) for a selection of strips which cover approximately the same angles. The plot shows that the energy of the protons from reactions at each beam energy are similar.

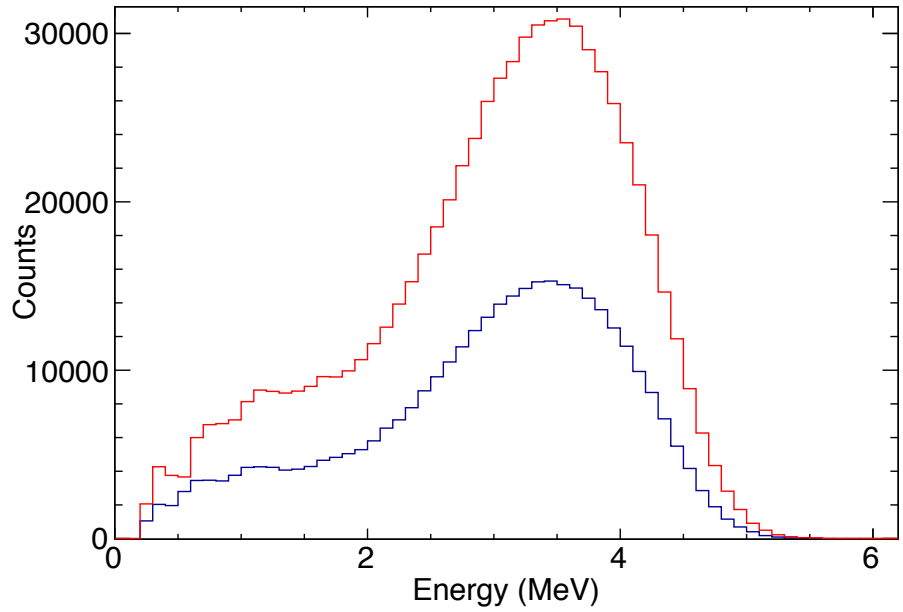

Fig. 6.3 ^{4}He particles from Rutherford scattering of the ^{23}Na beam with the ^{4}He gas target, detected in the ΔE S2 detector, at beam energies of E_{beam}= 1.39 MeV/u with a titanium window (red) and E_{beam}= 1.43 MeV/u with a Ni window (blue).

The second energy which was found to differ was for the data taken with the titanium window during the third experimental run. The Hauser-Feshbach weighted energy was calculated using the calibration to be $E_{c.m.}$=2.32 MeV. The Rutherford scattering data for a single strip in the ΔE detector were compared at each energy for

the third experimental run. This comparison showed that the beam energy inside the gas target was very similar to E_{beam}= 1.43 MeV/u with $E_{c.m.}$ = 2.14 MeV . Figure 6.3 shows an example of Rutherford scattered alpha particle data from the same strip in the ΔE detector for E_{beam}= 1.39 MeV/u with a titanium window (red) and E_{beam}= 1.43 MeV/u (blue) with the Ni entrance window.

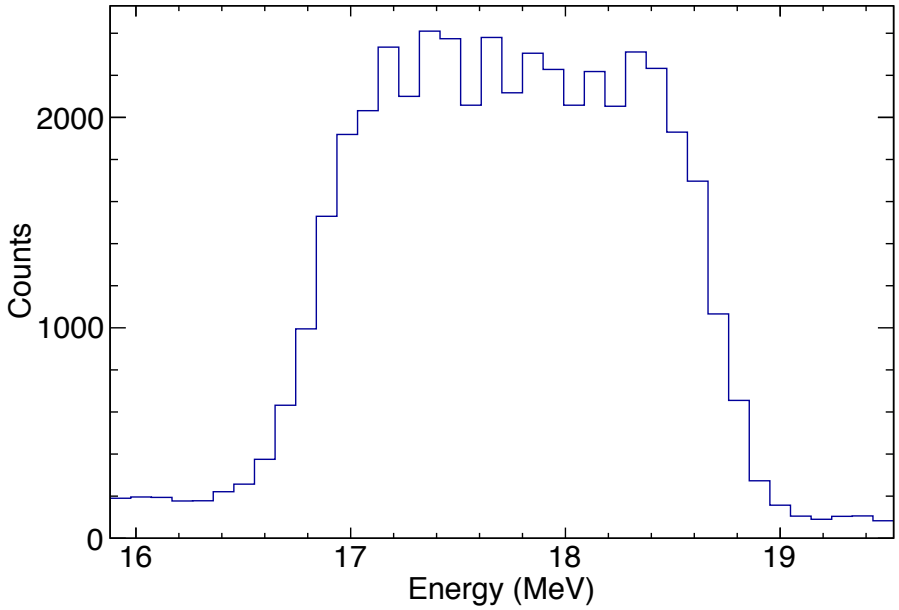

Fig. 6.4 Spectrum from a single strip in LEDA showing beam backscattered from the gold foil upstream of the titanium entrance window at E_{beam}= 1.39 MeV/u.

The beam energy before entering the gold foil, for the data taken with the titanium window, was checked by analysing the LEDA data. The LEDA data showed the backscattered beam from the gold foil mounted upstream of the entrance window. An example of a LEDA spectrum for the data taken with a titanium window is shown in Fg. 6.4. The LEDA data in this strip were expected to have an upper energy limit of 18.8 MeV which is in good agreement with the data. This agreement confirmed that the initial beam energy was E_{beam} = 1.39 MeV/u. Since the energy of the beam incident on the gold foil is as expected it is possible that the thickness of the titanium foil which was mounted in front of the photodiode for calibration purposes was not equal to the thickness of the titanium entrance window. It is possible that they were not cut from the same sheet of foil.

Experiment	E_{beam} (MeV/u)	$E_{c.m.}$ (MeV)		
		Start of Target	End of Target	HF weighted
1	1.18	1.79	1.66	$1.74^{+0.09}_{-0.12}$
	1.21	1.91	1.78	$1.86^{+0.09}_{-0.12}$
	1.25	2.05	1.91	$1.99^{+0.10}_{-0.12}$
	1.35	2.32	2.18	$2.26^{+0.10}_{-0.12}$
2	1.19	1.43	1.28	$1.38^{+0.09}_{-0.14}$
	1.39	2.09	1.95	$2.03^{+0.10}_{-0.12}$
3	1.39	2.08	1.94	$2.02^{+0.10}_{-0.12}$
	1.43	2.2	2.06	$2.14^{+0.10}_{-0.12}$
	1.46	2.32	2.18	$2.26^{+0.10}_{-0.12}$
	1.49	2.39	2.25	$2.33^{+0.10}_{-0.12}$
	1.52	2.48	2.34	$2.42^{+0.10}_{-0.12}$
	1.55	2.61	2.48	$2.55^{+0.10}_{-0.11}$
	1.58	2.73	2.6	$2.67^{+0.10}_{-0.11}$
	1.61	2.84	2.71	$2.78^{+0.10}_{-0.11}$
	1.64	2.98	2.85	$2.92^{+0.10}_{-0.11}$
	1.67	3.09	2.97	$3.03^{+0.10}_{-0.10}$
	1.7	3.15	3.04	$3.1^{+0.09}_{-0.10}$
TiWindow	1.39	2.2	2.06	$2.14^{+0.10}_{-0.12}$

Table 6.1 The beam energies weighted using Hauser Feshbach cross section calculations as described in the text. Two beam energies, one at at E_{beam} = 1.35 MeV and one at E_{beam} = 1.39 MeV with a Ti entrance window were corrected as described in the text.

6.2 ^{23}Na(α,p)^{26}Mg Yields

The results of two different methods of yield extraction are shown in Table 6.2. Firstly, the gas-in and gas-out data are overlayed and scaled and the background is subtracted from the gas-in data. The result of this is shown in the column labelled 'Yield'. This is the yield used to calculate the final cross sections so as to be consistent when extracting yields for p_1 and p_2 protons. The second method was to fit the background then draw this fit onto the gas-in data and scale the height. In each

case scaling was done by eye using the higher energy fusion evaporation proton background.

Experiment	$E_{c.m.}$ (MeV)	Yield (counts)	Yield - Fitting Method (counts)
1	1.74	551±23	563
	1.86	405±20	413
	1.99	338 ±18	351
	2.26	202 ±14	211
2	1.38	0 ± 0	0
	2.03	158±13	162
3	2.02	105± 10	100
	2.14	412± 20	427
	2.26	305± 17	321
	2.33	197± 14	194
	2.42	746± 27	751
	2.55	953± 31	958
	2.67	876±30	921
	2.78	1612 ± 40	1659
	2.92	2703 ±52	2752
	3.03	2592 ± 51	2643
	3.1	2138 ±46	2096
Ti Window	2.26	771 ± 28	783

Table 6.2 Results of yield extraction using two different methods for protons from ^{23}Na(α,p_0)^{26}Mg.

The fitting method resulted in yields which were within error of the yields used to calculate cross sections. In order to check that scaling the background by eye to the higher energy fusion evaporation protons was viable, the background was also scaled to the total number of beam particles incident on the target. This was done at two energies, at $E_{c.m.}$=2.14 MeV a yield of 441±21 counts was calculated and at $E_{c.m.}$=2.26 MeV a yield of 312±18 was calculated. These are both within error of the final yield and so confirmed that the scaling method was viable. As well as this, the limits of integration were changed by ±100 keV which again did not give a change in yield outside of the error.

In order to extract yields for p_1 and p_2 protons the method of scaling using higher energy fusion evaporation was used. At lower energies, where data collection times were longer, it was not possible to resolve the p_1 and p_2 proton peaks beneath the background produced by protons scattered by the beam from water contamination on the entrance window. However at higher energies it was possible to resolve the peaks for p_1 and p_2 protons. It is possible that at the higher energies, where data collection times were shorter, the amount of water contamination on the entrance window remained relatively constant. As well as shorter runs, the chamber had been continuously pumped out, using the turbo and cryo pumps, throughout the experiment and so there would be less moisture present in the chamber as the higher energies were measured later in the experimental run.

The protons measured from reactions to the first excited state in ^{26}Mg are shown in Table 6.3. The protons measured from reactions to the second excited state in ^{26}Mg are shown in Table 6.4.

Experiment	$E_{c.m.}$ (MeV)	Yield (counts)	Error
3	2.42	2499	±50
	2.55	2629	±51
	2.67	2963	±54
	2.78	5528	±74
	2.92	6252	±79
	3.03	7714	±88
	3.1	8353	±91

Table 6.3 Yield of protons from ^{23}Na(α,p_1)^{26}Mg

As well as changing the limits of integration the $\Delta\phi$ and ΔStrip cuts were removed to check that part of the ^{23}Na(α,p)^{26}Mg proton yield was not being lost. The result was that good counts were not being removed by these cuts, with ∼94% of events passing the $\Delta\phi$ cut and ∼88% of the events passing the ΔStrip cut.

Experiment	$E_{c.m.}$ (MeV)	Yield (counts)	Error
3	2.42	624	±25
	2.55	660	±26
	2.67	1125	±34
	2.78	1624	±40
	2.92	2752	±52
	3.03	2551	±51
	3.1	4684	±68

Table 6.4 Yield of protons from ^{23}Na(α,p_2)^{26}Mg

6.3 Efficiency

Table 6.5 shows the efficiency calculated at each energy. The solid angle and detector efficiency are dependant on the telescope geometry. During the first and third experimental runs this was the same at each energy measured for each setup. However, during the second experimental run, part of the silicon detector telescope that detected protons was blocked by an aluminium arm on the mount for the iris. The arm was present for the data taken at $E_{c.m.}$ = 2.03 MeV and removed part way through taking data at $E_{c.m.}$ = 1.38 MeV. The effect of the arm was taken into account in the solid angle calculation and the $\varepsilon_{Telescope}$ calculation. Therefore, although the same setup was used for experimental runs two and three, the calculated efficiencies differ slightly.

In order to check the efficiency calculation the Monte Carlo code was used to model the second experimental setup and calculate the value equivalent to the product of the solid angle multiplied by $\varepsilon_{Telescope}$. This value was calculated to be $3.7^{+0.96}_{-1.52}$ from Table 6.5 and in the Monte Carlo it was calculated to be 3.9%. The result of the Monte Carlo simulation is within error of the calculation for efficiency used for the cross section caluclation.

Experiment	$E_{c.m.}$ (MeV)	Live Time (%)	Solid Angle (sr)	$\varepsilon_{Telescope}$ (%)	ε_{Total} (%)	$\Delta\varepsilon_{Total}$ +(%)	- (%)
1	1.74	86	$1.05^{+0.3}_{-0.46}$	46.0	3.27	29	44
	1.86	91	$1.05^{+0.3}_{-0.46}$	46.0	3.57	29	44
	1.99	77	$1.05^{+0.3}_{-0.46}$	46.0	3.02	29	44
	2.26	70	$1.05^{+0.3}_{-0.46}$	46.0	2.54	29	44
2	1.38	75	$0.533^{+0.14}_{-0.22}$	70.8	22.3	26	41
	2.03	68	$0.461^{+0.12}_{-0.19}$	69.4	17.3	26	41
3	2.02	64	$0.656^{+0.17}_{-0.27}$	71.5	2.39	26	41
	2.14	65	$0.656^{+0.17}_{-0.27}$	71.5	2.43	26	41
	2.26	70	$0.656^{+0.17}_{-0.27}$	71.5	2.61	26	41
	2.33	78	$0.656^{+0.17}_{-0.27}$	71.5	2.91	26	41
	2.42	71	$0.656^{+0.17}_{-0.27}$	71.5	2.65	26	41
	2.55	74	$0.656^{+0.17}_{-0.27}$	71.5	2.76	26	41
	2.67	79	$0.656^{+0.17}_{-0.27}$	71.5	2.95	26	41
	2.78	75	$0.656^{+0.17}_{-0.27}$	71.5	2.80	26	41
	2.92	77	$0.656^{+0.17}_{-0.27}$	71.5	2.88	26	41
	3.03	81	$0.656^{+0.17}_{-0.27}$	71.5	3.02	26	41
	3.1	81	$0.656^{+0.17}_{-0.27}$	71.5	3.02	26	41
Ti Window	2.26	70	$0.656^{+0.17}_{-0.27}$	71.5	2.61	26	41

Table 6.5 Calculated efficiencies and errors.

6.4 Beam Intensity

Table 6.6 shows the total number of beam particles incident with the target calculated for the second and third experimental runs using Rutherford scattering from a gold foil. Also shown is the beam current read from FC4, the Faraday cup located just upstream of the TUDA scattering chamber, before each set of data were taken. The total number of beam particles was calculated for 83 strips in the LEDA detector. An average was then taken and the standard deviation is the error.

Table 6.7 shows the beam intensities calculated during the first experimental run. The average beam current $\bar{I}_{FC}$, calculated using backscattered beam from the entrance window, is used to calculate the total number of particles incident with the

Experiment	$E_{c.m.}$ (MeV)	TUDA FC (enA)	N_B	Error (%)
2	1.38	∼1.5	$2.03\pm0.12\times10^{14}$	6.11
	2.03	0.93	$5.27\pm0.17\times10^{12}$	3.21
3	2.02	1.02	$3.49\pm0.16\times10^{12}$	4.56
	2.14	1.02	$5.51\pm0.26\times10^{12}$	3.9
	2.26	0.5	$3.14\pm0.43\times10^{12}$	13.8
	2.33	0.9	$1.89\pm0.22\times10^{12}$	11.8
	2.42	0.85	$3.25\pm0.18\times10^{12}$	5.59
	2.55	0.8	$2.63\pm0.27\times10^{12}$	10.4
	2.67	0.77	$1.85\pm0.18\times10^{12}$	9.91
	2.78	0.9	$2.77\pm0.27\times10^{12}$	9.59
	2.92	1.0	$2.87\pm0.41\times10^{12}$	14.3
	3.03	0.78	$1.81\pm0.14\times10^{12}$	7.9
	3.1	0.72	$1.78\pm0.22\times10^{12}$	12.5
Ti Window	2.26	0.8	$1.03\pm0.12\times10^{13}$	11.7

Table 6.6 Total number of particles incident with the target calculated from Rutherford scattering on gold foil.

Experiment	$E_{c.m.}$ (MeV)	$\bar{I}_{FC}$ (enA)	Transmission	N_B	Error (%)
1	1.74	0.69± 0.16	0.95	$1.20\pm0.27\times10^{14}$	22.7
	1.86	0.30 ±0.05	0.97	$2.46\pm0.43\times10^{13}$	17.5
	1.99	0.48 ±0.09	0.95	$1.58\pm0.31\times10^{13}$	19.6
	2.26	0.65± 0.08	0.93	$2.81\pm0.33\times10^{12}$	11.7

Table 6.7 Total particles incident with the target for the first experimental run.

target, N_B. As a check of the method, the yield expected from Rutherford scattered alpha particles from the target was calculated and compared to the yield extracted from the data. An example of the comparison of the yields is shown in Fig. 6.5 and Fig. 6.6. Both plots show that the number of counts extracted from the data decreases compared to the simulation results in the outer strips. This effect is seen at each of the four energies measured and is due to the upstream ΔE-E telescope shielding the outer strips of the downstream telescope. There is also an alternating pattern to the counts in successive strips in the detector. This alternating effect is

observed in each of the four beam energies measured, however the reason for it is not clear. It could possibly be an effect of the readout of the strips as each strip is read out on an alternating side to the previous one.

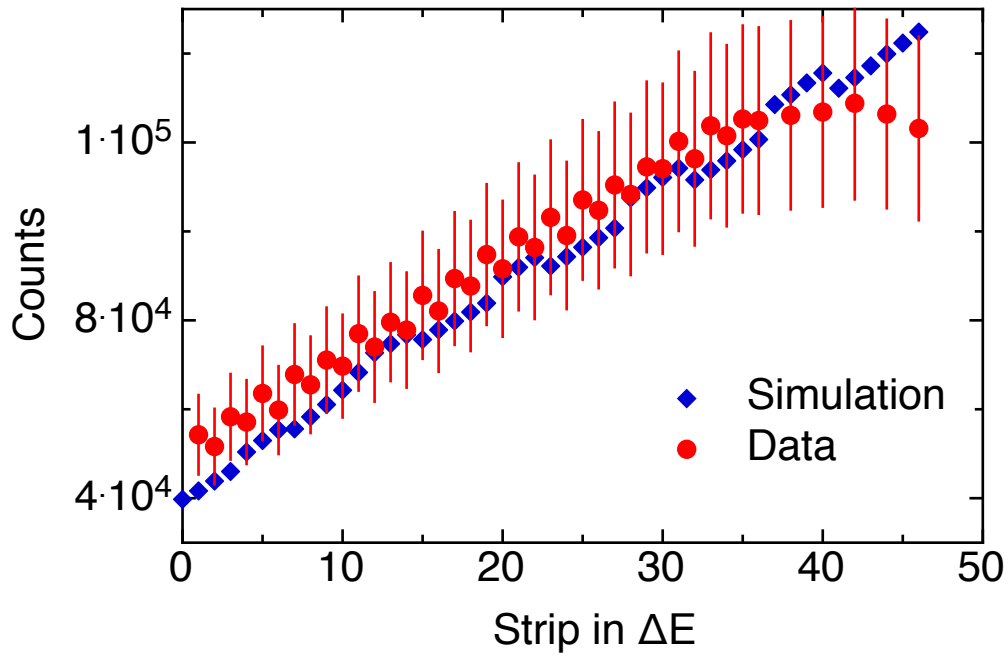

Fig. 6.5 Comparison of yield of alpha particles calculated in simulation to alpha particles detected in each strip of ΔE2 for $E_{c.m.}$ = 1.88 MeV.

Although the counts from the data were found to be consistently higher at each energy, the counts predicted by the simulation were within error of the counts extracted from the data. This confirmed the validity of using the relative yield of backscattered ^{23}Na beam from the Ni entrance window to calculate beam intensity.

In the case of the beam energy of E_{beam} = 1.35 MeV/u the Rutherford scattering yield for ^{23}Na(α,α) was calculated with a beam energy of $E_{c.m.}$=2.26 MeV. The Rutherford scattering in this case was with the ^{4}He target. However, for the data point taken at E_{beam} = 1.39 MeV/u with a titanium entrance window the original beam energy of E_{beam} = 1.39 MeV/u was used to calculate a total number of beam particles using Rutherford scattering of the ^{23}Na beam with the Au foil. This is because although the beam energy inside the gas target was modified, LEDA data showed that the beam energy incident on the Au foil was equal to E_{beam} = 1.39 MeV/u.

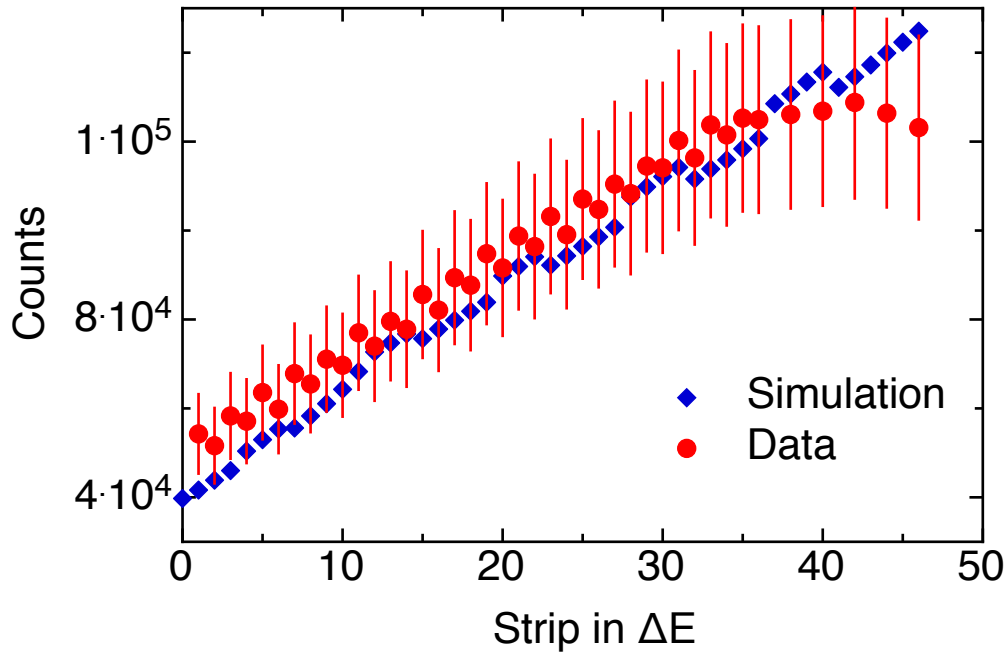

Fig. 6.6 Comparison of yield of alpha particles calculated in simulation to alpha particles detected in each strip of ΔE2 for $E_{c.m.} = 2.26$ MeV.

6.5 Target Particles

The temperature used to calculate the number of target particles in the target was 293 ± 5K which is room temperature. The error of ±5K was assumed since there was not a temperature sensor in the gas cell target. The number of target particles per cm^2 is shown in Table 6.8 along with the pressure inside the gas cell at each energy. The combined error was calculated to be 2.6% at 100 Torr and 2.5% at 110 Torr.

6.6 Angular Distributions

Angular distributions were calculated for the four energies from the first experimental run and at two energies in the third experimental run. An example of some angular distributions are plotted in Fig. 6.7. Due to the thickness of the gas target and the proximity of the ΔE-E telescope there is a large error in angle $\Theta_{c.m.}$ covered by each group of strips. These large error bars mean that a meaningful fit to the data is not possible as many fits could be viable.

Experiment	$E_{c.m.}$ (MeV)	Pressure (Torr)	N_T (cm^{-2})
1	1.74	110.0 ±2	7.25±0.18× 10^{18}
	1.86	110.0 ±2	7.25±0.18× 10^{18}
	1.99	110.0 ±2	7.25±0.18× 10^{18}
	2.26	100.0±2	6.59±0.17× 10^{18}
2	1.38	110.0±2	7.25±0.18× 10^{18}
	2.03	111.7 ±2	7.36±0.18 × 10^{18}
3	2.02	119.6±2	7.90±0.19× 10^{18}
	2.14	110.0±2	7.25±0.18 × 10^{18}
	2.26	110.0 ±2	7.25±0.18× 10^{18}
	2.33	110.0 ±2	7.25±0.18× 10^{18}
	2.42	104.5±2	6.89±0.18× 10^{18}
	2.55	110.5 ±2	7.28±0.18× 10^{18}
	2.67	108.0 ±2	7.12±0.18× 10^{18}
	2.78	106.0 ±2	6.99±0.18× 10^{18}
	2.92	103.3±2	6.81±0.18× 10^{18}
	3.03	110.2 ±2	7.26±0.18× 10^{18}
	3.1	110.1 ±2	7.26±0.18× 10^{18}
Ti Window	2.26	110±2	7.25±0.18 × 10^{18}

Table 6.8 Number of target particles per cm^2

For each beam energy at which data were taken, a flat angular distribution was assumed. This flat angular distribution did not disagree with the angular distributions calculated. However, Howard *et al.* [26] did produce angular distributions from their measurements. Their results show that the distribution is not flat [26], and so the data in this work would be improved if angular distributions for were taken into account in the total cross section calculation.

6.7 Cross Sections

Cross sections for the $^{23}Na(\alpha,p)^{26}Mg$ reaction were calculated at 17 energies. The cross sections are shown in Table 6.9. Where p_1 and p_2 cross sections were not extracted from the data the Hauser-Feshbach statistical model was used to scale p_0

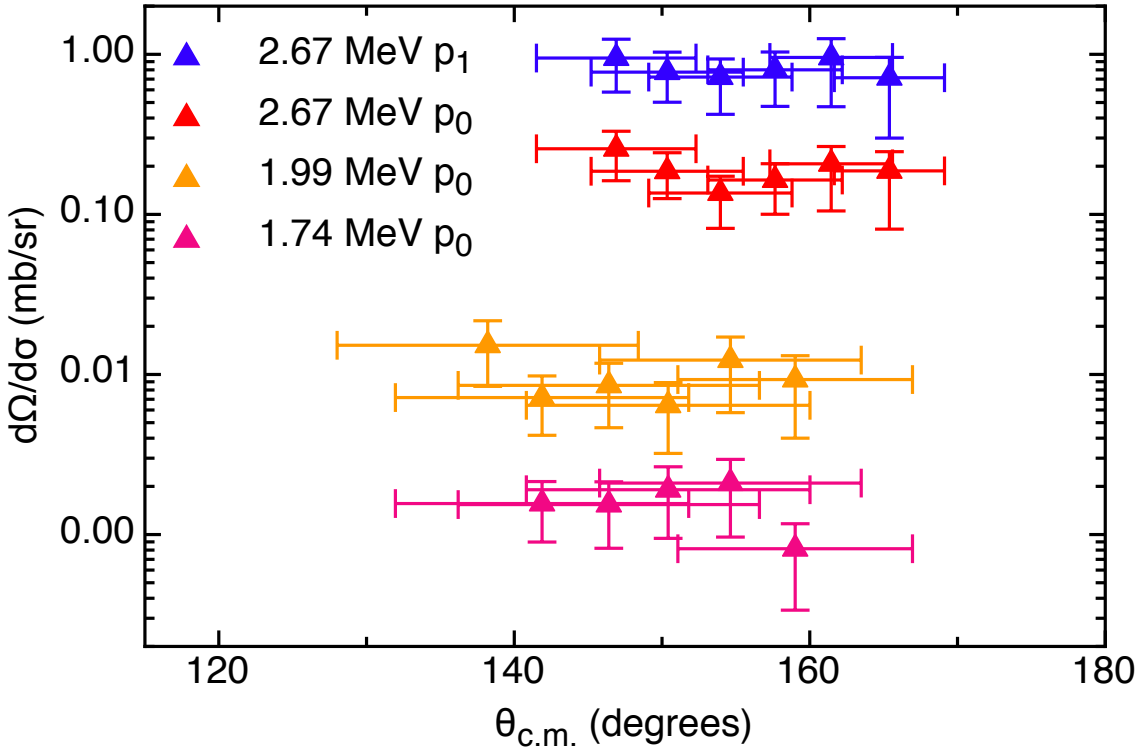

Fig. 6.7 The angular distributions for reaction protons to the ground and first excited states in ^{26}Mg for several beam energies.

cross sections to a total cross section. The ratio of p_0 to p_{tot} from the SMARAGD cross sections is within error of the ratio p_0 to p_{tot} calculated in this work.

Figure 6.8 shows these cross sections plotted with the Hauser-Feshbach cross sections from the codes NON-SMOKER and SMARAGD. Although the statistical model is not thought to be applicable for the ^{23}Na(α,p)^{26}Mg reaction at the energies measured here, there is a remarkable agreement between the NON-SMOKER cross sections and the cross sections calculated in this work. The exception to this agreement is the lowest energy data point. This upper limit point for ^{23}Na(α,p_0)^{26}Mg is eight times lower than the SMARAGD p_0 cross section. As the energy decreases the difference in cross section between experimental data and Hauser-Feshbach calculations increases. It is also interesting to see that reactions to the second excited state in ^{26}Mg make a significant contribution to the cross section, since other measurements of the reaction by Howard *et al.* and Almaraz-Calderon *et al.* have not accounted for these reactions. The work by Almaraz-Calderon *et al.* states that a Hauser-Feshbach calculation showed that at $E_{c.m.} = 2.42$ MeV the p_2 component

$E_{\text{c.m.}}$ (MeV)	σp_0(mb)	σp_1(mb)	σp_2(mb)	σ_{tot} (mb)
$1.38^{+0.09}_{-0.14}$	$\leq 1.04\times10^{-4}$			$\leq 2.22\times10^{-4}$
$1.74^{+0.09}_{-0.12}$	$0.02^{+0.01}_{-0.01}$			$0.05^{+0.02}_{-0.02}$
$1.86^{+0.09}_{-0.12}$	$0.06^{+0.02}_{-0.03}$			$0.19^{+0.07}_{-0.09}$
$1.99^{+0.10}_{-0.12}$	$0.10^{+0.03}_{-0.05}$			$0.30^{+0.10}_{-0.15}$
$2.02^{+0.10}_{-0.12}$	$0.16^{+0.05}_{-0.07}$			$0.51^{+0.18}_{-0.24}$
$2.03^{+0.10}_{-0.12}$	$0.16^{+0.04}_{-0.07}$			$0.51^{+0.14}_{-0.21}$
$2.14^{+0.10}_{-0.12}$	$0.4^{+0.11}_{-0.17}$			$1.3^{+0.4}_{-0.6}$
$2.14^{+0.10}_{-0.12}$	$0.42^{+0.12}_{-0.17}$			$1.3^{+0.4}_{-0.6}$
$2.26^{+0.10}_{-0.12}$	$0.43^{+0.14}_{-0.20}$			$1.5^{+0.5}_{-0.7}$
$2.33^{+0.10}_{-0.12}$	$0.49^{+0.15}_{-0.21}$			$1.8^{+0.5}_{-0.7}$
$2.42^{+0.10}_{-0.12}$	$1.2^{+0.3}_{-0.5}$	$4.0^{+1.1}_{-1.7}$	$1.1^{+0.3}_{-0.5}$	$6.3^{+1.2}_{-1.8}$
$2.55^{+0.10}_{-0.11}$	$1.8^{+0.5}_{-0.8}$	$5.0^{+1.39}_{-2.1}$	$1.3^{+0.4}_{-0.6}$	$8.1^{+1.5}_{-2.3}$
$2.67^{+0.10}_{-0.11}$	$2.3^{+0.6}_{-1.0}$	$7.6^{+2.1}_{-3.2}$	$3.0^{+0.9}_{-1.3}$	$12.9^{+2.4}_{-3.6}$
$2.78^{+0.10}_{-0.11}$	$2.97^{+0.8}_{-1.3}$	$10.2^{+2.8}_{-4.3}$	$3.1^{+0.9}_{-1.3}$	$16.2^{+3.1}_{-4.7}$
$2.92^{+0.10}_{-0.11}$	$4.8^{+1.4}_{-2.1}$	$11.1^{+3.3}_{-4.8}$	$5.1^{+1.5}_{-2.2}$	$21.1^{+3.9}_{-5.7}$
$3.03^{+0.10}_{-0.10}$	$6.5^{+1.8}_{-2.7}$	$19.4^{+5.3}_{-8.1}$	$6.6^{+1.8}_{-2.8}$	$32.6^{+5.9}_{-9.0}$
$3.10^{+0.09}_{-0.10}$	$5.5^{+1.6}_{-2.4}$	$21.4^{+6.2}_{-9.2}$	$12.7^{+3.7}_{-5.5}$	$39.5^{+7.3}_{-10.9}$

Table 6.9 ^{23}Na(α,p)^{26}Mg cross sections calculated in this work.

contributes ∼6% to the cross section with respect to the p_1 component. This work found that at $E_{c.m.} = 2.42$ MeV the p_2 contribution to the total cross section is ∼17% and is within error of the value of the p_0 cross section at this energy.

The total cross sections calculated at similar energies are within error of one another and the data point taken using a titanium entrance window is in agreement with the cross sections calculated using a nickel entrance window. This data point was taken in an attempt to mirror the data taken by Almaraz-Calderon *et al.* as closely as possible with our apparatus since the first set of experimental data taken showed a disagreement in cross section between our work and theirs. Figure 6.9 shows the cross sections calculated in this work for ^{23}Na(α,p_0)^{26}Mg and the total cross sections, which were experimentally measured and calculated. They are compared to the cross sections calculated by the work by Almaraz-Calderon *et al.* [25].

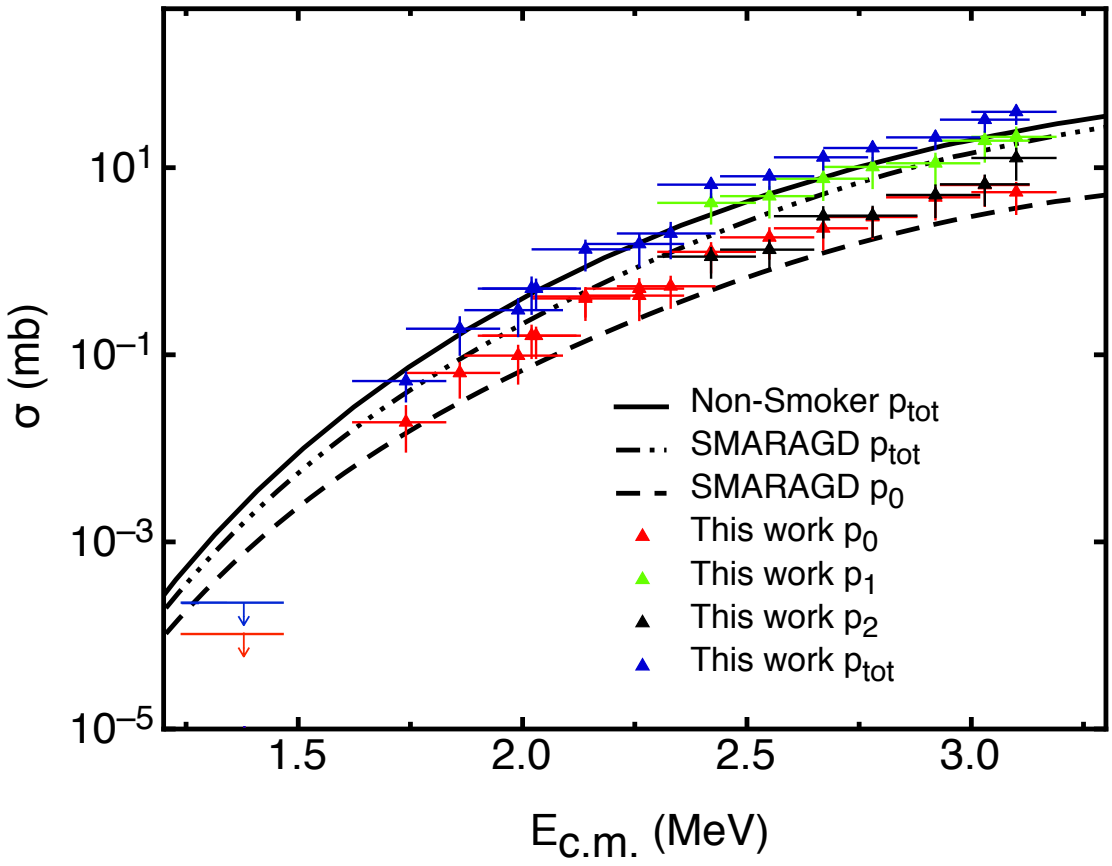

Fig. 6.8 ^{23}Na(α,p)^{26}Mg cross sections calculated in this work plotted with the SMARAGD and NON-SMOKER Hauser-Feshbach cross section calculations. The lowest energy data point is an upper limit.

It is clear that the cross sections calculated in this work are much lower than those in the work of Almaraz-Calderon *et al.* [25]. However it should be noted that although the cross sections are much lower, the ratio $\sigma p_0/\sigma p_1$ is similar, implying that the difference in cross sections could be due to a scaling factor. The re-analysis of the data during this work found no error in the calculations which would cause an increase in cross section by a factor of 20. Further, the cross sections calculated in this work are as expected by the work carried out by Mohr [49], which found that the result by Almaraz-Calderon *et al.* did not follow the trend of cross sections in this mass region [30].

Figure 6.10 shows a plot of the cross sections calculated in this work and the cross sections calculated in the work by Howard *et al.* [26]. The cross sections are mostly in agreement, however there are some points which do not agree. The data

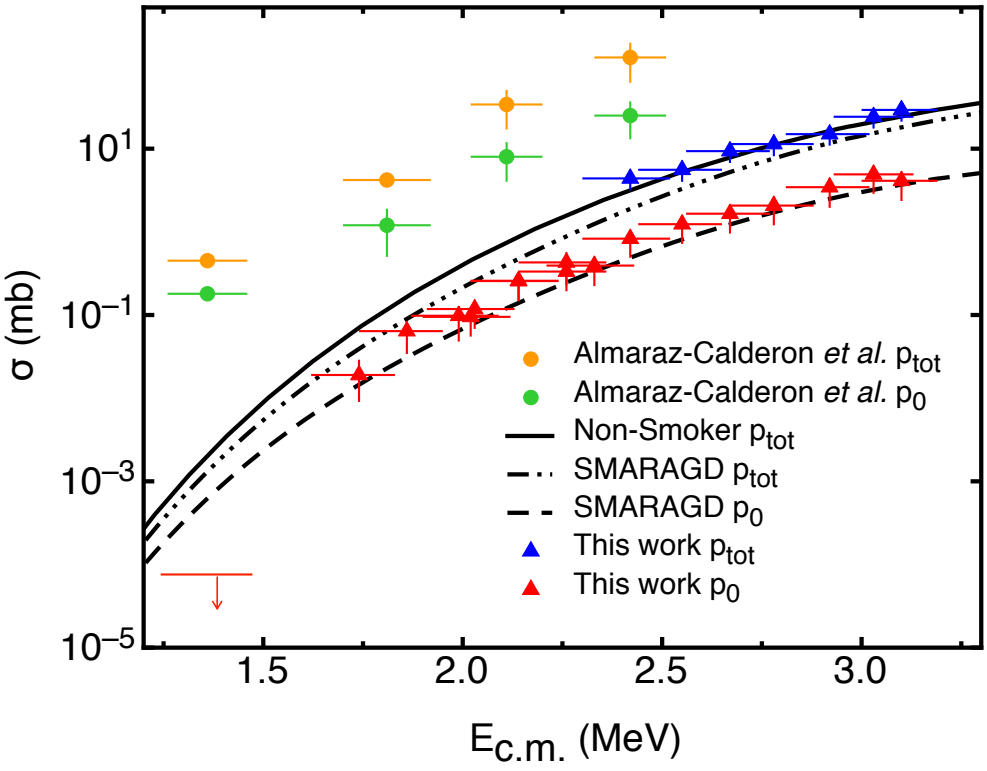

Fig. 6.9 ^{23}Na(α,p)^{26}Mg cross sections calculated in this work plotted with the SMARAGD and NON-SMOKER Hauser-Feshbach cross section calculations and the cross sections from the work by Almaraz-Calderon *et al.* [25]

point at $E_{c.m.}$ = 1.74 MeV has a p_0 cross section of 0.05±0.01 mb. In this work, the cross section calculated for $E_{c.m.}$ = 1.74 MeV has a p_0 cross section of 0.02±0.01 mb. Discussion with the authors of Reference [26] found that the angular distribution for p_0 is heavily peaked at $\theta_{c.m.} = 90°$ [50]. If we assume the same angular distribution for the different energy ranges of the beam in the target, the difference in cross sections is most likely due to the fact that we have not accounted for angular distributions, which would increase the cross section by ∼40% [50]. However this is not conclusive as this work covered a much larger energy range within the target, meaning a larger range of states in the compound nucleus would contribute to the reaction and the angular distributions produced in the work by Howard *et al.* may not be applicable to this work.

Another point which does not agree between the data sets is for p_{tot} at $E_{c.m.}$ = 2.14 MeV. This total cross section is larger than the trend of the other total cross sections calculated in the work of Howard *et al.* due to a strong (α,p) resonance

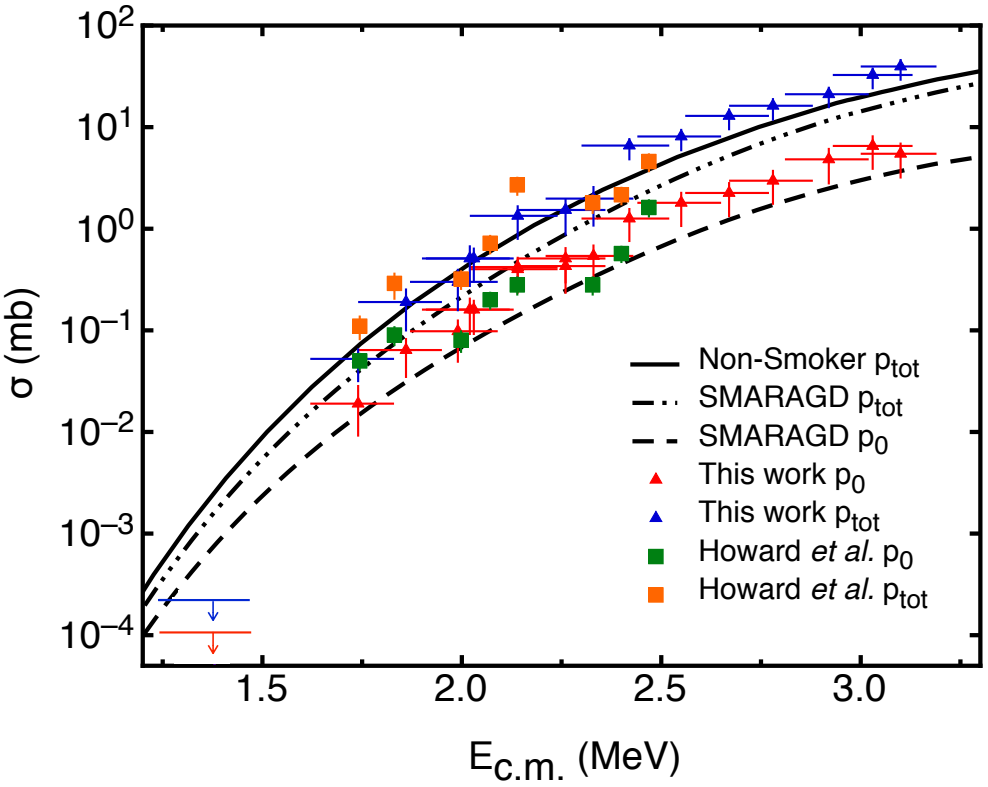

Fig. 6.10 ^{23}Na(α,p)^{26}Mg cross sections calculated in this work plotted with the SMARAGD and NON-SMOKER Hauser-Feshbach cross section calculations and the cross sections from the work by Howard *et al.* [26].

at this energy. The p_1 and p_0 resonance strengths were estimated to be $\omega\gamma_1$ = 1000±300 eV and $\omega\gamma_1$ = 42±13 eV, the strongest contribution comes from the p_1 channel [26]. In this work the p_1 channel was not measured at this energy and the total cross section was calculated by scaling with SMARAGD cross sections. A measurement of the p_1 cross section here may have resulted in agreement between the total cross sections for $E_{c.m.}$ = 2.14 MeV in this work and the work by Howard *et al.*

6.8 Astrophysical Reaction Rate

The astrophysical reaction rate, calculated using the total cross sections from Table 6.9 is shown in Fig. 6.11. Here the rate is compared to the rates calculated in the work of Almaraz-Calderon *et al.* [25] and Whitmire and Davids [24]. The work by Whitmire and Davids underestimated the reaction rate, whereas the work by Almaraz-Calderon

et al. calculated a rate a factor of 40 higher than the Non-Smoker rate. The rate calculated in this work largely agrees with the Non-Smoker rate.

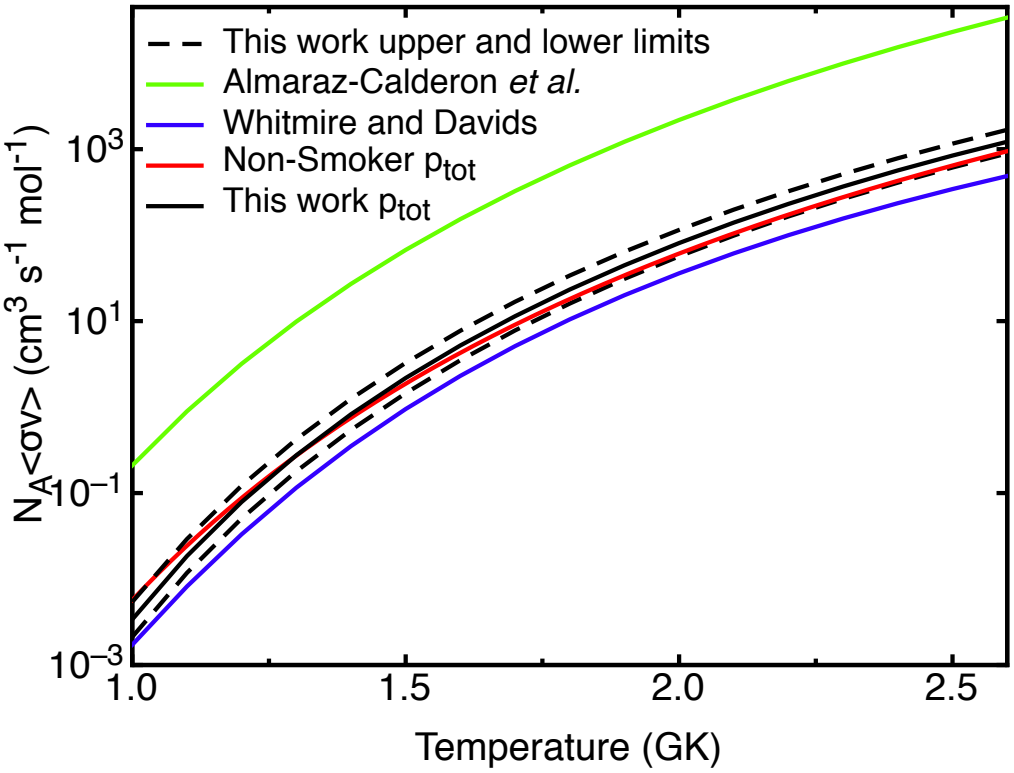

Fig. 6.11 Astrophysical reaction rates calculated for this work compared to the rates produced by Almaraz-Calderon *et al.* [25] and Whitmire and Davids [24]. The Non-Smoker reaction rate is taken from the JINA REACLIB database [21].

Figure 6.12 shows the ratio of the rates calculated in this work to Non-Smoker. It can be seen that the Non-Smoker rate is within the limits of the reaction rate calculated by this work at astrophysical energies of interest. However at lower temperatures the rate decreases due to the lowest energy data point, which is an upper limit and is lower than it is expected to be with the Non-smoker prediction. Howard *et al* conclude that overall their calculated reaction rate is within 30% of the NON-SMOKER rate.

The temperature of interest for C/Ne convective shell burning in massive stars is 1.4 GK. At this temperature the rate lies within 1.7 and 0.7 times the Non-Smoker rate. The study by Iliadis *et al.* [2] concludes that a factor of two increase in the rate produces a factor of 1.3 increase in the amount of ^{26}Al, whilst a factor of 0.5

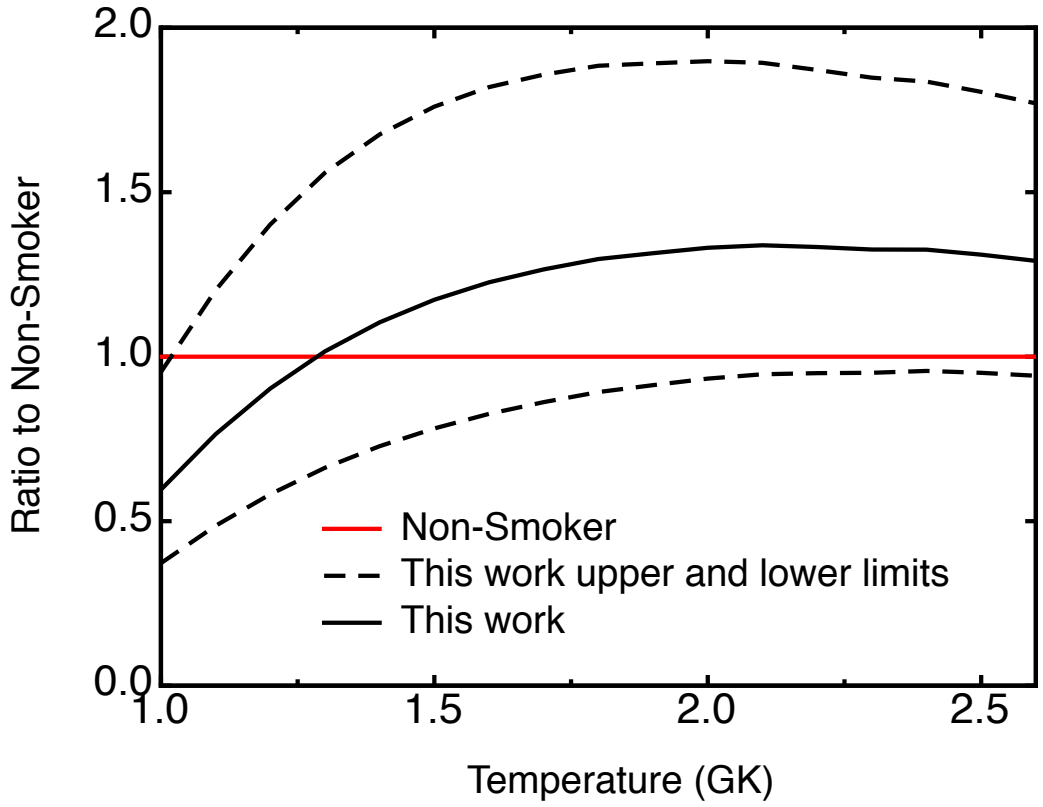

Fig. 6.12 Plot showing the ratio of the rate calculated in this work with the upper and lower limits as a ratio to the NON-SMOKER rate.

change in the rate causes a change in the amount of ^{26}Al of less than 20%. The uncertainties in the rate from the present work lie between these values, therefore the uncertainty in the amount of ^{26}Al produced in the C/Ne convective shell, arising from the the ^{23}Na(α,p)^{26}Mg reaction now has tighter limits of 0.8 - 1.3 times the nominal amount based on this new experimental measurement. Since the limits of the reaction rate lie within the limits which produce these abundance changes, more detailed post processing calculations are now needed to investigate the effect of the new limits on the ^{23}Na(α,p)^{26}Mg reaction rate in the production of ^{26}Al.

In the case of nucleosynthesis in type 1a supernovae, only a quarter of the temperature range of between 2 and 4 GK is covered in these results. The rate is within $\sim$0.9 and 1.9 times that of the Non-Smoker rate. Bravo *et al.* [16] found that for a factor of ten increase in the ^{23}Na(α,p)^{26}Mg reaction rate, the species ^{14}N, ^{21}Ne, ^{23}Na, ^{29}Si, ^{32}P, ^{33}S, ^{37}Cl, ^{40}Ca, ^{45}Sc, ^{44,47}Ti showed an increase by a factor of between 0.12 and 2, and the nuclei ^{26}Mg and ^{43}Ca showed a factor of at least 2

increase. Parikh *et al.* [17] found that when the reaction rate was increased by a factor of ten the ^{23}Na abundance changed by a factor of 0.47, ^{24}Na changed by a factor of 0.3 and ^{53}Cr changed by a factor of 2.1. The new limits to the reaction rate are well within the reaction rate variations studied in this work and so further post processing calculations are needed so that the effects of the new limits on the nuclei produced can be seen.

6.9 Experimental Setup

During the course of the data taking for this experiment the experimental setup was improved upon. The use of the gas cell targets for the measurement of (α,p) reactions at astrophysically relevant energy ranges has proved to be successful, not only in this work but in other measurements also. Margerin *et al.* [51] measured the ^{44}Ti(α,p)^{47}V reaction using the Edinburgh Gas Cell. The use of the Iris in the second experimental setup meant that the chamber did not have to be opened up to add and remove detector shields for tuning, saving several hours.

Fusion evaporation reactions of the beam with carbon and oxygen on the entrance window created a background of protons across the energy range of protons from the ^{23}Na(α,p)^{26}Mg reaction. The cold cone was installed in an attempt to reduce this background, however no evidence was found that it did so. The gold foil mounted in front of the gas cell window was destroyed before it could be checked for hydrocarbon buildup and fusion evaporation protons were observed in the data at all energies. Data were taken with and without the cold cone at the same beam energy, however time constraints meant that the rate of fusion evaporation protons in each case was not analysed. This is something that could be done in the future to provide conclusive evidence as to whether the cold cone reduces the background from fusion evaporation. The work by Margerin *et al.* did not observe a background from fusion evaporation on the entrance window but this may have been due to the lower beam intensities of 5×10^5 pps. The cold cone was very difficult to align to the beam line and for this reason took a lot of time to install. It also had to be brought back up to

temperature before opening the chamber and so added considerably to the time taken to open up the chamber. Based on the fact that fusion evaporation protons were observed with the cone in operation, and the background from the fusion evaporation was easily subtracted by taking data with gas in and out of the target, the cone does not seem to have been effective overall in this case.

The background from ^{23}Na(p,p) scattering of the beam with protons from water on the entrance window were more difficult to remove. The work by Almaraz-Calderon *et al.* [25] used a background subtraction of protons from water contamination on the window by scaling to beam intensity. A background subtraction for this background was not possible at all energies in this work, probably because the amount of water on the entrance window did not remain constant through the longer measurements. A way to monitor this would allow for a background subtraction, however one was not found during this analysis.

Chapter 7

Conclusions

In summary, the cross section of the ^{23}Na(α,p)^{26}Mg reaction has been measured between $E_{\text{c.m.}}$ = 1.38 - 3.1 MeV. At energies above $E_{\text{c.m.}}$= 1.7 MeV, the cross sections were found to be in good agreement with the Non-Smoker Hauser-Feshbach cross section calculations. The lowest energy measured during this work, $E_{\text{c.m.}}$ = 1.38 MeV, which is an upper limit measurement, shows that as energy decreases the Hauser-Feshbach model seems to over predict the cross section by a factor of ∼8. This is consistent with theory in that as the excitation energy in the compound nucleus decreases individual resonances become more significant and the Hauser-Feshbach energy averaged cross section does not reproduce the resonant structure of the cross section [2].

Comparison of the cross sections calculated in this work to previous work shows that there is a clear disagreement with the work by Almaraz-Calderon *et al.* [25]. However, the work of Howard *et al.* [26] is largely in agreement with the work presented in this thesis. For the data point at $E_{\text{c.m.}}$ = 1.74 MeV the discrepancy between the p_0 cross section calculated in the work by Howard *et al.* and this work is thought to be due to the fact that in this work a flat angular distribution was assumed while calculating the cross section. At this energy, an increase of ∼40% in the cross section is expected if the angular distribution calculated by Howard *et al.* is applied [50], however the energy range of the beam in the target is different for the two sets of work. In order to improve upon the work in this thesis, measured angular

distributions should be taken into account when calculating the angle integrated cross sections.

The experimental technique, which incorporated the use of a gas cell target, was found to be very successful in the measurement of the (α,p) reaction cross section and could be used to make similar (α,p) cross section measurements in future. The improvements in the experimental setup, such as the use of the iris as a detector shield which eliminated the need to open the chamber between beam energies were also successful in saving time. Water contamination on the window prevented protons to excited states in ^{26}Mg being detected where longer data collection times were used at lower energies. If possible this should be improved upon in future.

In the case of nucleosynthesis in type 1a supernovae, the temperature range covered in this work amounts to only a quarter of the energy range relevant for nucleosynthesis in this environment. However between 2 and 2.6 GK the new limits are within 0.9 and 1.9 times that of the recommended rate used in the nucleosynthesis model calculations. These models predict abundance changes of between 0.12 and 2 for ^{14}N, ^{21}Ne, ^{23}Na, ^{29}Si, ^{32}P, ^{33}S, ^{37}Cl, ^{40}Ca, ^{45}Sc, ^{44,47}Ti, 2 for ^{26}Mg and ^{43}Ca for a factor of ten change in the ^{23}Na(α,p),^{26}Mg reaction rate [16] and a change of 0.47 change in the abundance of ^{23}Na, a factor of 0.3 change in ^{24}Na and factor of 2.1 change in^{53}Cr for a factor of ten increase in the reaction rate [17]. New post processing calculations are needed to calculate the effect of the new much tighter limits of the ^{23}Na(α,p),^{26}Mg reaction rate on nucleosynthesis in type 1a supernovae.

The result of the current work is that the uncertainty in the ^{26}Al abundance due to the ^{23}Na(α,p)^{26}Mg reaction is now between 0.8 and 1.3 times the nominal abundance. These abundance limits are estimated from the reaction rate variations used by Iliadis *et al.* [2] which lie outside the new limits calculated in this work. The uncertainty in this key reaction for understanding ^{26}Al production in massive stars has therefore been significantly reduced. It is now necessary to carry out further post processing calculations to measure more accurately the effects of the new limits on the ^{23}Na(α,p)^{26}Mg reaction rate on the production of ^{26}Al in the C/Ne convective

burning shell in massive stars. As well as this, experimental data are now needed for other important reactions such as ^{26}Al(n,p)^{26}Mg by which ^{26}Al is destroyed in the C/Ne convective shell of massive stars.

After this thesis was submitted for examination Almaraz Calderon *et al.* issued an erratum [52] to their paper [25] which shows that their data is now in agreement with the data presented in this thesis.

Appendix A

Detector Specifications

A.1 Silicon detector specifications

A.1.1 S2 Detectors

Table A.1 lists the MSL type S2 detector specifications.

Wafer technology	4
Junction window	2M
Ohmic window	2M
Active outer diameter	70 mm
Active inner diameter	22 mm
Chip outer hole diameter	76 mm
Chip inner hole diameter	20 mm
Nunmer of junction elements	48 Incomplete Rings
Junction element pitch	491 um
Junction element seperation	100 um
Number of ohmic elements	16
Package	PCB

Table A.1 Msl-type S2 detector specifications.

Table A.2 lists the detector thicknesses, product codes and bias used for the S2 detector telescopes in experimental setup 1.

Detector	Thickness (μm)	Product Code	Bias (V)
ΔE 1	65	2410-23	14
E1	508	2623-18	130
ΔE2	74	2083-9	20
E2	1051	2951-20	150

Table A.2 S2 detector information for experimental setup 1.

Table A.3 lists the detector thicknesses, product codes and bias used for the S2 detector telescope used in experimental setup 2.

Detector	Thickness (μm)	Product Code	Bias (V)
ΔE	65	2410-23	14
E	1051	2951-20	150

Table A.3 S2 detector information for experimental setup 2.

Table A.4 shows the phi coverage of each strip in an S2 detector.

Strip Number	Active Area (%)	Strip Number	Active Area (%)
0	1.0	24	0.95
1	0.99	25	0.95
2	0.99	26	0.95
3	0.99	27	0.94
4	0.98	28	0.94
5	0.98	29	0.94
6	0.98	30	0.94
7	0.98	31	0.94
8	0.97	32	0.94
9	0.97	33	0.94
10	0.97	34	0.94
11	0.97	35	0.94
12	0.96	36	0.95
13	0.96	37	0.92
14	0.96	38	0.90
15	0.96	39	0.89
16	0.96	40	0.88
17	0.96	41	0.86
18	0.95	42	0.86
19	0.95	43	0.84
20	0.95	44	0.84
21	0.95	45	0.83
22	0.95	46	0.82
23	0.95	47	0.82

Table A.4 S2 detector strip fractional phi coverage.

A.1.2 LEDA Detectors

Table A.5 lists the MSL type YY1 LEDA detector specifications.

Wafer technology	4
Active inner dimensions	55 mm
Active outer dimensions	130 mm
Number of junction elements	16
Number of ohmic elements	1
Active area	29 cm^2
Number of Sectors	8
Sector subtends	45^o
Detector edge surround	0.5 mm
Junction pitch	5 mm
Package	PCB

Table A.5 MSL-type YY1 detector specifications.

Table A.6 lists the detector thicknesses, product codes and bias used for the LEDA detector array used in experimental setup 1.

Detector	Thickness (μm)	Product Code	Bias (V)
LEDA 1	289	2376-17	30
LEDA 2	290	2376-18	30
LEDA 3	288	2376-16	30
LEDA 4	286	2376-12	30

Table A.6 LEDA detector information for array used in experimental setup 1.

Table A.7 lists the detector thicknesses, product codes and bias used for the LEDA detector array used in experimental setup 2.

Detector	Thickness (μm)	Product Code	Bias (V)
LEDA 1	290	1998-3	30
LEDA 2	294	2350-7	30
LEDA 3	297	2350-3	30
LEDA 4	288	2376-16	30
LEDA 5	286	2376-13	30
LEDA 6	290	2376-18	30
LEDA 7	289	2376-17	30

Table A.7 LEDA detector information for array used in experimental setup 2.

Table A.8 shows the phi coverage of each strip in a LEDA segment.

Strip Number	Active Area (%)	Strip Number	Active Area (%)
0	0.11	8	0.11
1	0.11	9	0.11
2	0.11	10	0.11
3	0.11	11	0.11
4	0.11	12	0.11
5	0.11	13	0.10
6	0.11	14	0.08
7	0.11	15	0.05

Table A.8 LEDA detector strip fractional phi coverage.

Appendix B

Analysis Equations

B.1 Laboratory to Centre of Mass coordinate system Convertions

For experimental measurements the observations are made in a reference frame that is at rest in the laboratory, however it is often more convenient to use a reference frame in which the centre of mass is stationary called the centre of mass coordinate system [2]. Figure B.1 shows the kinematics of a reaction A(a,b)B. It should be noted that the total linear momentum in the centre of mass frame is always zero and so particles b and B will travel in opposite directions giving one scattering angle θ' [2].

Using the conservation of momentum it is possible to arrive at the conclusion that the total kinetic energy in the centre-of-mass frame, $E_{c.m.}$, before the collision is related to the laboratory bombarding energy E_a by

$$E_{\text{c.m.}} = E_a \frac{m_A}{m_a + m_A} \tag{B.1}$$

By evaluating the components of velocity parallel with and perpendicular to the beam direction is it also possible to derive the expression relating the angle between

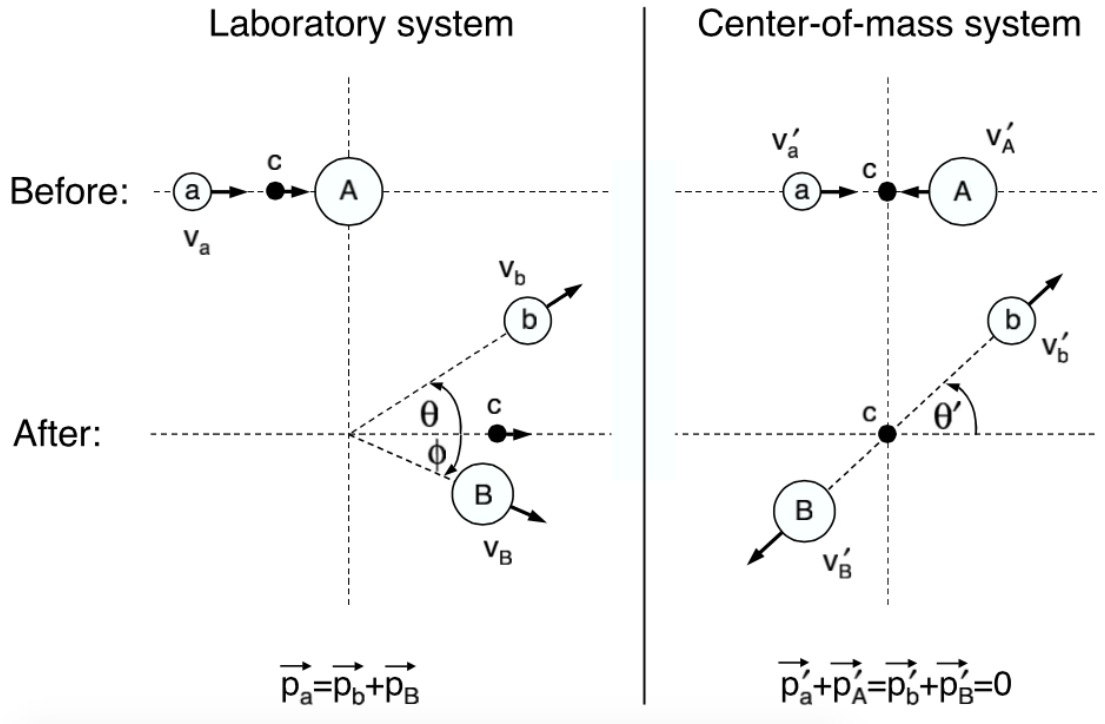

Fig. B.1 Diagram showing the kinematics of a reaction in the laboratory frame and the centre-of-mass coordinate system. The location of the centre of mass is labelled c. Figure taken from reference [2].

the emitted particle and the beam axis in the laboratory and centre of mass frames as

$$cos\theta = \frac{\gamma + cos\theta'}{\sqrt{1+\gamma^2+2\gamma cos\theta'}} \tag{B.2}$$

where

$$\gamma = \frac{v_c}{v'_b} = \sqrt{\frac{m_a m_b E_a}{m_B(m_b+m_B)Q + m_B(M_B+m_b-m_a)E_a}}. \tag{B.3}$$

where θ is the lab angle of the scattered particle, θ' is the centre of mass angle, $Q = (m_a + m_A - m_b - m_B)c^2$, m_a, m_b, m_B and m_A are the particle masses and E_a is the laboratory bombarding energy. For a full derivation of these formulae see Iliadis [2] pages 593 to 597.

B.2 Rutherford Cross Section

In order to calculate the theoretical Rutherford scattering cross section the following equation is used [2].

$$\left[\frac{d\sigma(E)}{d\Omega}\right]_{\theta}^{Ruth} = 1.296\left(\frac{Z_p Z_t}{E}\right)^2 \frac{1}{sin^4(\theta/2)} \tag{B.4}$$

Here energy, E, is in units of MeV, Z_p is the atomic number of the projectile, Z_t is the atomic number of the target and θ is the scattering angle of the scattered particle in the lab frame. This expression gives the cross section in units of mb/sr [2].

B.3 Energy Loss of a Charged Particle

The classical Bethe formula describes the specific energy loss of a charged particle in a medium as:

$$-\frac{dE}{dx} = \frac{4\pi e^2 z^2}{m_0 v^2} NB \tag{B.5}$$

where

$$B = Z\left[ln\left(\frac{2m_0v^2}{I}\right) - ln\left(1-\frac{v^2}{c^2}\right) - \frac{v^2}{c^2}\right]. \tag{B.6}$$

Where e is the electronic charge, m_0 is the electron rest mass, z is the charge of the incident particle, v is the velocity of the incident particle, N is the number density of target atoms, Z is the atomic number of the absorber atoms, I is the average excitation and ionisation potential of the absorber. Note Eqn. B.5 is not in SI units. For non-relativistic incident particles the second two terms in Equation B.6 are insignificant. Energy loss of a particle in a material is therefore dependant on the charge of the particle and is inversely proportional to its energy [37].

References

[1] CAMBRIDGE UNIVERSITY PRESS 1997. The local abundance distribution, 2015. URL http://ned.ipac.caltech.edu/level5/Pagel/Pagel1_3.html.

[2] C. Iliadis. *Nuclear Physics of Stars*. Wiley-VCH, Weinheim, 2007.

[3] W. A. Mahoney, J. C. Ling, W$_M$. A. Wheaton, and A. S. Jacobson. HEAO 3 discovery of ^{26}Al in the interstellar medium. *Astrophysical Journal*, 286:578–585, 1984.

[4] L. Bouchet, E. Jourdain, and J. P. Roques. The Galactic ^{26}Al Emission Map as Revealed by Integral Spi. *The Astrophysical Journal*, 801:142, 2015.

[5] J. Knödlseder. Implications of 1.8 MeV Gamma-Ray Observations for the Origin of ^{26}Al. *The Astrophysical Journal*, 510:915–929, 1999.

[6] G. J. MacPherson, A. M. Davis, and E. K. Zinner. The distribution of aluminium-26 in the early solar system-A reappraisal. *Meteorics*, 30:365–386, 1995.

[7] S. Benemara, N. de Séréville, A. M. Laird, F. Hammache, I. Stefan, P. Roussel, S. Ancelin, M. Assié, A. Coc, I. Deloncle, S. P. Fox, J. Kiener, L. Lefebvre, A. Lefebvre-Schuhl, G. Mavilla, p. Morfouace, Á. M. Sánchez-Benítez, L. Perrot, M. Sinha, V. Tatischeff, and M. Vandebrouck. Nucleosynthesis of ^{26}Al in massive stars: New ^{27}Al states above α and neutron emission thresholds. *Phys. Rev. C*, 89:065805–1–9, 2014.

[8] B. Jacobsen, Q. Yin, F. Moynier, Y. Amelin, A. N. Krot, K. Nagashima, I. D. Hutcheon, and H. Palme. ^{26}Al-^{26}Mg and ^{207}Pb-^{208}Pb systematics of Allende CAIs: Canonical solar initial ^{26}Al/^{27}Al ratio reinstated. *Earth and Planetary Science Letters*, 272:353–364, 2008.

[9] P. Hoppe, S. Amari, E. Zinner, T. Ireland, and R. S. Lewis. Carbon, nitrogen, magnesium, silicon and titanium isotopic compositions of single interstellar silicon carbide grains from the murchison carbonaceous chondrite. *The Astrophysical Journal*, 430:870–890, 1994.

[10] R. Diehl, C. Dupraz, K. Bennett, H. Bloemen, W. Hermsen, J. Knödlseder, G. Lichti, D. Morris, J. Ryan, V. Schönfelder, H. Steinle, A. Strong, B. Swanenburg, M. Varendorff, and C. Winkler. COMPTEL observations of Galactic ^{26}Al emission. *Astronomy and Astrophysics*, 298:445–460, 1995.

[11] M. Limongi and A. Chieffi. The Nucleosynthesis of ^{26}Al and ^{60}Fe in Solar Metalicity Stars Extending in Mass from 11 to 120 M$_\odot$: The Hydrostatic and Explosive Contributions. *The Astrophysical Journal*, 647:483–500, 2006.

[12] R. Diehl, H. Halloin, K. Kretschmer, G. G. Lichti, V. Schönfelder, A. W. Strong, A. von Kienlin, W. Wang, P. Jean, J. Knödlseder, J. P. Roques, G. Weidenspointner, S. Schanne, D. H. Hartmann, C. Winkler, and C. Wundered. Radioactive ^{26}Al from massive stars in the Galaxy. *Nature*, 439:45–47, 2006.

[13] C. Iliadis, A. Chamoagne, A. Chieffi, and M. Limongi. The Effects of Thermonuclear Reaction Rate Variations on ^{26}Al Production in Massive Stars: A Sensitivity Study. *The Astrophysical Journal Supplement Series*, 193:16, 2011.

[14] Boyd R. N. *An Introduction to Nuclear Astrophysics*. The University of Chicago Press, Chicago, 2007.

[15] R. A. Ward and W. A. Fowler. Thermalization of Long-Lived Nuclear Isomeric States Under Stellar Conditions. *The Astrophysical Journal*, 238:266–286, 1980.

[16] E. Bravo and G. Martinez-Pinedo. Sensitivity Study of Explosive Nucleosynthesis in type Ia supernovae: Modification of Individual Thermonuclear Reaction Rates. *Physical Review C*, 85:055805, 2012.

[17] A. Parikh, I. R. Jose, J. Seitenzahl, and F. K. Ropke. The effects of variations in nuclear interactions on nucleosynthesis in thermonuclear supernovae. *Astronomy and Astrophysics*, 557:A3, 2013.

[18] F. K. Thielemann, K. Nomoto, and K. Yokoi. Explosive nucleosynthesis in carbon deflagration models of Type I supernovae. *Astronomy and Astrophysics*, 158:17–33, 1986.

[19] I. J. Thompson and F. M. Nunes. *Nuclear Reactions for Astrophysics*. Cambridge University Press, New York, 2009.

[20] Alak Ray. Massive stars as thermonuclear reactors and their explosions following core collapse, 2015. URL http://inspirehep.net/record/827392/plots.

[21] T. Rauscher and F. K. Thielemann. Astrophysical Reaction Rates from Statistical Model Calculations. *Atomic Data and Nuclear Data Tables*, 75:1–351, 2000.

[22] T. Rauscher and F. K. Thielemann. The path to improved reaction rates for astrophysics. *Journal of Modern Physics E*, 20:1071–1169, 2011.

[23] J. Kuperus. Protons from the alpha-particle bombardment of ^{23}Na. *Physica (Amsterdam)*, 30:2253–2260, 1964.

[24] D. P. Whitmire and C. N. Davids. Reaction ^{23}Na(α,p)^{26}Mg from e_α=2.3-3.7 MeV and the corresponding thermonuclear reaction rate. *Physical Review C*, 9:996–1001, 1974.

[25] S. Almaraz-Calderon, P. F. Bertone, M. Alcorta, M. Albers, C. M. Deibel, C. R. Hoffman, C. L. Jiang, S. T. Marley, K. E. Rehm, and C. Ugalde. Direct measurement of the ^{23}Na(α,p)^{26}Mg Reaction Cross Section at Energies Relevant for the Production of Galactic ^{26}Al. *Physical Review Letters*, 112:152701, 2014.

[26] A. M. Howard, M. Munch, H. O. U. Fynbo, O. S. Kirsebom, K. L. Laursen, C. Aa. Diget, and N. J. Hubbard. ^{23}Na(α,p)^{26}Mg reaction rate at astrophysically relevant energies. *Physical Review Letters*, 115:052701, 2015.

[27] G. M. Temmer and N. P. Heydenburg. Coulomb Excitation Process in the Lighter Odd-Mass Nuclei. *Physical Review*, 96:426–433, 1954.

[28] B. M. Paine, S. R. Kennett, and D. G. Sargood. (p,γ) resonance strengths in the s-d shell. *Physical Review C*, 17:1550–1554, 1977.

[29] C. Rowland, C. Iliadis, A. E. Champagne, and J. Mosher. Measurement of the E_R=338 keV resonance strength for ^{23}Na(p,α)^{20}Ne. *Physical Review C*, 65: 064609, 2002.

[30] P. Mohr. Cross sections of α-induced reactions for targets with masses A≈20-50 at low energies. *The European Journal A*, 51:56, 2015.

[31] J. R. Tomlinson, J. Fallis, A. M. Laird, S. P. Fox, C. Akers, M. Alcorta, M. A. Bentley, G. Christian, B. Davids, T. Davinson, B. R. Fulton, N. Galinski, A. Rojas, C. Ruiz, N. de Séréville, M. Shen, and A. C. Schotter. Measurement of ^{23}Na(α,p)^{26}Mg at energies relevant to ^{26}Al production in massive stars. *Physical Review Letters*, 115:052702, 2015.

[32] TRIUMF. ISAC (Isotope Separator and Accelerator), 2015. URL http://www.triumf.info/wiki/exp-prog/index.php/ISAC_(Isotope_Separator_and_ACcelerator).

[33] TRIUMF. Isac-i and isac-ii experimental halls, August 2015. URL https://www.triumf.info/wiki/exp-prog/index.php/Image:Test-isacii-06segment.jpg.

[34] K. Jayamanna, F. Ames, G. Cojocaru, R. Baartman, P. Bricault, R. Dube, R. Laxdal, M. Marchetto, M. MacDonald, P. Schmor, G. Wight, and D. Yuan. Off-line ion source terminal for ISAC at TRIUMF. *Review of Scientific Instruments*, 79:02C711, 2008.

[35] M. Marchetto, Z. T. Ang, K. Jayamanna, R. E. Laxdal, A. Mitra, and V. Zvyagintsev. Radioactive ion beam post-acceleration and ISAC. *The European Physical Journal Special Topics*, 150:241–242, 2007.

[36] C. Beerč. *Low Energy Measurements of the $^{18}F(p,\alpha)^{15}O$ Cross Section*. PhD thesis, The University of York, Department of Physics, 2010.

[37] G. F. Knoll. *Radiation Detection and Measurement Third Edition*. John Wiley and Sons, U.S.A., 2000.

[38] Micron Semiconductors Ltd. Specialist Detectors for Nuclear Physics - Design S, 2015. URL http://www.micronsemiconductor.co.uk/pdf/s.pdf.

[39] T. Davinson. Private communication. email, 2014.

[40] Micron Semiconductors Ltd. Specialist Detectors for Nuclear Physics - Design YY, 2015. URL http://www.micronsemiconductor.co.uk/pdf/yy.pdf.

[41] S. J. Thomas, T. Davinson, and A. C. Shotter. A modular amplifier system for the readout of silicon strip detectors. *Nuclear Instruments and Methods in Physics Research*, A288:212–218, 1990.

[42] J. F. Ziegler, M. D. Ziegler, and J. P. Biersack. SRIM - the stopping range of ions in matter. *Nuclear Instruments and Methods in Physics Research B*, 268: 1818–1823, 2010.

[43] NEA. SPAR, high-energy muon, pion, heavy ion stopping-powers and ranges, January 2015. URL http://www.oecd-nea.org/tools/abstract/detail/ccc-0228/.

[44] Lise Group @ NSCL/MSU. Lise++, September 2015. URL http://lise.nscl.msu.edu/lise.html.

[45] T. Davinson. kin2b Reaction Kinematics Code. equations taken from Kinematics Of Nuclear Reactions by A. M. Baldin, V. I. Gol'danskii and I. L. Rozenthal, Pergamon Press 1961. email, 2014.

[46] F. S. Goulding, D. A. Landis, J. Cerny, and R. H. Pehl. A New Particle Identifier Technique For Z=1 And Z=2 Particles in the Energy Range > 10 MeV. *Nuclear Instruments and Methods*, 45:337–339, 1966.

[47] J. Cerny, S. W. Cosper, G. W. Butler, H. Brunnader, R. L. McGrath, and F. S. Goulding. Heavy Ion Identification Using the Power Law Technique. *Nuclear Instruments and Methods*, 45:337–339, 1966.

[48] T. Rauscher. exp2rate, January 2015. URL http://download.nucastro.org/codes/exp2rate.f90.

[49] P. Mohr. Private communication. email, 2015.

[50] C. Diget. Private communication. email, 2015.

[51] V. Margerin, A. St. J. Murphy, T. Davinson, R. Dressler, J. Fallis, A. Kankainen, A. M. Laird, G. Lotay, D. J. Mountford, C. D. Murphy, C. Seiffert, D. Schumann, T. Stowasser, T. Stora, C. H. T. Wang, and P. J. Woods. Study of the ^{44}Ti(α,p)^{47}V reaction and implications for core collapse supernovae. *Physics Letters B*, 731:358–361, 2014.

[52] S. Almaraz-Calderon, P. F. Bertone, M. Alcorta, M. Albers, C. M. Deibel, C. R. Hoffman, C. L. Jiang, S. T. Marley, K. E. Rehm, and C. Ugalde. Erratum: Direct measurement of the ^{23}Na(α,p)^{26}Mg Reaction Cross Section at Energies Relevant for the Production of Galactic ^{26}Al [Phys. Rev. Lett. 112, 152701 (2014). *Physical Review Letters*, 115:179901, 2015.